Journal of Computational Physics: X 3 (2019) 100025

Contents lists available at ScienceDirect

Journal of Computational Physics: X

www.elsevier.com/locate/jcpx

An upwind vertex centred finite volume algorithm for nearly and truly incompressible explicit fast solid dynamic applications: Total and Updated Lagrangian formulations

Osama I. Hassan [a], Ataollah Ghavamian [a], Chun Hean Lee [b,*], Antonio J. Gil [a,*], Javier Bonet [c], Ferdinando Auricchio [d]

[a] Zienkiewicz Centre for Computational Engineering, College of Engineering, Swansea University, Bay Campus, SA1 8EN, United Kingdom
[b] Glasgow Computational Engineering Centre, James Watt School of Engineering, University of Glasgow, Glasgow, G12 8QQ, United Kingdom
[c] University of Greenwich, London, SE10 9LS, United Kingdom
[d] Department of Civil Engineering and Architecture, University of Pavia, Pavia, Italy

ARTICLE INFO

Article history:
Received 10 September 2018
Received in revised form 20 March 2019
Accepted 25 March 2019
Available online 24 May 2019

Keywords:
Conservation laws
Solid dynamics
Lagrangian
FVM
Upwind
JST

ABSTRACT

This paper presents an explicit vertex centred finite volume method for the solution of fast transient isothermal large strain solid dynamics via a system of first order hyperbolic conservation laws. Building upon previous work developed by the authors, in the context of alternative numerical discretisations, this paper explores the use of a series of enhancements (both from the formulation and numerical standpoints) in order to explore some limiting scenarios, such as the consideration of near and true incompressibility. Both Total and Updated Lagrangian formulations are presented and compared at the discrete level, where very small differences between both descriptions are observed due to the excellent discrete satisfaction of the involutions. In addition, a matrix-free tailor-made artificial compressibility algorithm is discussed and combined with an angular momentum projection algorithm. A wide spectrum of numerical examples is thoroughly examined. The scheme shows excellent (stable, consistent and accurate) behaviour, in comparison with other methodologies, in compressible, nearly incompressible and truly incompressible bending dominated scenarios, yielding equal second order of convergence for velocities, deviatoric and volumetric components of the stress.

1. Introduction

Current industry codes (e.g. PAM-CRASH, LS-DYNA, ABAQUS, Altair HyperCrash) targeting on the simulation of fast solid dynamics problems (e.g. vehicle crash simulation, hypervelocity impact on honeycomb sandwich panel and implosion of an underwater structure) are developed on the basis of classical low order finite element displacement based formulations. However, these formulations present a number of numerical difficulties, namely (1) spurious hour-glassing and pressure checkerboarding [1], (2) bending difficulty [2], (3) shear and volumetric locking [3], (4) reduced order of convergence for strains and stresses in comparison with displacements and (5) high frequency noise in the vicinity of shocks [4,5].

* Corresponding authors.
E-mail addresses: chunhean.lee@glasgow.ac.uk (C.H. Lee), a.j.gil@swansea.ac.uk (A.J. Gil).

https://doi.org/10.1016/j.jcpx.2019.100025

In order to overcome some of these drawbacks, a variety of different techniques have been introduced in the last few decades. One very popular option is to resort to a selective reduced integration procedure [6–8], typically applied to (trilinear) hexahedral elements. In this case, a reduced number of Gauss integration points is utilised in order to under-integrate the volumetric component of the stress. Despite not satisfying the inf-sup Ladyzenskaja-Babuška-Brezzi condition, this approach remains very appealing to the industry as the modifications required to the existing commercial finite element codes are very minor. As an alternative, some of these shortcomings can be partially addressed with the use of high order schemes [9]. However, the increase in the number of Gauss integration points can drastically reduce the computational efficiency of these schemes in comparison with low order schemes, especially when complex constitutive laws (e.g. visco-elasticity [10], visco-plasticity) are of great interest.

In the case of tetrahedral elements, the most preferred choice in the industry is the Average Nodal Pressure (ANP) procedure originally proposed by Bonet and Burton [11]. In this approach, the pressure field is under-integrated at nodes. Extensive effort has since been made in order to prevent the appearance of hourglassing-like modes [12–17], a typical shortcoming of this type of finite element. Several variants of the original ANP approach have since followed, including the averaged nodal deformation gradient [2], the F-bar method [18], and the Smoothed Finite Element Method (SFEM) [3]. However, all of the enhanced methods described above still suffer from spurious pressure fluctuations when attempting to model predominantly nearly incompressible solids [11]. This specific shortcoming can be partially rectified using the recently proposed SFEM in conjunction with the use of a non-consistent smoothing pressure procedure [19].

On another front, several attempts have also been reported at aiming to solve solid mechanics problems via the use of displacement-based finite volume discretisations [20–23]. Some interesting work has also been recently explored using the open source platform "OpenFOAM", with special attention paid to the simulation of contact mechanics [24], orthotropic materials experiencing moderate strains [25] and metal forming applications [26]. The earliest attempt at employing a system of first order hyperbolic conservation laws in solid dynamics originates from the work of Trangenstein and Colella [27,28], where the conservation variables of the mixed based approach were the linear momentum $\boldsymbol{p}$ and the continuum deformation gradient tensor $\boldsymbol{F}$. Specifically, a second order Godunov-type cell centred Finite Volume Method (FVM) in combination with a Riemann based upwinding stabilisation was presented. Although the consideration of involutions was outlined as part of the paper, its numerical implementation was not fully described. Moreover, the examples explored were restricted to the case of small strain linear elasticity in two dimensions [28]. With a similar philosophy, an alternative version of cell centred FVM (via a node based discretisation of the numerical fluxes) originally proposed by Mazeran and Després [29], and later explored in [30–36], in gas dynamics applications was adapted to the case of hyperelastic solids [37,38]. In parallel, Scovazzi and co-authors [10,39–42] also used a mixed based approach for a linear tetrahedral element by utilising a Variational Multi-Scale method.

In recent years, some of the authors of this manuscript have pursued the same $\{\boldsymbol{p}, \boldsymbol{F}\}$ system whilst exploiting a wide range of spatial discretisation techniques. These include upwind cell centred FVM [43,44], Jameson-Schmidt-Turkel vertex centred FVM [45], upwind vertex centred FVM [46], two step Taylor-Galerkin FEM [47], stabilised Petrov-Galerkin FEM [48–51], Jameson-Schmidt-Turkel Smooth Particle Hydrodynamics (SPH) [52], Streamline Upwind Petrov-Galerkin SPH [53] and upwind SPH [54].

In subsequent papers, the $\{\boldsymbol{p}, \boldsymbol{F}\}$ system was then augmented by incorporating a new conservation law for the Jacobian of the deformation J [46,49] to effectively solve nearly incompressible deformations. Moreover, the $\{\boldsymbol{p}, \boldsymbol{F}, J\}$ formulation was also extended to account for truly incompressible materials utilising a tailor-made fractional step approach [49]. Further enhancement of this framework has recently been reported by the authors [51,55], when considering materials governed by a polyconvex constitutive law where the co-factor $\boldsymbol{H}$ of the deformation plays a dominant role. The complete set of unknowns $\{\boldsymbol{p}, \boldsymbol{F}, \boldsymbol{H}, J\}$ yields an elegant system of conservation laws, where the existence of a generalised convex entropy function enables the derivation of a symmetric system of hyperbolic equations, dual of that expressed in terms of entropy conjugates of the conservation variables [50].

One contribution of the current paper is to enhance the robustness of the $\{\boldsymbol{p}, \boldsymbol{F}\}$ vertex centred finite volume algorithm presented in [45,46] and to extend their applicability to nearly and truly incompressible scenarios. To achieve this, and following the work of [52,53,55,56], we incorporate another two additional geometric conservation laws, one for the co-factor of the deformation $\boldsymbol{H}$ (or area map) and the other for the Jacobian of the deformation J (or volume map). The objective is to explore the improved performance of the vertex centred algorithm when considering these two new conservation laws.

In addition, in this work, two variants of the Lagrangian description of the conservation equations are presented, namely Total Lagrangian formulation (TLF) and Updated Lagrangian formulation (ULF). In the former, evaluation of the integrals is carried out with respect to the initial undeformed configuration, whereas in the latter its integral evaluation is carried out with respect to the time moving deformed configuration. The objective is to demonstrate the small differences observed between both approaches from a discrete viewpoint. Whilst strict correspondence between TLF and ULF is guaranteed at the continuum level, from the semi-discrete viewpoint, $\boldsymbol{H}$ (key for the push forward/pull back operation between TLF and ULF) is not strongly equal to $J\boldsymbol{F}^{-T}$, but only in a weak sense via a conservation law. From a spatial discretisation standpoint, upwind [46] and Jameson-Schmidt-Turkel [45] schemes will be used for comparison purposes. Interestingly, we show that both TLF and ULF representations perform equally well. Thus, it is the authors' opinion that the choice of representation is purely a matter of personal preference.

In the case of near (or full) incompressibility limit or when large rigid body rotations take place, it has been shown by the authors the need to incorporate two additional numerical ingredients for the formulation to be robust, namely, a

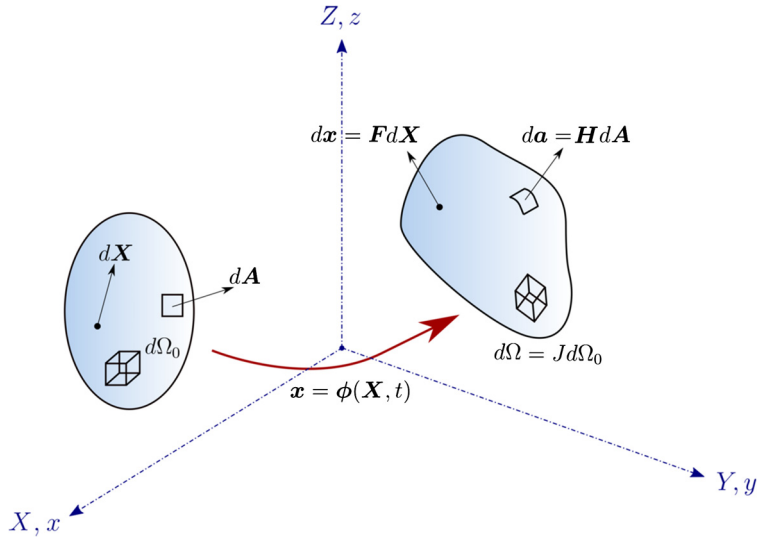

Fig. 1. Motion of a deformable body.

fractional step pressure [49] projection algorithm and a global a posteriori angular momentum projection procedure [44]. It is also the objective of this paper to adapt these two techniques for the case of a vertex centred FVM in order to explore these extreme scenarios.

The outline of the present paper is as follows. Section 2 summarises the complete set of first order conservation laws $\{\boldsymbol{p}, \boldsymbol{F}, \boldsymbol{H}, J\}$ for large strain fast solid dynamics. Both Total Lagrangian and Updated Lagrangian descriptions of the conservation equations, in conjunction with a suitable polyconvex constitutive law, are presented. Section 3 describes the computational methodology of the vertex centred finite volume method. Generation of a dual mesh and its associated area vectors, the Riemann based spatial discretisation and the complete set of Total Lagrangian and Updated Lagrangian semi-discrete equations are presented. Section 4 describes the Total Variation Diminishing Runge-Kutta time integrator used for temporal discretisation. In addition, an adapted artificial compressibility algorithm is also presented in Section 5 to account for truly and nearly incompressible solids. In Section 6, an extensive set of challenging numerical examples is examined to assess the performance of the proposed computational framework. Section 7 presents some concluding remarks and current directions of research. Finally, an Appendix is included where the discrete satisfaction of entropy production of the scheme is demonstrated.

2. Reversible elastodynamics

2.1. Total Lagrangian formalism

Consider the three dimensional deformation of an elastic body of material density ρ_0 moving from its initial undeformed configuration occupying a volume Ω_0, of boundary $\partial\Omega_0$, to a time dependent deformed configuration occupying a volume $\Omega(t)$, of boundary $\partial\Omega(t)$ at time t (see Fig. 1). The motion of the body is defined through a deformation mapping $\boldsymbol{x} = \boldsymbol{\phi}(\boldsymbol{X}, t)$ which satisfies the following system of first order conservation laws [37,43–46,48,52,53,57,58]

$$\frac{\partial \boldsymbol{p}}{\partial t} - \mathrm{DIV}\boldsymbol{P} = \boldsymbol{f}_0; \tag{1a}$$

$$\frac{\partial \boldsymbol{F}}{\partial t} - \nabla_0\left(\frac{\boldsymbol{p}}{\rho_0}\right) = \boldsymbol{0}; \tag{1b}$$

$$\frac{\partial \boldsymbol{H}}{\partial t} - \mathrm{CURL}\left(\frac{\boldsymbol{p}}{\rho_0} \times \boldsymbol{F}\right) = \boldsymbol{0}; \tag{1c}$$

$$\frac{\partial J}{\partial t} - \mathrm{DIV}\left(\boldsymbol{H}^T \frac{\boldsymbol{p}}{\rho_0}\right) = 0. \tag{1d}$$

Here, $\boldsymbol{p} := \rho_0 \boldsymbol{v}$ is the linear momentum per unit of undeformed volume, $\boldsymbol{v}$ represents the velocity field, $\boldsymbol{f}_0$ is the body force per unit of undeformed volume, $\boldsymbol{F}$ is the deformation gradient tensor (or fibre map), $\boldsymbol{H}$ is the cofactor of the deformation gradient tensor (or area map), J is the Jacobian of the deformation gradient tensor (or volume map), $\boldsymbol{P}$ represents the first Piola–Kirchhoff stress tensor, DIV and CURL represent the material divergence and curl operators, respectively, and ∇_0 is the material gradient operator defined as $[\nabla_0]_I := \frac{\partial}{\partial X_I}$. The symbol $\times$ represents the tensor cross product between vectors

and/or second order tensors as that presented in [55,56,59,60]. Finally, for post-processing purposes, the deformed geometry $\boldsymbol{x}$ can be recovered through time integration of the velocity field defined as

$$\frac{\partial \boldsymbol{x}}{\partial t} = \frac{\boldsymbol{p}}{\rho_0}. \tag{2}$$

As the system of conservation laws presented above has more equations than needed, compatibility relationships, also known as involutions, are necessary [27,28,61,62], namely[1]

$$\text{CURL}\boldsymbol{F} = \boldsymbol{0}; \qquad \text{DIV}\boldsymbol{H} = \boldsymbol{0}. \tag{3}$$

It is now possible to combine all of the Total Lagrangian conservation equations described in (1a)–(1d) into a system of first order hyperbolic equations

$$\frac{\partial \mathcal{U}}{\partial t} + \sum_{I=1}^{3} \frac{\partial \mathcal{F}_I}{\partial X_I} = \mathcal{S}, \tag{4}$$

where $\mathcal{U}$ is the vector of conservation variables, $\mathcal{F}_I$ is the flux column vector in I-th material direction and $\mathcal{S}$ is the source term, which can be written as

$$\mathcal{U} = \begin{bmatrix} \boldsymbol{p} \\ \boldsymbol{F} \\ \boldsymbol{H} \\ J \end{bmatrix}, \qquad \mathcal{F}_I = -\begin{bmatrix} \boldsymbol{P}\boldsymbol{E}_I \\ \frac{1}{\rho_0}\boldsymbol{p}\otimes\boldsymbol{E}_I \\ \boldsymbol{F}\times\left(\frac{1}{\rho_0}\boldsymbol{p}\otimes\boldsymbol{E}_I\right) \\ \boldsymbol{H}:\left(\frac{1}{\rho_0}\boldsymbol{p}\otimes\boldsymbol{E}_I\right) \end{bmatrix}, \qquad \mathcal{S} = \begin{bmatrix} \boldsymbol{f}_0 \\ \boldsymbol{0} \\ \boldsymbol{0} \\ 0 \end{bmatrix}, \tag{5}$$

and the Cartesian coordinate basis

$$\boldsymbol{E}_1 = \begin{bmatrix} 1 \\ 0 \\ 0 \end{bmatrix}; \quad \boldsymbol{E}_2 = \begin{bmatrix} 0 \\ 1 \\ 0 \end{bmatrix}; \quad \boldsymbol{E}_3 = \begin{bmatrix} 0 \\ 0 \\ 1 \end{bmatrix}. \tag{6}$$

In addition, the surface flux vector is also defined as

$$\mathcal{F}_{\boldsymbol{N}} = \sum_{I=1}^{3} \mathcal{F}_I N_I = -\begin{bmatrix} \boldsymbol{P}\boldsymbol{N} \\ \frac{1}{\rho_0}\boldsymbol{p}\otimes\boldsymbol{N} \\ \boldsymbol{F}\times\left(\frac{1}{\rho_0}\boldsymbol{p}\otimes\boldsymbol{N}\right) \\ \boldsymbol{H}:\left(\frac{1}{\rho_0}\boldsymbol{p}\otimes\boldsymbol{N}\right) \end{bmatrix}, \tag{7}$$

with $\boldsymbol{N}$ being the material outward unit normal vector of a surface.

In the presence of non-smooth solutions, above conservation equations (1a)–(1d) are accompanied by appropriate Rankine Hugoniot jump conditions across a discontinuous surface (defined by a material unit normal vector $\boldsymbol{N}$) propagating with speed U in the reference space [43,44,46,50,51]. This can be described as

$$U[\![\boldsymbol{p}]\!] = -[\![\boldsymbol{P}]\!]\boldsymbol{N}; \tag{8a}$$

$$U[\![\boldsymbol{F}]\!] = -\frac{1}{\rho_0}[\![\boldsymbol{p}]\!]\otimes\boldsymbol{N}; \tag{8b}$$

$$U[\![\boldsymbol{H}]\!] = -\boldsymbol{F}^{\text{Ave}}\times\left(\frac{1}{\rho_0}[\![\boldsymbol{p}]\!]\otimes\boldsymbol{N}\right); \tag{8c}$$

$$U[\![J]\!] = -\boldsymbol{H}^{\text{Ave}}:\left(\frac{1}{\rho_0}[\![\boldsymbol{p}]\!]\otimes\boldsymbol{N}\right). \tag{8d}$$

Here, $[\cdot]^{\text{Ave}} := \frac{1}{2}\left([\cdot]^+ + [\cdot]^-\right)$ represents an average state between the left and right states of a discontinuous surface and $[\![\cdot]\!] := [\cdot]^+ - [\cdot]^-$ denotes the jump operator across a discontinuous surface.

[1] Indeed conservation equations for the cofactor and Jacobian of the deformation are not strictly necessary from a continuum standpoint as these two kinematic fields are intrinsically (strongly) related (via compatibility equations or involutions) with the deformation gradient. However, from a semi-discrete viewpoint, this strong compatibility weakens and can be "exploited" in order to add flexibility to a numerical (low order) scheme circumventing locking related problems.

Integrating expression (4) over any arbitrary undeformed domain Ω_0, followed by the application of the integration by parts on the flux vector, gives

$$\frac{d}{dt}\int_{\Omega_0} \boldsymbol{\mathcal{U}}\, d\Omega_0 = -\int_{\partial\Omega_0} \boldsymbol{\mathcal{F}_N}\, dA + \int_{\Omega_0} \boldsymbol{\mathcal{S}}\, d\Omega_0. \tag{9}$$

Equation above can then be particularised for each individual component of the conservation equations described in (1a)–(1d), yielding

$$\frac{d}{dt}\int_{\Omega_0} \boldsymbol{p}\, d\Omega_0 = \int_{\partial\Omega_0} \boldsymbol{P}\boldsymbol{N}\, dA + \int_{\Omega_0} \boldsymbol{f}_0\, d\Omega_0; \tag{10a}$$

$$\frac{d}{dt}\int_{\Omega_0} \boldsymbol{F}\, d\Omega_0 = \int_{\partial\Omega_0} \frac{1}{\rho_0}\boldsymbol{p}\otimes\boldsymbol{N}\, dA; \tag{10b}$$

$$\frac{d}{dt}\int_{\Omega_0} \boldsymbol{H}\, d\Omega_0 = \int_{\partial\Omega_0} \boldsymbol{F}\times\left(\frac{1}{\rho_0}\boldsymbol{p}\otimes\boldsymbol{N}\right) dA; \tag{10c}$$

$$\frac{d}{dt}\int_{\Omega_0} J\, d\Omega_0 = \int_{\partial\Omega_0} \frac{1}{\rho_0}\boldsymbol{p}\cdot(\boldsymbol{H}\boldsymbol{N})\, dA. \tag{10d}$$

Remark 1. It is also useful to present an alternative non-conservative form (for the case of smooth solutions) of the differential equations (known as transport equations) for $\{\boldsymbol{H}, J\}$. This is achieved by inserting (3) into equations (1c) and (1d), and after some simple algebraic manipulations, to give

$$\frac{\partial \boldsymbol{H}}{\partial t} = \boldsymbol{F}\times\nabla_0\left(\frac{\boldsymbol{p}}{\rho_0}\right); \qquad \frac{\partial J}{\partial t} = \boldsymbol{H}:\nabla_0\left(\frac{\boldsymbol{p}}{\rho_0}\right). \tag{11}$$

Their equivalent integral forms are

$$\frac{d}{dt}\int_{\Omega_0} \boldsymbol{H}\, d\Omega_0 = \int_{\Omega_0}\left[\boldsymbol{F}\times\nabla_0\left(\frac{\boldsymbol{p}}{\rho_0}\right)\right] d\Omega_0; \qquad \frac{d}{dt}\int_{\Omega_0} J\, d\Omega_0 = \int_{\Omega_0}\left[\boldsymbol{H}:\nabla_0\left(\frac{\boldsymbol{p}}{\rho_0}\right)\right] d\Omega_0, \tag{12}$$

respectively.

For the particular case of a reversible process, the closure of the hyperbolic system (1a)–(1d) requires the introduction of a suitable constitutive law relating the stress tensor $\boldsymbol{P}$ with the geometric strain measures $\{\boldsymbol{F}, \boldsymbol{H}, J\}$, obeying the principle of objectivity [63] and thermodynamic consistency (via the Colemann-Noll procedure). In this work, a nearly incompressible constitutive model (derived on the basis of a polyconvex multi-variable energy function) is employed and will be presented in Section 2.1.1. The use of the first order system (1a)–(1d), in conjunction with a polyconvex constitutive law (i.e. a guarantor of material stability), ensures hyperbolicity and also enables the transformation of the original system of conservation laws into a symmetric set of hyperbolic equations expressed in terms of the entropy conjugates of the conservation variables [51,55].

Finally, for a complete definition of the initial boundary value problem, initial and boundary (essential and natural) conditions must be specified as appropriate. In particular, four different types of boundary conditions will be considered in this paper (refer to Fig. 2).

2.1.1. Constitutive model: polyconvex elasticity

For a nearly incompressible Mooney-Rivlin material, the convex multi-variable strain energy W can be decomposed into the summation of deviatoric $\hat{W}(\boldsymbol{F}, \boldsymbol{H}, J)$ and volumetric $U(J)$ contributions [51,55,60]

$$W = \hat{W} + U, \tag{13}$$

with

$$\hat{W} = \zeta\, J^{-2/3}\,(\boldsymbol{F}:\boldsymbol{F}) + \xi\, J^{-2}\,(\boldsymbol{H}:\boldsymbol{H})^{3/2} - 3\left(\zeta + \sqrt{3}\xi\right); \qquad U = \frac{\kappa}{2}(J-1)^2, \tag{14}$$

where ζ, ξ and κ (bulk modulus) are positive material parameters. By comparison of the tangent elasticity operator at the initial undeformed configuration with that of classical linear elasticity [59,60], appropriate values for the material parameters ζ and ξ can be defined in terms of the shear modulus μ, that is, $2\zeta + 3\sqrt{3}\xi = \mu$ [52,53,55].

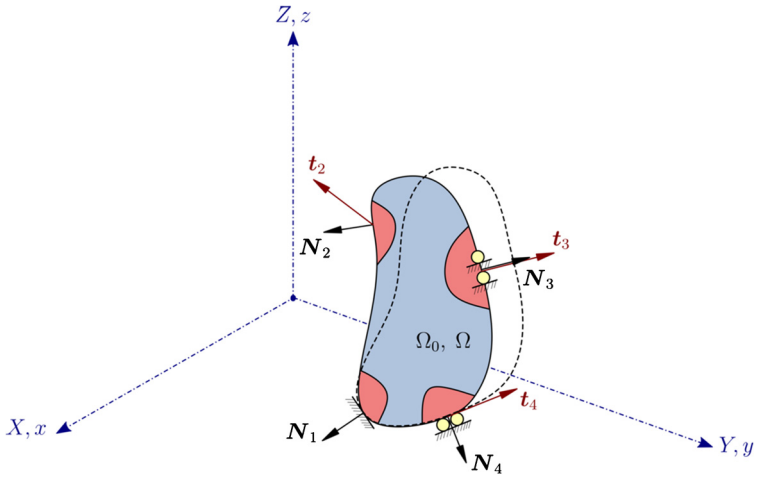

Fig. 2. Boundary conditions. The reference configuration is designated by a continuous line while the deformed configuration is represented by a discontinuous line. Four types of boundary conditions are considered: (1) Fixed, (2) Free, (3) Skew symmetric and (4) Symmetric.

Following Reference [51], the first Piola-Kirchhoff stress tensor $\boldsymbol{P}$ can be expressed as

$$\boldsymbol{P} = \boldsymbol{\Sigma}_{\boldsymbol{F}} + \boldsymbol{\Sigma}_{\boldsymbol{H}} \times \boldsymbol{F} + \Sigma_J \boldsymbol{H}, \tag{15}$$

where the conjugate stresses $\{\boldsymbol{\Sigma}_{\boldsymbol{F}}, \boldsymbol{\Sigma}_{\boldsymbol{H}}, \Sigma_J\}$ with respect to $\{\boldsymbol{F}, \boldsymbol{H}, J\}$ are defined as

$$\boldsymbol{\Sigma}_{\boldsymbol{F}} := \frac{\partial \hat{W}}{\partial \boldsymbol{F}} = 2\zeta J^{-2/3}\boldsymbol{F}; \qquad \boldsymbol{\Sigma}_{\boldsymbol{H}} := \frac{\partial \hat{W}}{\partial \boldsymbol{H}} = 3\xi J^{-2}(\boldsymbol{H}:\boldsymbol{H})^{1/2}\boldsymbol{H}, \tag{16}$$

and $\Sigma_J := \hat{\Sigma}_J + p$ with

$$\hat{\Sigma}_J := \frac{\partial \hat{W}}{\partial J} = -\frac{2}{3}\zeta J^{-5/3}(\boldsymbol{F}:\boldsymbol{F}) - 2\xi J^{-3}(\boldsymbol{H}:\boldsymbol{H})^{3/2}; \qquad p := \frac{dU}{dJ} = \kappa(J-1). \tag{17}$$

It is worth noticing that the energy function (13) described above degenerates to the case of a nearly incompressible neo-Hookean model by imposing the values of $\zeta = \frac{\mu}{2}$ and $\xi = 0$ [55].

2.2. Updated Lagrangian formalism

Insofar as the current industry solid solvers (e.g. PAM-CRASH, LS-DYNA, ABAQUS, Altair HyperCrash) are generally established starting from an Updated Lagrangian kinematical description, an equivalent system of Updated Lagrangian conservation equations for $\{\boldsymbol{p}, \boldsymbol{F}, \boldsymbol{H}, J\}$ will be presented in this section.

Utilising both the Nanson's formula [63] (i.e. $\boldsymbol{n}da = \boldsymbol{H}\boldsymbol{N}dA$) and the volume mapping transformation (i.e. $d\Omega = Jd\Omega_0$), equation (9) becomes

$$\frac{d}{dt}\int_{\Omega(t)} \mathbf{U}\, d\Omega = \int_{\partial\Omega(t)} \mathbf{F}_{\boldsymbol{n}}\, da + \int_{\Omega(t)} \mathbf{S}\, d\Omega, \tag{18}$$

where $\mathbf{U} := J^{-1}\boldsymbol{\mathcal{U}}$, $\mathbf{F}_{\boldsymbol{n}} := \sum_{i=1}^{3}\left(\boldsymbol{H}^{-T}\boldsymbol{\mathcal{F}}\right)_i n_i$, $\mathbf{S} := J^{-1}\boldsymbol{\mathcal{S}}$ and $\boldsymbol{n}$ represents the spatial outward unit normal vector on a moving boundary surface $\partial\Omega(t)$. Above expression can also be particularised for each conservation law employed in this work, yielding the full system written under the Updated Lagrangian description as

$$\frac{d}{dt}\int_{\Omega(t)} \rho\boldsymbol{v}\, d\Omega = \int_{\partial\Omega(t)} \boldsymbol{\sigma}\boldsymbol{n}\, da + \int_{\Omega(t)} \boldsymbol{f}\, d\Omega; \tag{19a}$$

$$\frac{d}{dt}\int_{\Omega(t)} J^{-1}\boldsymbol{F}\, d\Omega = \int_{\partial\Omega(t)} \left[\boldsymbol{v}\otimes\left(\boldsymbol{H}^{-1}\boldsymbol{n}\right)\right] da; \tag{19b}$$

$$\frac{d}{dt}\int_{\Omega(t)} J^{-1}\boldsymbol{H}\, d\Omega = \int_{\partial\Omega(t)} \boldsymbol{F}\times\left[\boldsymbol{v}\otimes\left(\boldsymbol{H}^{-1}\boldsymbol{n}\right)\right] da; \tag{19c}$$

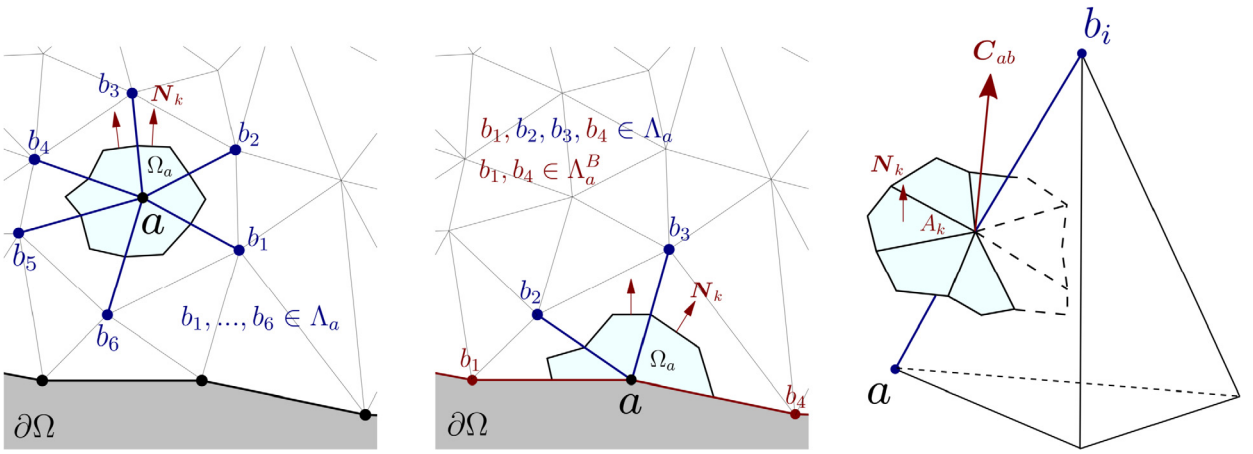

(a) Interior node (b) Boundary node (c) Mean normal vector

Fig. 3. Dual mesh of (a) an interior node and (b) a boundary node using the medial dual approach in two dimensional triangular mesh. Figure (c) shows the mean surface area normal vector of a given edge *ab* for a three dimensional tetrahedral mesh.

$$\frac{d}{dt}\int_{\Omega(t)} d\Omega = \int_{\partial\Omega(t)} \boldsymbol{v}\cdot\boldsymbol{n}\, da. \tag{19d}$$

Here, $\rho := J^{-1}\rho_0$ is the current density and $\boldsymbol{f} := J^{-1}\boldsymbol{f}_0$ is the body force per unit of deformed volume.

Remark 2. As an alternative, the left hand side of (18) (typically expressed in terms of a moving domain $\Omega(t)$) can be pulled back to the undeformed configuration Ω_0, resulting in

$$\frac{d}{dt}\int_{\Omega(t)} \mathbf{U}\, d\Omega = \frac{d}{dt}\int_{\Omega_0} J\mathbf{U}\, d\Omega_0 = \frac{d}{dt}\int_{\Omega_0} \mathcal{U}\, d\Omega_0. \tag{20}$$

For closure of the above system (19a)–(19d), a suitable constitutive relation is thus required by relating the Cauchy stress tensor $\boldsymbol{\sigma}$ (or the Kirchhoff stress tensor $\boldsymbol{\tau}$) with the geometric strain variables $\{\boldsymbol{F}, \boldsymbol{H}, J\}$. Such expressions can be easily derived from the standard relationship between these tensors [63]

$$J\boldsymbol{\sigma} = \boldsymbol{\tau} = \boldsymbol{P}\boldsymbol{F}^T. \tag{21}$$

To achieve this, it is important to substitute equation (15) into (21) for $\boldsymbol{P}$, and noting that $\boldsymbol{H}\boldsymbol{F}^T = J\boldsymbol{I}$, which gives the resulting expression for the Kirchhoff stresses [51]

$$J\boldsymbol{\sigma} = \boldsymbol{\tau} = \boldsymbol{\tau}_{\boldsymbol{F}} + \boldsymbol{\tau}_{\boldsymbol{H}} \times \boldsymbol{I} + \tau_J \boldsymbol{I}, \tag{22}$$

where

$$\boldsymbol{\tau}_{\boldsymbol{F}} := \boldsymbol{\Sigma}_{\boldsymbol{F}}\boldsymbol{F}^T; \qquad \boldsymbol{\tau}_{\boldsymbol{H}} := \boldsymbol{\Sigma}_{\boldsymbol{H}}\boldsymbol{H}^T; \qquad \tau_J := J\Sigma_J. \tag{23}$$

3. Finite volume spatial discretisation

3.1. Dual mesh and area vectors

The vertex centred finite volume spatial discretisation presented in this work requires the generation of a dual mesh for the definition of control volumes. Specifically, the median dual approach for tetrahedral meshes is chosen. This approach constructs the dual mesh by connecting edge midpoints with element centroids in two dimensions (see Fig. 3a) and edge midpoints with face centroids and element centroids in three dimensions. For a given edge connecting nodes *a* and *b* (see Fig. 3c), the mean undeformed area vector is defined as

$$\boldsymbol{C}_{ab} = \sum_{k\in\Gamma_{ab}} A_k \boldsymbol{N}_k. \tag{24}$$

Here, Γ_{ab} is the set of facets belonging to edge ab, A_k and $\boldsymbol{N}_k$ are the area and the material outward unit normal of a given facet k, respectively. Essentially, these area vectors satisfy the reciprocal relation $\boldsymbol{C}_{ab} = -\boldsymbol{C}_{ba}$, which allows for a substantial cost reduction in evaluating the control volume interface fluxes by saving an additional loop on facets per edge ab [45].

Similarly, the mean deformed area vector of a given edge ab becomes

$$\boldsymbol{c}_{ab} = \sum_{k \in \Gamma_{ab}} a_k \boldsymbol{n}_k, \tag{25}$$

where a_k and $\boldsymbol{n}_k$ denote the area and its corresponding outward unit normal on the deformed facet k. In the case of a boundary edge, the contribution of the boundary faces to which it belongs has to be taken into account. This set of boundary faces will be defined as Λ_a^B (refer to Fig. 3b).

3.2. Total Lagrangian discrete formulation

With this in mind, expression (4) can now be integrated in space over an undeformed control volume Ω_0^a, followed by the Green-Gauss divergence theorem, to give

$$\Omega_0^a \frac{d\boldsymbol{\mathcal{U}}_a}{dt} = -\int_{\partial\Omega_0^a} \boldsymbol{\mathcal{F}}_{\boldsymbol{N}}\, dA + \Omega_0^a \boldsymbol{\mathcal{S}}_a. \tag{26}$$

Here, $\boldsymbol{\mathcal{U}}_a$ and $\boldsymbol{\mathcal{S}}_a$ are the average values of both the conservation variables and source term vector within the control volume, respectively, and the normal flux $\boldsymbol{\mathcal{F}}_{\boldsymbol{N}}$ is already defined in (7).

The surface integral of (26) is approximated by means of an upwinding numerical flux [46]

$$\Omega_0^a \frac{d\boldsymbol{\mathcal{U}}_a}{dt} = -\left(\sum_{b \in \Lambda_a} \sum_{k \in \Gamma_{ab}} \boldsymbol{\mathcal{F}}^C_{\boldsymbol{N}_k} A_k + \sum_{\gamma \in \Lambda_a^B} \boldsymbol{\mathcal{F}}_a^\gamma \boldsymbol{C}_\gamma \right) + \Omega_0^a \boldsymbol{\mathcal{S}}_a, \tag{27}$$

where $b \in \Lambda_a$ represents the set of neighbouring control volumes b associated with the control volume a, $\boldsymbol{C}_\gamma := \frac{A_\gamma}{3}\boldsymbol{N}_\gamma$ represents the (tributary) boundary area vector and $\boldsymbol{\mathcal{F}}^C_{\boldsymbol{N}_k} = \boldsymbol{\mathcal{F}}^C_{\boldsymbol{N}}(\boldsymbol{\mathcal{U}}_k^-, \boldsymbol{\mathcal{U}}_k^+, \boldsymbol{N}_k)$ represents the numerical flux depending on the reconstructed states at both sides of the facet k, namely $\boldsymbol{\mathcal{U}}_k^-$ and $\boldsymbol{\mathcal{U}}_k^+$. In this type of scenario, (small) numerical jumps arise at each of the facets due to the use of discontinuous interpolations for the conservation variables. It is thus sufficient to employ an acoustic Riemann solver (derived on the basis of the Rankine-Hugoniot jump conditions) for the evaluation of the numerical flux, where now the shock speed U appearing in (8) is simply the speed of sound of a material [43].

However, it is clear that the above semi-discrete formulation (27) leads to an expensive computation of the numerical flux for each of the facets k belonging to a given edge ab. With the use of mean area vector defined in (24), a unique normal numerical flux $\boldsymbol{\mathcal{F}}^C_{\boldsymbol{N}_{ab}}$ can now be obtained by grouping all the facets associated with a given edge ab. This would simplify expression (27) to

$$\Omega_0^a \frac{d\boldsymbol{\mathcal{U}}_a}{dt} = -\left(\sum_{b \in \Lambda_a} \boldsymbol{\mathcal{F}}^C_{\boldsymbol{N}_{ab}} ||\boldsymbol{C}_{ab}|| + \sum_{\gamma \in \Lambda_a^B} \boldsymbol{\mathcal{F}}_a^\gamma \boldsymbol{C}_\gamma \right) + \Omega_0^a \boldsymbol{\mathcal{S}}_a, \tag{28}$$

where $\boldsymbol{\mathcal{F}}^C_{\boldsymbol{N}_{ab}} = \boldsymbol{\mathcal{F}}^C_{\boldsymbol{N}}(\boldsymbol{\mathcal{U}}_{ab}^-, \boldsymbol{\mathcal{U}}_{ab}^+, \boldsymbol{N}_{ab})$ is the Riemann-based numerical flux evaluated at the mid-edge of ab. Comparing equations (27) and (28), the former requires to store the complex facet stencil grouped at each edge, whereas the latter only requires to store the edge structure. This will enable expression (28) to be solved using a unique loop on edges, resulting into a computationally more efficient discretisation.[2] It is for this reason that equation (28) is preferred in this paper.

The terms within the parenthesis in (28) correspond to the evaluation of the control volume interface (and boundary) fluxes. This evaluation is comprised of a summation over edges (first term in the parenthesis) and a summation over boundary faces (second term in the parenthesis). In this second term, the weighted average stencil proposed by Löhner and co-authors [64] is used by computing the boundary flux over a boundary face γ in three dimensions as

$$\boldsymbol{\mathcal{F}}_a^\gamma = \frac{6\boldsymbol{\mathcal{F}}_a + \boldsymbol{\mathcal{F}}_b + \boldsymbol{\mathcal{F}}_c}{8}, \tag{29}$$

where b, c are the other two nodes that together with node a define boundary face γ.

It is worth noticing that equation (28) would only lead to a first order solution in space [43] provided that $\boldsymbol{\mathcal{U}}_{ab}^-$ and $\boldsymbol{\mathcal{U}}_{ab}^+$ are modelled following a piecewise constant representation. For instance, $\boldsymbol{\mathcal{U}}_{ab}^- = \boldsymbol{\mathcal{U}}_a$ and $\boldsymbol{\mathcal{U}}_{ab}^+ = \boldsymbol{\mathcal{U}}_b$, thus leading to excessive

[2] The use of this simplification does not compromise the overall accuracy of the scheme [45].

numerical dissipation in the solution. The physics of the problem can no longer be captured accurately unless excessively fine meshes are used, which is clearly undesirable especially for large scale problems in practice. To overcome this drawback, and to guarantee second order accuracy in space, a suitable linear reconstruction procedure is used. A detailed discussion of this reconstruction procedure can be found in [44].

For completeness, expression (28) is particularised for each individual component of $\mathcal{U}$, yielding

$$\Omega_a^0 \frac{d\boldsymbol{p}_a}{dt} = \sum_{b\in\Lambda_a} \boldsymbol{t}^C ||\boldsymbol{C}_{ab}|| + \sum_{\gamma\in\Gamma_a^B} \boldsymbol{t}_a^\gamma ||\boldsymbol{C}_\gamma|| + \Omega_a^0 \boldsymbol{f}_0^a; \tag{30a}$$

$$\Omega_a^0 \frac{d\boldsymbol{F}_a}{dt} = \sum_{b\in\Lambda_a} \frac{1}{\rho_0}\boldsymbol{p}^C \otimes \boldsymbol{C}_{ab} + \sum_{\gamma\in\Gamma_a^B} \frac{1}{\rho_0}\boldsymbol{p}_a^\gamma \otimes \boldsymbol{C}_\gamma; \tag{30b}$$

$$\Omega_a^0 \frac{d\boldsymbol{H}_a}{dt} = \sum_{b\in\Lambda_a} \boldsymbol{F}_{ab}^{\text{Ave}} \times \left(\frac{1}{\rho_0}\boldsymbol{p}^C \otimes \boldsymbol{C}_{ab}\right) + \sum_{\gamma\in\Gamma_a^B} \boldsymbol{F}_a^\gamma \times \left(\frac{1}{\rho_0}\boldsymbol{p}_a^\gamma \otimes \boldsymbol{C}_\gamma\right); \tag{30c}$$

$$\Omega_a^0 \frac{dJ_a}{dt} = \sum_{b\in\Lambda_a} \frac{1}{\rho_0}\boldsymbol{p}^C \cdot \left(\boldsymbol{H}_{ab}^{\text{Ave}} \boldsymbol{C}_{ab}\right) + \sum_{\gamma\in\Gamma_a^B} \frac{1}{\rho_0}\boldsymbol{p}_a^\gamma \cdot \left(\boldsymbol{H}_a^\gamma \boldsymbol{C}_\gamma\right). \tag{30d}$$

Here, the mappings are defined as $\boldsymbol{F}_{ab}^{\text{Ave}} := \frac{1}{2}(\boldsymbol{F}_a + \boldsymbol{F}_b)$ and $\boldsymbol{H}_{ab}^{\text{Ave}} := \frac{1}{2}(\boldsymbol{H}_a + \boldsymbol{H}_b)$ and $\{\boldsymbol{t}^C, \boldsymbol{p}^C\}$ are, respectively, the numerical approximation [44] for traction and linear momentum. It is important to emphasise that strong compatibility between the different kinematic fields $\{\boldsymbol{F}, \boldsymbol{H}, J\}$ is lost at the semi-discrete level. However, weak compatibility is maintained due to the coupled nature of the semi-discrete system of conservation equations.

For visualisation purposes, the current deformed geometry is recovered by integrating in time the discrete nodal velocity field obtained using (30a)

$$\frac{d\boldsymbol{x}_a}{dt} = \frac{\boldsymbol{p}_a}{\rho_0}. \tag{31}$$

Finally, the remaining unknowns to be defined in equations (30a)–(30d) are the numerical flux evaluation for $\{\boldsymbol{t}^C, \boldsymbol{p}^C\}$. This can be approximated via a characteristic based Riemann solver and will be discussed in the following section.

3.2.1. Riemann based upwinding stabilisation

To achieve this, recall first that the numerical flux across a discontinuous surface with normal $\boldsymbol{N}_{ab}$, namely $\mathcal{F}_{\boldsymbol{N}_{ab}}^C$, is generally described as

$$\mathcal{F}_{\boldsymbol{N}_{ab}}^C = \underbrace{\frac{1}{2}\left[\mathcal{F}_{\boldsymbol{N}_{ab}}(\mathcal{U}_{ab}^-) + \mathcal{F}_{\boldsymbol{N}_{ab}}(\mathcal{U}_{ab}^+)\right]}_{\text{Unstable flux}} \underbrace{- \frac{1}{2}\int_{\mathcal{U}_{ab}^-}^{\mathcal{U}_{ab}^+} |\mathcal{A}_{\boldsymbol{N}_{ab}}|\, d\mathcal{U}}_{\text{Upwinding stabilisation}}, \tag{32}$$

where $\{\mathcal{U}_{ab}^-, \mathcal{U}_{ab}^+\}$ represent the reconstructed states of the conservation variables at both sides of the mid-edge ab and the absolute value component of the flux Jacobian matrix is defined as $|\mathcal{A}_{\boldsymbol{N}_{ab}}| := \left|\frac{\partial \mathcal{F}_{\boldsymbol{N}_{ab}}}{\partial \mathcal{U}}\right| = \frac{1}{2}\sum_{\alpha=1}^{6} |c_\alpha| \mathcal{R}_\alpha \mathcal{L}_\alpha^T$ (refer to Appendix A in [44]). The first term on the right hand side of (32) denotes the unstable average flux, whereas the second term (i.e. upwinding stabilisation) can be interpreted as a consistent numerical stabilisation that counterbalances non-physical instabilities arising from the first term.

In this work, evaluation of $|\mathcal{A}_{\boldsymbol{N}_{ab}}|$ is carried out at the initial undeformed configuration (i.e. origin) by adopting $\boldsymbol{F} = \boldsymbol{H} = \boldsymbol{I}$ and $J = 1$. Furthermore, above unstable flux contribution (refer to the first term of (32)) can be approximated via a second order central difference scheme, which results in

$$\mathcal{F}_{\boldsymbol{N}_{ab}}^C = \underbrace{\frac{1}{2}\left[\mathcal{F}_{\boldsymbol{N}_{ab}}(\mathcal{U}_a) + \mathcal{F}_{\boldsymbol{N}_{ab}}(\mathcal{U}_b)\right]}_{\text{Central difference flux}} \underbrace{- \frac{1}{2}|\mathcal{A}_{\boldsymbol{N}_{ab}}|\left(\mathcal{U}_{ab}^+ - \mathcal{U}_{ab}^-\right)}_{\text{Upwinding stabilisation}}. \tag{33}$$

Interestingly, this type of central difference flux evaluation does not need to rely on the reconstructed states of the conservation variables $\mathcal{U}_{ab}^{-,+}$. A detailed derivation of the upwinding stabilisation term in (33) can be found in Reference [44] (see pg. 417 to pg. 420 in Section 4.3).

Following the exact same procedure reported in Reference [44], and after some algebraic manipulations, the Godunov-type numerical traction and linear momentum can be summarised here for completeness

$$\boldsymbol{t}^C = \boldsymbol{t}_{ab}^{\text{Ave}} + \boldsymbol{t}_{ab}^{\text{Stab}}; \qquad \boldsymbol{p}^C = \boldsymbol{p}_{ab}^{\text{Ave}} + \boldsymbol{p}_{ab}^{\text{Stab}}. \tag{34}$$

The (unstable) average states of both the traction and linear momentum are

$$\boldsymbol{t}_{ab}^{\text{Ave}} := \underbrace{\frac{1}{2}(\boldsymbol{P}_a + \boldsymbol{P}_b)}_{\boldsymbol{P}_{ab}^{\text{Ave}}} \boldsymbol{N}_{ab}; \qquad \boldsymbol{p}_{ab}^{\text{Ave}} := \frac{1}{2}(\boldsymbol{p}_a + \boldsymbol{p}_b), \tag{35}$$

and the corresponding upwinding stabilisation terms are

$$\boldsymbol{t}_{ab}^{\text{Stab}} := \frac{1}{2}\boldsymbol{S}_{ab}^{\boldsymbol{p}}(\boldsymbol{p}_{ab}^{+} - \boldsymbol{p}_{ab}^{-}); \qquad \boldsymbol{p}_{ab}^{\text{Stab}} := \frac{1}{2}\boldsymbol{S}_{ab}^{\boldsymbol{t}}\left[(\boldsymbol{P}_{ab}^{+} - \boldsymbol{P}_{ab}^{-})\boldsymbol{N}_{ab}\right], \tag{36}$$

with the (positive definite) stabilisation matrices being defined as

$$\boldsymbol{S}_{ab}^{\boldsymbol{p}} := c_p\,(\mathbf{n}_{ab} \otimes \mathbf{n}_{ab}) + c_s\,(\boldsymbol{I} - \mathbf{n}_{ab} \otimes \mathbf{n}_{ab})\,; \qquad \boldsymbol{S}_{ab}^{\boldsymbol{t}} := \frac{1}{c_p}\,(\mathbf{n}_{ab} \otimes \mathbf{n}_{ab}) + \frac{1}{c_s}\,(\boldsymbol{I} - \mathbf{n}_{ab} \otimes \mathbf{n}_{ab})\,. \tag{37}$$

In this case, the unit outward normal vector is

$$\mathbf{n}_{ab} := \frac{\mathbf{c}_{ab}}{||\mathbf{c}_{ab}||}; \qquad \mathbf{c}_{ab} := \boldsymbol{H}_{ab}^{\text{Ave}}\boldsymbol{C}_{ab}, \tag{38}$$

and c_p and c_s represent the elastic pressure wave speed and the elastic shear wave speed

$$c_p := \sqrt{\frac{\lambda + 2\mu}{\rho_0}}; \qquad c_s := \sqrt{\frac{\mu}{\rho_0}}, \tag{39}$$

respectively.

Remark 3. We need to point out that at the discrete level, the deformed area vector $\mathbf{c}_{ab}$ projected through $\boldsymbol{H}_{ab}^{\text{Ave}}$ (refer to (38)) does not necessarily coincide with the geometry-based $\boldsymbol{c}_{ab}$ of (25). For instance, $\mathbf{c}_{ab} \neq \boldsymbol{c}_{ab}$. However, in practice, the robustness of the overall algorithm would not be adversely affected regardless of which deformed area vector is used.

Substitution of (34) into (30a)–(30d) for $\{\boldsymbol{t}^C, \boldsymbol{p}^C\}$ yields the following semi-discrete nodal update for the $\{\boldsymbol{p}, \boldsymbol{F}, \boldsymbol{H}, J\}$ Total Lagrangian equations as

$$\Omega_a^0 \frac{d\boldsymbol{p}_a}{dt} = \left[\sum_{b\in\Lambda_a} \boldsymbol{P}_{ab}^{\text{Ave}}\boldsymbol{C}_{ab} + \sum_{\gamma\in\Lambda_a^B} \boldsymbol{t}_a^{\gamma}||\boldsymbol{C}_{\gamma}|| + \Omega_a^0 \boldsymbol{f}_0^a\right] + \sum_{b\in\Lambda_a} \mathcal{D}_{ab}^{\boldsymbol{p}}; \tag{40a}$$

$$\Omega_a^0 \frac{d\boldsymbol{F}_a}{dt} = \left[\sum_{b\in\Lambda_a} \frac{1}{\rho_0}\boldsymbol{p}_{ab}^{\text{Ave}} \otimes \boldsymbol{C}_{ab} + \sum_{\gamma\in\Lambda_a^B} \frac{1}{\rho_0}\boldsymbol{p}_a^{\gamma} \otimes \boldsymbol{C}_{\gamma}\right] + \sum_{b\in\Lambda_a} \mathcal{D}_{ab}^{\boldsymbol{F}}; \tag{40b}$$

$$\Omega_a^0 \frac{d\boldsymbol{H}_a}{dt} = \left[\sum_{b\in\Lambda_a} \boldsymbol{F}_{ab}^{\text{Ave}} \times \left(\frac{1}{\rho_0}\boldsymbol{p}^{\text{Ave}} \otimes \boldsymbol{C}_{ab}\right) + \sum_{\gamma\in\Lambda_a^B} \boldsymbol{F}_a^{\gamma} \times \left(\frac{1}{\rho_0}\boldsymbol{p}_a^{\gamma} \otimes \boldsymbol{C}_{\gamma}\right)\right] + \sum_{b\in\Lambda_a} \mathcal{D}_{ab}^{\boldsymbol{H}}; \tag{40c}$$

$$\Omega_a^0 \frac{dJ_a}{dt} = \left[\sum_{b\in\Lambda_a} \frac{1}{\rho_0}\boldsymbol{p}_{ab}^{\text{Ave}} \cdot \left(\boldsymbol{H}_{ab}^{\text{Ave}}\boldsymbol{C}_{ab}\right) + \sum_{\gamma\in\Lambda_a^B} \frac{1}{\rho_0}\boldsymbol{p}_a^{\gamma} \cdot \left(\boldsymbol{H}_a^{\gamma}\boldsymbol{C}_{\gamma}\right)\right] + \sum_{b\in\Lambda_a} \mathcal{D}_{ab}^{J}. \tag{40d}$$

Here, $\{\mathcal{D}_{ab}^{\boldsymbol{p}}, \mathcal{D}_{ab}^{\boldsymbol{F}}, \mathcal{D}_{ab}^{\boldsymbol{H}}, \mathcal{D}_{ab}^{J}\}$ correspond to the upwinding stabilisation terms expressed as

$$\mathcal{D}_{ab}^{\boldsymbol{p}} = \boldsymbol{t}_{ab}^{\text{Stab}}||\boldsymbol{C}_{ab}||; \tag{41}$$

and

$$\mathcal{D}_{ab}^{\boldsymbol{F}} = \frac{1}{\rho_0}\boldsymbol{p}_{ab}^{\text{Stab}} \otimes \boldsymbol{C}_{ab}; \quad \mathcal{D}_{ab}^{\boldsymbol{H}} = \boldsymbol{F}_{ab}^{\text{Ave}} \times \left(\frac{1}{\rho_0}\boldsymbol{p}_{ab}^{\text{Stab}} \otimes \boldsymbol{C}_{ab}\right); \quad \mathcal{D}_{ab}^{J} = \frac{1}{\rho_0}\boldsymbol{p}_{ab}^{\text{Stab}} \cdot \left(\boldsymbol{H}_{ab}^{\text{Ave}}\boldsymbol{C}_{ab}\right). \tag{42}$$

In ensuring discrete satisfaction of the involutions (3), we must not introduce any numerical dissipation into (40b) and (40c) by setting the values of $\mathcal{D}_{ab}^{\boldsymbol{F}} = \mathcal{D}_{ab}^{\boldsymbol{H}} = \boldsymbol{0}$. Additionally, and following the work of [65], the strain variables $\left\{\boldsymbol{F}_{ab}^{\text{Ave}}, \boldsymbol{F}_a^{\gamma}\right\}$ and $\left\{\boldsymbol{H}_{ab}^{\text{Ave}}, \boldsymbol{H}_a^{\gamma}\right\}$ appearing in the square bracket terms of (40c)–(40d) will be replaced by $\boldsymbol{F}_a$ and $\boldsymbol{H}_a$. This implies that the updates for $\boldsymbol{F}$ and $\boldsymbol{H}$ are naturally curl- and divergence-free as their semi-discrete equations are formulated in terms of a material discrete gradient of a continuous velocity field [49]. By doing this, the geometric conservation equations (40b)-(40d) reduce to

$$\Omega_a^0 \frac{d\boldsymbol{F}_a}{dt} = \sum_{b\in\Lambda_a} \frac{1}{\rho_0} \boldsymbol{p}_{ab}^{\text{Ave}} \otimes \boldsymbol{C}_{ab} + \sum_{\gamma\in\Lambda_a^B} \frac{1}{\rho_0} \boldsymbol{p}_a^{\gamma} \otimes \boldsymbol{C}_{\gamma}; \tag{43a}$$

$$\Omega_a^0 \frac{d\boldsymbol{H}_a}{dt} = \boldsymbol{F}_a \times \left(\sum_{b\in\Lambda_a} \frac{1}{\rho_0} \boldsymbol{p}_{ab}^{\text{Ave}} \otimes \boldsymbol{C}_{ab} + \sum_{\gamma\in\Lambda_a^B} \frac{1}{\rho_0} \boldsymbol{p}_a^{\gamma} \otimes \boldsymbol{C}_{\gamma} \right); \tag{43b}$$

$$\Omega_a^0 \frac{dJ_a}{dt} = \boldsymbol{H}_a : \left(\sum_{b\in\Lambda_a} \frac{1}{\rho_0} \boldsymbol{p}_{ab}^{\text{Ave}} \otimes \boldsymbol{C}_{ab} + \sum_{\gamma\in\Lambda_a^B} \frac{1}{\rho_0} \boldsymbol{p}_a^{\gamma} \otimes \boldsymbol{C}_{\gamma} \right) + \sum_{b\in\Lambda_a} \mathcal{D}_{ab}^{J}. \tag{43c}$$

Notice here that the upwinding stabilisation is only applied to the linear momentum evolution $\boldsymbol{\mathcal{D}}_{ab}^{\boldsymbol{p}}$ (40a) and the volume map evolution $\mathcal{D}_{ab}^{J}$ (43c). The former alleviates the appearance of spurious zero-energy (hourglass-like) modes, whereas the latter removes pressure instabilities in near incompressibility [49].

Remark 4. It is worth noticing that the above semi-discrete system (e.g. (40a) and (43a)–(43c)) guarantees a non-negative production of (numerical) entropy for every edge, provided that the following two conditions are fulfilled:

- the term $\boldsymbol{p}_{ab}^{\text{Stab}}$ (36b) appearing in $\mathcal{D}_{ab}^{J}$ (43c) is re-defined as $\boldsymbol{p}_{ab}^{\text{Stab}} := \frac{1}{2}\boldsymbol{S}_{ab}^{\boldsymbol{t}} \left[(\Sigma_{J,ab}^{+} - \Sigma_{J,ab}^{-}) \boldsymbol{H}_{ab}^{\text{Ave}} \boldsymbol{N}_{ab} \right]$; and
- both stabilisation matrices $\{\boldsymbol{\mathcal{S}}_{ab}^{\boldsymbol{p}}, \boldsymbol{\mathcal{S}}_{ab}^{\boldsymbol{t}}\}$ (37) are positive semi-definite (second order) tensors.

For the sake of complenetess of this work, detailed proof of the edge based entropy production is included in Appendix A.

3.3. Updated Lagrangian discrete formulation

Following the discretisation procedure presented in equations (40a) and (43a)–(43c), the nodal update for the $\{\boldsymbol{p}, \boldsymbol{F}, \boldsymbol{H}, J\}$ equations (19a)–(19d) follows

$$\Omega_a^0 \frac{d\boldsymbol{p}_a}{dt} = \sum_{b\in\Lambda_a} \boldsymbol{\sigma}_{ab}^{\text{Ave}} \boldsymbol{c}_{ab} + \sum_{\gamma\in\Lambda_a^B} \boldsymbol{t}_a^{\gamma} ||\boldsymbol{c}_{\gamma}|| + \Omega_a(t) \boldsymbol{f}^a + \sum_{b\in\Lambda_a} \boldsymbol{D}_{ab}^{\boldsymbol{p}}; \tag{44a}$$

$$\Omega_a^0 \frac{d\boldsymbol{F}_a}{dt} = \sum_{b\in\Lambda_a} \frac{1}{\rho_0} \boldsymbol{p}_{ab}^{\text{Ave}} \otimes \left[\left(\boldsymbol{H}_{ab}^{\text{Ave}} \right)^{-1} \boldsymbol{c}_{ab} \right] + \sum_{\gamma\in\Lambda_a^B} \frac{1}{\rho_0} \boldsymbol{p}_a^{\gamma} \otimes \left[\boldsymbol{H}_a^{-1} \boldsymbol{c}_{\gamma} \right]; \tag{44b}$$

$$\Omega_a^0 \frac{d\boldsymbol{H}_a}{dt} = \boldsymbol{F}_a \times \left(\sum_{b\in\Lambda_a} \frac{1}{\rho_0} \boldsymbol{p}_{ab}^{\text{Ave}} \otimes \left[\left(\boldsymbol{H}_{ab}^{\text{Ave}} \right)^{-1} \boldsymbol{c}_{ab} \right] + \sum_{\gamma\in\Lambda_a^B} \frac{1}{\rho_0} \boldsymbol{p}_a^{\gamma} \otimes \left[\boldsymbol{H}_a^{-1} \boldsymbol{c}_{\gamma} \right] \right); \tag{44c}$$

$$\Omega_a^0 \frac{dJ_a}{dt} = \sum_{b\in\Lambda_a} \frac{1}{\rho_0} \boldsymbol{p}_{ab}^{\text{Ave}} \cdot \boldsymbol{c}_{ab} + \sum_{\gamma\in\Lambda_a^B} \frac{1}{\rho_0} \boldsymbol{p}_a^{\gamma} \cdot \boldsymbol{c}_{\gamma} + \sum_{b\in\Lambda_a} D_{ab}^{J}, \tag{44d}$$

where the area vector is defined as $\boldsymbol{c}_{\gamma} := \boldsymbol{n}_{\gamma} \frac{a_{\gamma}}{3}$ and the average Cauchy stress tensor is given by $\boldsymbol{\sigma}_{ab}^{\text{Ave}} = \frac{1}{2}(\boldsymbol{\sigma}_a + \boldsymbol{\sigma}_b)$. It is clear that, for computational efficiency, terms on the left hand side of (19a)–(19d) typically expressed in terms of a moving domain $\Omega(t)$, are now evaluated at the initial undeformed domain Ω_0 (refer to (20)).

Moreover, the stabilisation term $\boldsymbol{D}_{ab}^{\boldsymbol{p}}$ described in the Updated Lagrangian linear momentum evolution (44a) is the push forward equivalent of $\boldsymbol{\mathcal{D}}_{ab}^{\boldsymbol{p}}$ (41). This can be achieved by substituting (36a) into (41) for $\boldsymbol{t}_{ab}^{\text{Stab}}$, and noticing that

$$||\boldsymbol{C}_{ab}||^2 = \boldsymbol{C}_{ab} \cdot \boldsymbol{C}_{ab} = \left[\left(\boldsymbol{H}_{ab}^{\text{Ave}} \right)^{-1} \boldsymbol{c}_{ab} \right] \cdot \left[\left(\boldsymbol{H}_{ab}^{\text{Ave}} \right)^{-1} \boldsymbol{c}_{ab} \right], \tag{45}$$

which results in

$$\boldsymbol{D}_{ab}^{\boldsymbol{p}} = \left(\frac{1}{2} \boldsymbol{S}_{ab}^{\boldsymbol{p}} (\boldsymbol{p}_{ab}^{+} - \boldsymbol{p}_{ab}^{-}) \right) \left(\left[\left(\boldsymbol{H}_{ab}^{\text{Ave}} \right)^{-1} \boldsymbol{c}_{ab} \right] \cdot \left[\left(\boldsymbol{H}_{ab}^{\text{Ave}} \right)^{-1} \boldsymbol{c}_{ab} \right] \right)^{\frac{1}{2}}. \tag{46}$$

On the other hand, the term D_{ab}^{J} becomes

$$D_{ab}^{J} = \frac{1}{\rho_0} \left[\frac{1}{2} \boldsymbol{S}_{ab}^{\boldsymbol{t}} (\boldsymbol{\sigma}_{ab}^{+} - \boldsymbol{\sigma}_{ab}^{-}) \frac{\boldsymbol{c}_{ab}}{||\boldsymbol{C}_{ab}||} \right] \cdot \boldsymbol{c}_{ab}. \tag{47}$$

Referring to Remark 3, since $\left(\boldsymbol{H}^{\text{Ave}}_{ab}\right)^{-1}\boldsymbol{c}_{ab} \neq \boldsymbol{C}_{ab}$ and $\boldsymbol{H}^{-1}_{a}\boldsymbol{c}_{\gamma} \neq \boldsymbol{C}_{\gamma}$, it is clear that the update of $\dot{\boldsymbol{F}}$ (44b) and $\dot{\boldsymbol{H}}$ (44c) is no longer dependent on a material discrete gradient of a continuous velocity field, thus violating the discrete satisfaction of the involutions. This can be remedied by adopting a locally area map projection procedure so that the area maps $\{\boldsymbol{H}^{\text{Ave}}_{ab}, \boldsymbol{H}_a\}$ on the right hand side of (44b)–(44c) are suitably modified. The modified area maps $\{\mathbf{H}^{\text{Ave}}_{ab}, \mathbf{H}_a\}$ will then satisfy the following conditions, namely $\left(\mathbf{H}^{\text{Ave}}_{ab}\right)^{-1}\boldsymbol{c}_{ab} = \boldsymbol{C}_{ab}$ and $\mathbf{H}^{-1}_{a}\boldsymbol{c}_{\gamma} = \boldsymbol{C}_{\gamma}$, which will be discussed in Appendix B.

3.3.1. Complete Upwind-ULF

Replacing $\{\boldsymbol{H}^{\text{Ave}}_{ab}, \boldsymbol{H}_a\}$ with $\{\mathbf{H}^{\text{Ave}}_{ab}, \mathbf{H}_a\}$ in the system (44a)–(44d), and noting that $\boldsymbol{C}_{ab} = \left(\mathbf{H}^{\text{Ave}}_{ab}\right)^{-1}\boldsymbol{c}_{ab}$ and $\boldsymbol{C}_{\gamma} = \mathbf{H}^{-1}_{a}\boldsymbol{c}_{\gamma}$, yields

$$\Omega^0_a \frac{d\boldsymbol{p}_a}{dt} = \sum_{b\in\Lambda_a} \boldsymbol{\sigma}^{\text{Ave}}_{ab}\boldsymbol{c}_{ab} + \sum_{\gamma\in\Gamma^B_a} \boldsymbol{t}^{\gamma}_{a}\,||\boldsymbol{c}_{\gamma}|| + \Omega_a(t)\,\boldsymbol{f}^a + \sum_{b\in\Lambda_a} \boldsymbol{D}^{\boldsymbol{p}}_{ab}; \tag{48a}$$

$$\Omega^0_a \frac{d\boldsymbol{F}_a}{dt} = \sum_{b\in\Lambda_a} \frac{1}{\rho_0}\boldsymbol{p}^{\text{Ave}}_{ab} \otimes \boldsymbol{C}_{ab} + \sum_{\gamma\in\Gamma^B_a} \frac{1}{\rho_0}\boldsymbol{p}^{\gamma}_{a} \otimes \boldsymbol{C}_{\gamma} \tag{48b}$$

$$\Omega^0_a \frac{d\boldsymbol{H}_a}{dt} = \boldsymbol{F}_a \boldsymbol{\times} \left(\sum_{b\in\Lambda_a} \frac{1}{\rho_0}\boldsymbol{p}^{\text{Ave}}_{ab} \otimes \boldsymbol{C}_{ab} + \sum_{\gamma\in\Gamma^B_a} \frac{1}{\rho_0}\boldsymbol{p}^{\gamma}_{a} \otimes \boldsymbol{C}_{\gamma} \right) \tag{48c}$$

$$\Omega^0_a \frac{dJ_a}{dt} = \sum_{b\in\Lambda_a} \frac{1}{\rho_0}\boldsymbol{p}^{\text{Ave}}_{ab} \cdot \boldsymbol{c}_{ab} + \sum_{\gamma\in\Gamma^B_a} \frac{1}{\rho_0}\boldsymbol{p}^{\gamma}_{a} \cdot \boldsymbol{c}_{\gamma} + \sum_{b\in\Lambda_a} D^{J}_{ab}. \tag{48d}$$

In this particular case, $\mathbf{c}_{ab} = \boldsymbol{c}_{ab}$ and $\mathbf{n}_{ab} = \boldsymbol{n}_{ab} := \frac{\boldsymbol{c}_{ab}}{||\boldsymbol{c}_{ab}||}$. This implies that the time update for $\{\boldsymbol{p}_a, J_a\}$ (see (48a) and (48d)) is carried out in the Updated Lagrangian form, whereas the update for the remaining conservation variables $\{\boldsymbol{F}_a, \boldsymbol{H}_a\}$ (see (48b) and (48c)) is carried out in an identical manner to the Total Lagrangian formulation.

In comparison to the complete set of Total Lagrangian discretised equations (40a)–(40d), it is clear that the update of the $\{\boldsymbol{p}, \boldsymbol{F}, \boldsymbol{H}, J\}$ Updated Lagrangian equations (48a)–(48d) is more computationally demanding as the evaluation of mesh based area vectors $\{\boldsymbol{c}_{ab}, \boldsymbol{c}_{\gamma}\}$ in (48a) and (48d) is required for every time step during the time integration process.

Remark 5. Aiming to eliminate the need to construct the median dual mesh for every time step of the time integration process, one viable option is to update the time dependent area vectors $\{\boldsymbol{c}_{ab}, \boldsymbol{c}_{\gamma}\}$ via the geometry based area map $\boldsymbol{H}_{\boldsymbol{x}} := \frac{1}{2}\left(\nabla_0\boldsymbol{x} \boldsymbol{\times} \nabla_0\boldsymbol{x}\right)$, defined as

$$\tilde{\boldsymbol{c}}_{ab} := \boldsymbol{H}^{\text{Ave}}_{\boldsymbol{x},ab}\boldsymbol{C}_{ab} \qquad \text{and} \qquad \tilde{\boldsymbol{c}}_{\gamma} := \boldsymbol{H}^{a}_{\boldsymbol{x}}\boldsymbol{C}_{\gamma} \qquad \text{with} \qquad \gamma \in \Lambda^B_a. \tag{49}$$

Here, the average state of the geometry based area map is defined as $\boldsymbol{H}^{\text{Ave}}_{\boldsymbol{x},ab} := \frac{1}{2}\left(\boldsymbol{H}^{a}_{\boldsymbol{x}} + \boldsymbol{H}^{b}_{\boldsymbol{x}}\right)$ and the material gradient of the spatial geometry for an arbitrary control volume a can be approximated as $\nabla_0\boldsymbol{x}_a \approx \frac{1}{\Omega^0_a}\sum_{b\in\Lambda_a}\boldsymbol{x}^{\text{Ave}}_{ab} \otimes \boldsymbol{C}_{ab}$ with $\boldsymbol{x}^{\text{Ave}}_{ab} := \frac{1}{2}\left(\boldsymbol{x}_a + \boldsymbol{x}_b\right)$.

4. Time integrator

Insofar as the resulting set of semi-discrete equations is rather large, it will only be suitable to employ an explicit type of time integrator. In this work, an explicit one-step two-stage Total Variation Diminishing Runge-Kutta (TVD-RK) scheme is used [43,45,46,66]. This is described by the following time update equations from time step t^n to t^{n+1}

$$\mathcal{U}^{\star}_a = \mathcal{U}^{n}_a + \Delta t\,\dot{\mathcal{U}}^{n}_a(\mathcal{U}^{n}_a, t^n); \qquad \mathcal{U}^{\star\star}_a = \mathcal{U}^{\star}_a + \Delta t\,\dot{\mathcal{U}}^{\star}_a(\mathcal{U}^{\star}_a, t^{n+1}); \qquad \mathcal{U}^{n+1}_a = \frac{1}{2}(\mathcal{U}^{n}_a + \mathcal{U}^{\star\star}_a), \tag{50}$$

where overdot represents differentiation with respect to time.

In this work, a monolithic time integration procedure is used where the conservation variables $\boldsymbol{\mathcal{U}} = \{\boldsymbol{p}, \boldsymbol{F}, \boldsymbol{H}, J\}$ along with the geometry $\boldsymbol{x}$ are all updated via expression (50). The maximum allowable time step $\Delta t = t^{n+1} - t^n$ is governed by the standard Courant-Friedrichs-Lewy (CFL) condition [67] given as

$$\Delta t = \alpha_{\text{CFL}}\frac{h_{\min}}{c_{p,\max}}, \tag{51}$$

where $c_{p,\max}$ is the maximum pressure wave speed, $h_{\min}$ is the minimum characteristic length within the computational domain (defined in our case as the smallest mesh element length) and α_{CFL} is the CFL stability number. For the numerical examples presented in this paper, a value of $\alpha_{\text{CFL}} = 0.3$ has been chosen to ensure both the accuracy and stability of the algorithm.

The proposed algorithm does not necessarily fulfil the conservation of angular momentum of the system, as the minors of the deformation gradient tensor, namely $\{\boldsymbol{F}, \boldsymbol{H}, J\}$, are no longer computed on the basis of the material gradient of a current geometry (e.g. $\boldsymbol{F} \neq \boldsymbol{F}_{\boldsymbol{x}} := \nabla_0 \boldsymbol{x}$, $\boldsymbol{H} \neq \boldsymbol{H}_{\boldsymbol{x}} := \frac{1}{2}\boldsymbol{F}_{\boldsymbol{x}} \times \boldsymbol{F}_{\boldsymbol{x}}$, $J \neq J_{\boldsymbol{x}} := \frac{1}{6}\boldsymbol{F}_{\boldsymbol{x}} : (\boldsymbol{F}_{\boldsymbol{x}} \times \boldsymbol{F}_{\boldsymbol{x}})$) [51]. In our experience, this can have a negative effect in those problems involving very large and sustained rotations. To rectify this, and taking inspiration from the work of [44], a global least-square angular momentum projection procedure is carried out. The linear momentum update (see (40a) or (48a)) is suitably modified (in the least squares sense) in order to preserve the total angular momentum whilst still ensuring the conservation of the overall linear momentum. Details of this projection technique can be found in Reference [44].

5. Artificial compressibility: total Lagrangian formulation

5.1. General remark

As it is well known, in the case of nearly (or truly) incompressible materials, the pressure wave speed c_p can reach very large (or even infinitely large) values leading to prohibitively small time steps. This can have a very negative effect on the computational efficiency of any time-explicit algorithm. One popular approach to address this issue is the employment of the artificial compressibility method, originally developed for the Navier-Stokes equations [68]. Taking inspiration from the work of Gil and co-authors [49,55], the artificial compressibility approach is here adapted to the system of Total Lagrangian conservation equations as presented in (1a), (1b), (11).

To achieve this, we must first re-write the Jacobian conservation law (1d) in terms of its entropy conjugate (pressure),

$$\frac{1}{\kappa}\frac{\partial p}{\partial t} = \boldsymbol{H} : \nabla_0 \left(\frac{\boldsymbol{p}}{\rho_0} \right). \tag{52}$$

In this case, the new unknowns of the problem are $\{\boldsymbol{p}, \boldsymbol{F}, \boldsymbol{H}, p\}$ ((1a), (1b), (11a), (52)) and this permits to (naturally) consider the degenerate case of strict incompressibility.

With the idea to pursue a fractional step type approach, we must first discretise the continuum equations listed above in time and then proceed to their discretisation in space.[3] In addition, whilst conservation equations for $\{\boldsymbol{F}, \boldsymbol{H}\}$ will still be solved explicitly, equations for $\{\boldsymbol{p}, p\}$ will now be treated semi-implicitly in order to enforce the incompressibility constraint without compromising the size of the time step, namely

$$\frac{\boldsymbol{p}^{n+1} - \boldsymbol{p}^n}{\Delta t} - \mathrm{DIV}\boldsymbol{P}(\boldsymbol{F}^n, \boldsymbol{H}^n, p^{n+1}) - \boldsymbol{f}_0^n = \boldsymbol{0}; \tag{53a}$$

$$\frac{1}{\kappa}\frac{p^{n+1} - p^n}{\Delta t} - \boldsymbol{H}^n : \nabla_0 \left(\frac{\boldsymbol{p}^{n+1}}{\rho_0} \right) = 0. \tag{53b}$$

As typically adopted in fractional step methods, we now split the time integration over a time step Δt into two consecutive steps, an intermediate explicit predictor followed by an implicit projection corrector. Therefore, the first (intermediate predictor) step is defined as

$$\frac{\boldsymbol{p}^{\mathrm{int}} - \boldsymbol{p}^n}{\Delta t} - \mathrm{DIV}\boldsymbol{P}(\boldsymbol{F}^n, \boldsymbol{H}^n, p^n) - \boldsymbol{f}_0^n = \boldsymbol{0}; \tag{54a}$$

$$\frac{\boldsymbol{F}^{n+1} - \boldsymbol{F}^n}{\Delta t} - \nabla_0 \left(\frac{\boldsymbol{p}^n}{\rho_0} \right) = \boldsymbol{0}; \tag{54b}$$

$$\frac{\boldsymbol{H}^{n+1} - \boldsymbol{H}^n}{\Delta t} - \boldsymbol{F}^n \times \nabla_0 \left(\frac{\boldsymbol{p}^n}{\rho_0} \right) = \boldsymbol{0}; \tag{54c}$$

$$\frac{1}{\kappa}\frac{p^{\mathrm{int}} - p^n}{\Delta t} - \boldsymbol{H}^n : \nabla_0 \left(\frac{\boldsymbol{p}^n}{\rho_0} \right) = 0. \tag{54d}$$

The second (corrector or projection) step becomes

$$\frac{\left(\boldsymbol{p}^{n+1} - \boldsymbol{p}^{\mathrm{int}}\right)}{\Delta t} - \mathrm{DIV}\left[\left(p^{n+1} - p^n\right)\boldsymbol{H}^n\right] = \boldsymbol{0}; \tag{55a}$$

$$\frac{1}{\kappa}\frac{\left(p^{n+1} - p^{\mathrm{int}}\right)}{\Delta t} - \boldsymbol{H}^n : \nabla_0 \left(\frac{\boldsymbol{p}^{n+1}}{\rho_0} - \frac{\boldsymbol{p}^n}{\rho_0} \right) = 0. \tag{55b}$$

It is important to notice that addition of equations (54a) and (55a) (and (54d) and (55b)) recovers the original equations (53a) ((53b)). For nearly (and truly) incompressible materials, the bulk modulus present in the first term of equation (54d)

[3] This is the opposite to what it is typically done in the so-called method of lines.

can potentially reach very high values (even infinite), which can destroy the explicit nature of the predictor step of the scheme. It is for this reason that a fictitious (thus the name of artificial compressibility) bulk modulus $\tilde{\kappa}$ is used in its place, yielding

$$\frac{1}{\tilde{\kappa}}\frac{p^{\text{int}}-p^n}{\Delta t}-\boldsymbol{H}^n:\nabla_0\left(\frac{\boldsymbol{p}^n}{\rho_0}\right)=0. \tag{56}$$

As a result of this, the projection step of the pressure equation (55b) now becomes (to ensure consistency)

$$\frac{1}{\kappa}\frac{\left(p^{n+1}-p^n\right)}{\Delta t}-\frac{1}{\tilde{\kappa}}\frac{p^{\text{int}}-p^n}{\Delta t}-\boldsymbol{H}^n:\nabla_0\left(\frac{\boldsymbol{p}^{n+1}}{\rho_0}-\frac{\boldsymbol{p}^n}{\rho_0}\right)=0. \tag{57}$$

After advancing explicitly the predictor step, the corrector step must be solved ((55a) and (57)). In this case, and in order to preserve a matrix free approach, the artificial compressibility method is further exploited. This is typically achieved by introducing artificial "pseudo-time" derivative terms which permit to explicitly evolve the corrector equations in pseudo-time until convergence. This gives,

$$\frac{\partial \boldsymbol{p}}{\partial \tau}=\text{DIV}\left[\left(p^{n+1}-p^n\right)\boldsymbol{H}^n\right]-\frac{\left(\boldsymbol{p}^{n+1}-\boldsymbol{p}^{\text{int}}\right)}{\Delta t}; \tag{58a}$$

$$\frac{1}{\gamma}\frac{\partial p}{\partial \tau}=\frac{1}{\tilde{\kappa}}\frac{p^{\text{int}}-p^n}{\Delta t}+\boldsymbol{H}^n:\nabla_0\left(\frac{\boldsymbol{p}^{n+1}}{\rho_0}-\frac{\boldsymbol{p}^n}{\rho_0}\right)-\frac{1}{\kappa}\frac{\left(p^{n+1}-p^n\right)}{\Delta t}, \tag{58b}$$

where $\frac{\partial}{\partial \tau}$ represents the pseudo-time derivative terms and γ denotes the so-called artificial compressibility parameter. In this work, the pseudo-time terms are discretised in time using exactly the same time integrator as described in (50).

Once the time semi-discretisation is concluded, spatial semi-discretisation is then necessary. The upwind finite volume spatial discretisation for the predictor-corrector system (54a), (54b), (54c), (56), (58a), (58b) will now be presented.

5.2. FVM artificial compressibility algorithm

Following the upwind FVM discretisation procedure presented in Section 3.2, the predictor step of the mixed-based system $\{\boldsymbol{p},\boldsymbol{F},\boldsymbol{H},p\}$ becomes,

$$\Omega_a^0\left[\frac{\boldsymbol{p}_a^{\text{int}}-\boldsymbol{p}_a^n}{\Delta t}\right]=\sum_{b\in\Lambda_a}\boldsymbol{P}_{ab}^{\text{Ave},n}\boldsymbol{C}_{ab}+\sum_{\gamma\in\Gamma_a^B}\boldsymbol{t}_a^{\gamma,n}||\boldsymbol{C}_\gamma||+\Omega_a^0\boldsymbol{f}_0^{a,n}+\sum_{b\in\Lambda_a}\mathcal{D}_{ab}^{\boldsymbol{p},n}; \tag{59a}$$

$$\Omega_a^0\left[\frac{\boldsymbol{F}_a^{n+1}-\boldsymbol{F}_a^n}{\Delta t}\right]=\sum_{b\in\Lambda_a}\frac{1}{\rho_0}\boldsymbol{p}_{ab}^{\text{Ave},n}\otimes\boldsymbol{C}_{ab}+\sum_{\gamma\in\Gamma_a^B}\frac{1}{\rho_0}\boldsymbol{p}_a^{\gamma,n}\otimes\boldsymbol{C}_\gamma; \tag{59b}$$

$$\Omega_a^0\left[\frac{\boldsymbol{H}_a^{n+1}-\boldsymbol{H}_a^n}{\Delta t}\right]=\boldsymbol{F}_a^n\times\left(\sum_{b\in\Lambda_a}\frac{1}{\rho_0}\boldsymbol{p}_{ab}^{\text{Ave},n}\otimes\boldsymbol{C}_{ab}+\sum_{\gamma\in\Gamma_a^B}\frac{1}{\rho_0}\boldsymbol{p}_a^{\gamma,n}\otimes\boldsymbol{C}_\gamma\right); \tag{59c}$$

$$\Omega_a^0\left[\frac{p_a^{\text{int}}-p_a^n}{\tilde{\kappa}\,\Delta t}\right]=\boldsymbol{H}_a^n:\left(\sum_{b\in\Lambda_a}\frac{1}{\rho_0}\boldsymbol{p}_{ab}^{\text{Ave},n}\otimes\boldsymbol{C}_{ab}+\sum_{\gamma\in\Gamma_a^B}\frac{1}{\rho_0}\boldsymbol{p}_a^{\gamma,n}\otimes\boldsymbol{C}_\gamma\right)+\sum_{b\in\Lambda_a}\mathcal{D}_{ab}^{J,n}. \tag{59d}$$

The corrector step of the discrete system $\{\boldsymbol{p},\boldsymbol{F},\boldsymbol{H},p\}$ becomes

$$\Omega_a^0\frac{\partial \boldsymbol{p}_a}{\partial \tau}=\frac{1}{2}\sum_{b\in\Lambda_a}\left[\left(p_b^{n+1}-p_b^n\right)\boldsymbol{H}_b^n\right]\boldsymbol{C}_{ab}-\Omega_a^0\frac{\left(\boldsymbol{p}_a^{n+1}-\boldsymbol{p}_a^{\text{int}}\right)}{\Delta t}; \tag{60a}$$

$$\frac{\Omega_a^0}{\gamma}\frac{\partial p_a}{\partial \tau}=\frac{\Omega_a^0}{\tilde{\kappa}}\frac{p_a^{\text{int}}-p_a^n}{\Delta t}-\frac{\Omega_a^0}{\kappa}\frac{\left(p_a^{n+1}-p_a^n\right)}{\Delta t}+\frac{1}{2}\boldsymbol{H}_a^n:\sum_{b\in\Lambda_a^b}\left(\frac{\boldsymbol{p}_b^{n+1}}{\rho_0}-\frac{\boldsymbol{p}_b^n}{\rho_0}\right)\otimes\boldsymbol{C}_{ab}. \tag{60b}$$

5.3. Iteration speed-up procedure

To accelerate the speed of convergence within the iterative process, we can incorporate an additional Laplacian dissipative operator to equation (60b), which results in

$$\frac{\Omega_a^0}{\gamma}\frac{dp_a}{d\tau}=\frac{\Omega_a^0}{\tilde{\kappa}}\frac{p_a^{\text{int}}-p_a^n}{\Delta t}-\frac{\Omega_a^0}{\kappa}\frac{\left(p_a^{n+1}-p_a^n\right)}{\Delta t}+\frac{1}{2}\boldsymbol{H}_a^n:\sum_{b\in\Lambda_a^b}\left(\frac{\boldsymbol{p}_b^{n+1}}{\rho_0}-\frac{\boldsymbol{p}_b^n}{\rho_0}\right)\otimes\boldsymbol{C}_{ab}+\sum_{b\in\Lambda_a}\mathcal{D}_{ab}^{\text{PSE}}. \tag{61}$$

Referring to [54], the discrete Laplacian viscosity operator used in this work is defined as

$$\mathcal{D}_{ab}^{\mathrm{PSE}} := \alpha \frac{c_s^2 \Delta t}{\mu} \left[\frac{p_b - p_a}{\|\boldsymbol{X}_b - \boldsymbol{X}_a\|} \boldsymbol{N}_{ab} \right] \cdot \boldsymbol{C}_{ab}, \tag{62}$$

where α is a dimensionless user-defined parameter in the range of $[0, 1]$. Above dissipative operator automatically ensures fulfilment of the global conservation requirement, that is $\sum_a \Omega_a^0 \mathcal{D}_{ab}^{\mathrm{PSE}} = 0$.

Notice here that the only purpose of adding viscosity operator $\mathcal{D}_{ab}^{\mathrm{PSE}}$ to (61) is to accelerate the speed of convergence within the pseudo time integration process when iteratively solving the implicit system for pressure correction (60a), (61). This is in clear contrast to the upwinding stabilisation terms $\{\boldsymbol{\mathcal{D}}_{ab}^{\boldsymbol{p}}, \mathcal{D}_{ab}^{J}\}$ introduced in the predictor step (59), crucial to ensure the robustness (overall stability) of the algorithm.

6. Numerical examples

An ample spectrum of numerical examples is presented in order to examine the performance of the proposed methodologies in compressible, nearly incompressible and truly incompressible scenarios. Specifically, three different types of proposed methodologies are analysed, namely Upwind Total Lagrangian Formulation (Upwind-TLF, refer to (40a) and (43a)–(43c)), Upwind Updated Lagrangian Formulation (Upwind-ULF, refer to (48a)–(48d)) and Upwind Pseudo Updated Lagrangian Formulation (Upwind-PULF, refer to (48a)–(48d) but $\{\boldsymbol{c}_{ab}, \boldsymbol{c}_{\gamma}\}$ are replaced with $\{\tilde{\boldsymbol{c}}_{ab}, \tilde{\boldsymbol{c}}_{\gamma}\}$). For verification purposes, some of the results are benchmarked against other in-house mixed-based numerical schemes, namely Finite Element Method [48–51], Finite Volume Method [43–46] and mesh-free Smooth Particle Hydrodynamics [52,53].

6.1. Low dispersion cube

A cube of unit side length has symmetric boundary conditions (i.e. restricted to tangential displacement) at the faces $X = 0$, $Y = 0$ and $Z = 0$ and skew-symmetric boundary conditions (i.e. restricted to normal displacement) at the faces $X = 1$, $Y = 1$ and $Z = 1$. This example has been thoroughly explored in previous publications [39,44–46,49,55,56], with the final aim to show the optimal convergence behaviour of the proposed framework. In the case of small deformations, the problem has an analytical (or closed-form) solution for the displacement field described as

$$\boldsymbol{u}(\boldsymbol{X}, t) = U_0 \cos\left(\frac{\sqrt{3}}{2} c_d \pi t\right) \begin{bmatrix} A \sin\left(\frac{\pi X_1}{2}\right) \cos\left(\frac{\pi X_2}{2}\right) \cos\left(\frac{\pi X_3}{2}\right) \\ B \cos\left(\frac{\pi X_1}{2}\right) \sin\left(\frac{\pi X_2}{2}\right) \cos\left(\frac{\pi X_3}{2}\right) \\ C \cos\left(\frac{\pi X_1}{2}\right) \cos\left(\frac{\pi X_2}{2}\right) \sin\left(\frac{\pi X_3}{2}\right) \end{bmatrix}; \qquad c_d = \sqrt{\frac{\lambda + 2\mu}{\rho_0}}. \tag{63}$$

When the value of $U_0 < 0.001$ m, this example is considered to be linear and the exact solution provided in (63) holds. In this case, the problem is initialised with a given fibre map $\boldsymbol{F}(\boldsymbol{X}, t = 0) := \boldsymbol{F}^0(\boldsymbol{X}) = \boldsymbol{I} + \nabla_0 \boldsymbol{u}|_{t=0}$ by taking the material gradient of (63) at time $t = 0$. Subsequently, the initial conditions for the area and volume maps are $\boldsymbol{H}(\boldsymbol{X}, t = 0) := \boldsymbol{H}^0(\boldsymbol{X}) = \frac{1}{2}\left(\boldsymbol{F}^0 \times \boldsymbol{F}^0\right)$ and $J(\boldsymbol{X}, t = 0) := J^0(\boldsymbol{X}) = \frac{1}{6}\boldsymbol{F}^0 : \left(\boldsymbol{F}^0 \times \boldsymbol{F}^0\right)$, respectively. A linear elastic model is chosen where the material properties are Poisson's ratio of $\nu = (1 - \mu/\kappa)/2 = 0.45$, Young's modulus $E = 17$ MPa and density $\rho_0 = 1100$ kg/m^3. The solution parameters are set as $U_0 = 5 \times 10^{-4}$ m and the value of $A = B = C = 1$ [44] ensures the existence of a non-zero pressure field.

Tables 1 and 2 show the L_1 and L_2 global convergence analysis of the linear momentum $\boldsymbol{p}$ and the first Piola Kirchhoff stress tensor $\boldsymbol{P}$ simulated using the $\{\boldsymbol{p}, \boldsymbol{F}, \boldsymbol{H}, J\}$ Upwind-TLF and a $\{\boldsymbol{p}, \boldsymbol{F}, \boldsymbol{H}, J\}$ Jameson-Schmidt-Turkel Total Lagrangian Formulation (JST-TLF) [46] is shown for completeness, as compared to the analytical solution described in (63). Their corresponding graphical representations are depicted in Figs. 4 and 5. As expected, both methodologies show very similar

Table 1
Low dispersion cube: Numerical values for the relative error of the p_1 component of linear momentum as compared to the exact solution, measured with L^1 and L^2 norms. Comparison between the $\{\boldsymbol{p}, \boldsymbol{F}, \boldsymbol{H}, J\}$ Upwind-TLF and $\{\boldsymbol{p}, \boldsymbol{F}, \boldsymbol{H}, J\}$ JST-TLF. Convergence rate calculated using the results of the two finest meshes.

h	$\{\boldsymbol{p}, \boldsymbol{F}, \boldsymbol{H}, J\}$ JST-TLF		$\{\boldsymbol{p}, \boldsymbol{F}, \boldsymbol{H}, J\}$ Upwind-TLF	
	L^1 norm	L^2 norm	L^1 norm	L^2 norm
1/3	1.886×10^{-1}	2.044×10^{-1}	1.742×10^{-1}	1.948×10^{-1}
1/6	6.158×10^{-2}	6.732×10^{-2}	4.535×10^{-2}	5.116×10^{-2}
1/12	1.614×10^{-2}	1.988×10^{-2}	1.155×10^{-2}	1.265×10^{-2}
1/24	4.262×10^{-3}	5.663×10^{-3}	3.030×10^{-3}	3.197×10^{-3}
1/48	1.131×10^{-3}	1.524×10^{-3}	7.762×10^{-4}	7.995×10^{-4}
conv. rate	1.9134	1.8933	1.9652	1.9996

Table 2
Low dispersion cube: Numerical values for the relative error of the P_{11} component of the stress as compared to the exact solution, measured with L^1 and L^2 norms. Comparison between the $\{\boldsymbol{p}, \boldsymbol{F}, \boldsymbol{H}, J\}$ Upwind-TLF and $\{\boldsymbol{p}, \boldsymbol{F}, \boldsymbol{H}, J\}$ JST-TLF. Convergence rate calculated using the results of the two finest meshes.

h	$\{\boldsymbol{p}, \boldsymbol{F}, \boldsymbol{H}, J\}$ JST-TLF		$\{\boldsymbol{p}, \boldsymbol{F}, \boldsymbol{H}, J\}$ Upwind-TLF	
	L^1 norm	L^2 norm	L^1 norm	L^2 norm
1/3	1.634×10^{-1}	7.326×10^{-2}	1.621×10^{-1}	7.379×10^{-2}
1/6	6.684×10^{-2}	3.743×10^{-2}	6.108×10^{-2}	3.435×10^{-2}
1/12	2.017×10^{-2}	1.271×10^{-2}	1.692×10^{-2}	1.068×10^{-2}
1/24	5.337×10^{-3}	3.538×10^{-3}	4.267×10^{-3}	2.837×10^{-3}
1/48	1.396×10^{-3}	1.009×10^{-3}	1.079×10^{-3}	8.073×10^{-4}
conv. rate	1.9348	1.8093	1.9829	1.8136

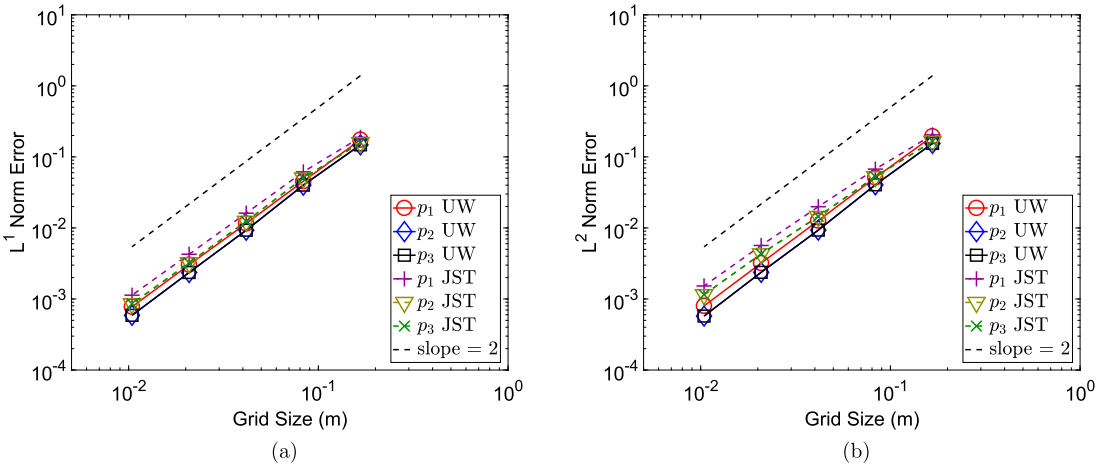

Fig. 4. Low dispersion cube. Convergence of the (a) L^1 norm and (b) L^2 norm for the components of linear momentum at time $t = 0.002$ s. Results are obtained using $\{\boldsymbol{p}, \boldsymbol{F}, \boldsymbol{H}, J\}$ Upwind-TLF and $\{\boldsymbol{p}, \boldsymbol{F}, \boldsymbol{H}, J\}$ JST-TLF with parameters $A = B = C = 1$ and $U_0 = 5 \times 10^{-4}$ m. A linear elastic material is used with density $\rho_0 = 1100$ kg/m^3, Young's modulus $E = 17$ MPa and Poisson's ratio $\nu = 0.45$ and $\alpha_{CFL} = 0.3$. JST stabilising parameters used: $k_{\boldsymbol{p}}^{(4)} = 1/256$, $k_J^{(4)} = 1/8192$.

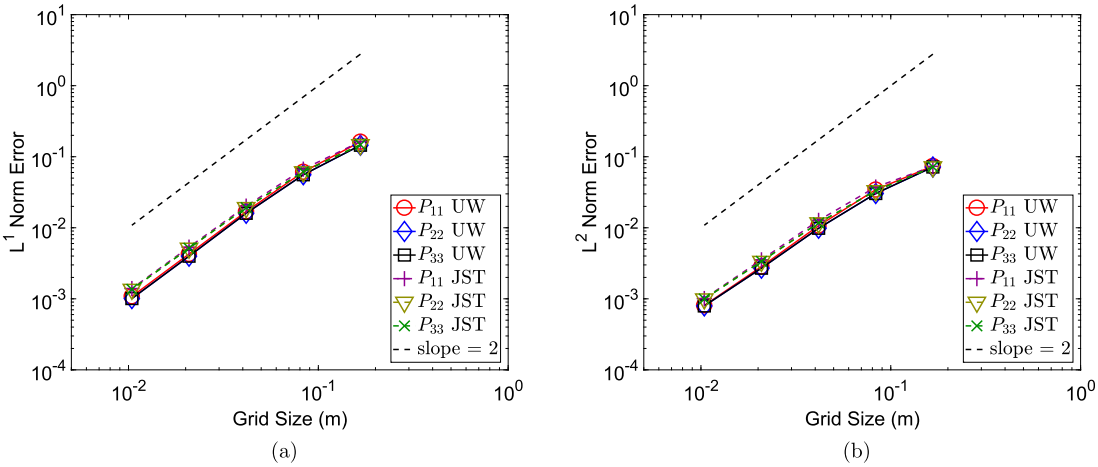

Fig. 5. Low dispersion cube. Convergence of the (a) L^1 norm and (b) L^2 norm for the diagonal components of the first Piola–Kirchhoff stress tensor $\boldsymbol{P}$ at time $t = 0.002$ s. Results are obtained using $\{\boldsymbol{p}, \boldsymbol{F}, \boldsymbol{H}, J\}$ Upwind-TLF and $\{\boldsymbol{p}, \boldsymbol{F}, \boldsymbol{H}, J\}$ JST-TLF with parameters $A = B = C = 1$ and $U_0 = 5 \times 10^{-4}$ m. A linear elastic material is used with density $\rho_0 = 1100$ kg/m^3, Young's modulus $E = 17$ MPa and Poisson's ratio $\nu = 0.45$ and $\alpha_{CFL} = 0.3$. JST stabilising parameters used: $k_{\boldsymbol{p}}^{(4)} = 1/256$, $k_J^{(4)} = 1/8192$.

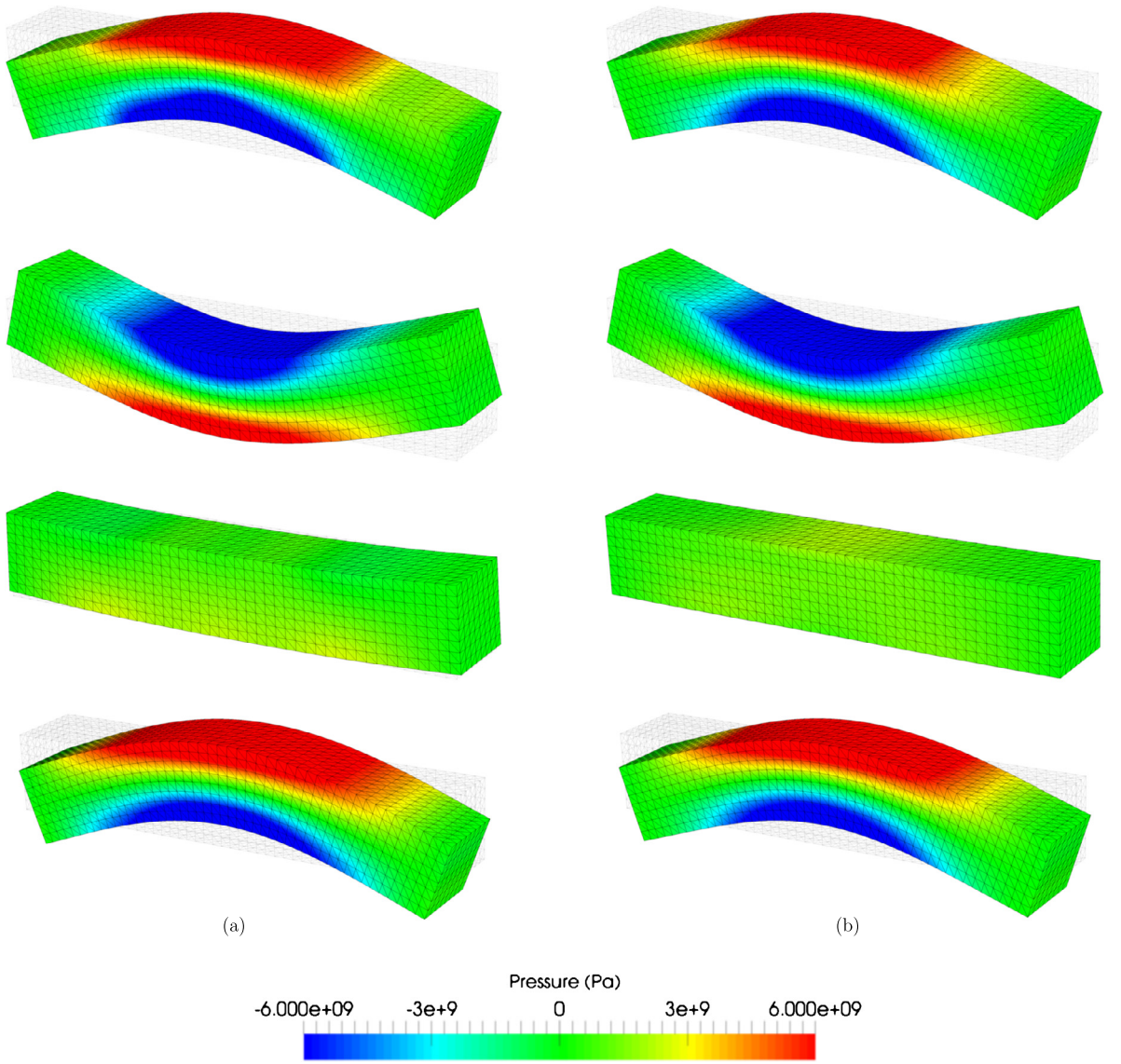

Fig. 6. Beryllium plate. Deformation shapes plotted with pressure at different time instants (from top to bottom): $t = 1 \times 10^{-5}$ s; 2×10^{-5} s; 3×10^{-5} s and 4×10^{-5} s. Results are obtained using the (a) $\{\boldsymbol{p}, \boldsymbol{F}\}$ Upwind-TLF scheme with Poisson's ratio $\nu = 0.0539$ and (b) $\{\boldsymbol{p}, \boldsymbol{F}, J\}$ Upwind-TLF scheme with Poisson's ratio $\nu = 0.4995$. A neo-Hookean material is used with density $\rho_0 = 1845$ kg/m^3, Young's modulus $E = 318.27$ GPa and $\alpha_{CFL} = 0.3$. Discretisation of $8 \times 8 \times 48 \times 6$ linear tetrahedral elements.

convergence pattern, achieving equal second order convergence for both linear momentum and the components of the stress tensor. Remarkably, the Upwind-TLF method shows better accuracy than the JST-TLF algorithm, with the same slope but with a lower translation error (see Figs. 4 and 5). This is due to the fact that JST-TLF method requires careful selection of a number of artificial stabilisation parameters for properly controlling the amount of numerical dissipation introduced by the algorithm.

6.2. Elastic vibration of a Beryllium plate

Following References [38,46,69], the main purpose of this benchmark problem is to assess the accuracy of the proposed Upwind-TLF method in the elastic regime. A Beryllium plate, of dimensions $[-0.5, -3, -0.5]$ m $\times$ $[0.5, 3, 0.5]$ m, is simulated using a neo-Hookean model with material properties given as density $\rho_0 = 1845$ kg/m^3, Young's modulus $E = 318.27$ GPa and Poisson's ratio $\nu = 0.0539$. The plate, with no supports or constraints, is oscillating freely at time $t = 0$ via the imposition of a specific form of initial velocity field that purely excites its first flexural mode [45] as

$$\boldsymbol{v}_0 = [0, 0, v_z]^T; \quad v_z = A\omega\left[g_1\left(\sinh(B\mathrm{Y}) + \sin(B\mathrm{Y})\right) - g_2\left(\cosh(B\mathrm{Y}) + \cos(B\mathrm{Y})\right)\right]. \tag{64}$$

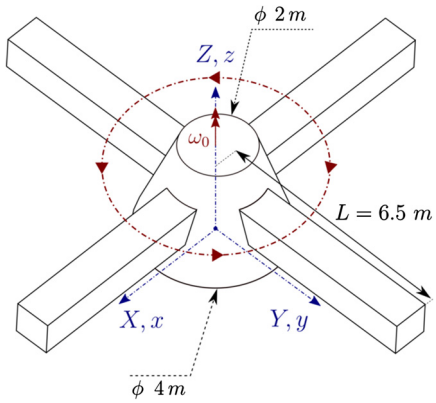

Fig. 7. Satellite-like structure configuration. The structure is free everywhere and initialised with a constant angular velocity $\boldsymbol{\omega}_0 = [0, 0, 1]^T$ rad/s.

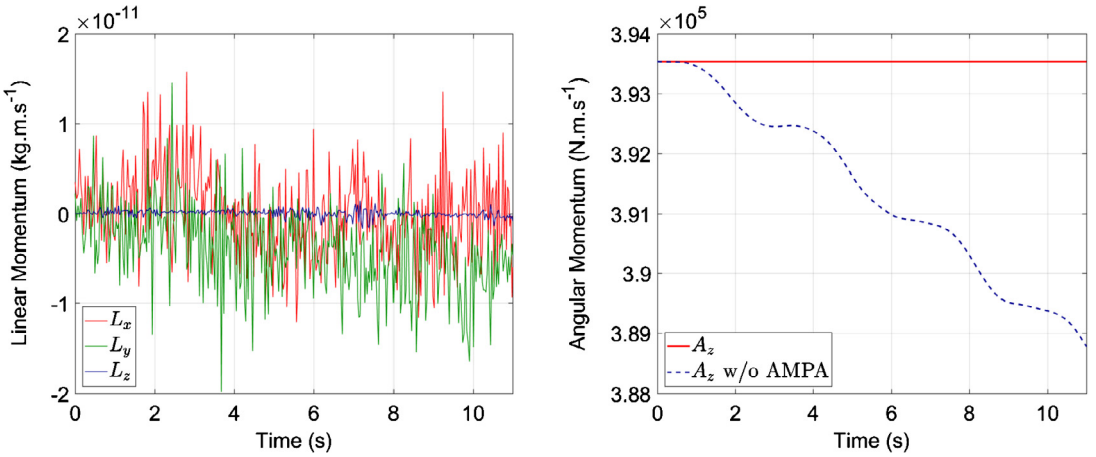

(a) Linear momentum (b) Angular momentum

Fig. 8. Satellite-like structure. Time evolution of (a) linear momentum and (b) z-component of angular momentum, with and without the consideration of the discrete angular momentum projection algorithm (AMPA). Results are obtained using the $\{\boldsymbol{p}, \boldsymbol{F}\}$ Upwind–TLF scheme with an initial angular velocity $\boldsymbol{\omega}_0 = [0, 0, 1]^T$ rad/s. A neo-Hookean material is used with density $\rho_0 = 1000$ kg/m^3, Young's modulus $E = 50.05$ kPa, Poisson's ratio $\nu = 0.3$ and $\alpha_{CFL} = 0.3$. The domain is discretised using a linear tetrahedral mesh with 2496 nodes.

In this case, the parameters are set as $g_1 = 56.637$, $g_2 = 57.646$, $\omega = 2.3597$ s^{-1}, $A = 4.3369 \times 10^{-5}$ m, $B = 78.834$ m^{-1} and $\mathrm{Y} = Y + 0.03$.

For quantitative comparison purposes, a sequence of snapshots capturing the deformation of the plate is depicted in the first column of Fig. 6. Smooth pressure field is observed. Our results are in very good agreement with those results published in [38], with the latter being obtained using an excessively fine mesh. For completeness, Fig. 9a monitors the time evolution of the vertical component of the displacement at the origin $\boldsymbol{X} = [0, 0, 0]^T$. It is clear that the solution converges with a progressive level of refinement. The time history of the P_{yY} component of the first Piola–Kirchhoff stress tensor $\boldsymbol{P}$ at point $\boldsymbol{X} = [0, 0, 0.5]^T$ is plotted in Fig. 9b. As can be seen, as the mesh is refined (although still coarse), the solution picks up a higher energy mode which is clearly shown by the higher oscillatory behaviour of the stress component displayed in the figure. This is not noticeable in Fig. 9a, due to the time integrated nature of the displacements. First order formulations (with not reconstruction) might not pick up this higher energy mode unless very refined meshes are employed (due the higher dissipative nature of these schemes).

Finally, we further assess the performance of the $\{\boldsymbol{p}, \boldsymbol{F}, J\}$ Upwind-TLF algorithm by using a large value of the Poisson's ratio $\nu = 0.4995$ (refer to the second column of Fig. 6). As can be observed, the proposed method can be efficiently used for the simulation of this problem without experiencing locking difficulties.

6.3. Satellite-like structure

A flexible satellite-like structure [70] is studied in this section. The main objective of this problem is to examine the capability of the proposed methodologies in preserving the linear and angular momenta of a system. The structure, as displayed in Fig. 7, consists of a central truncated cone of base radius 4 m, of top radius 2 m and of height 3 m, along

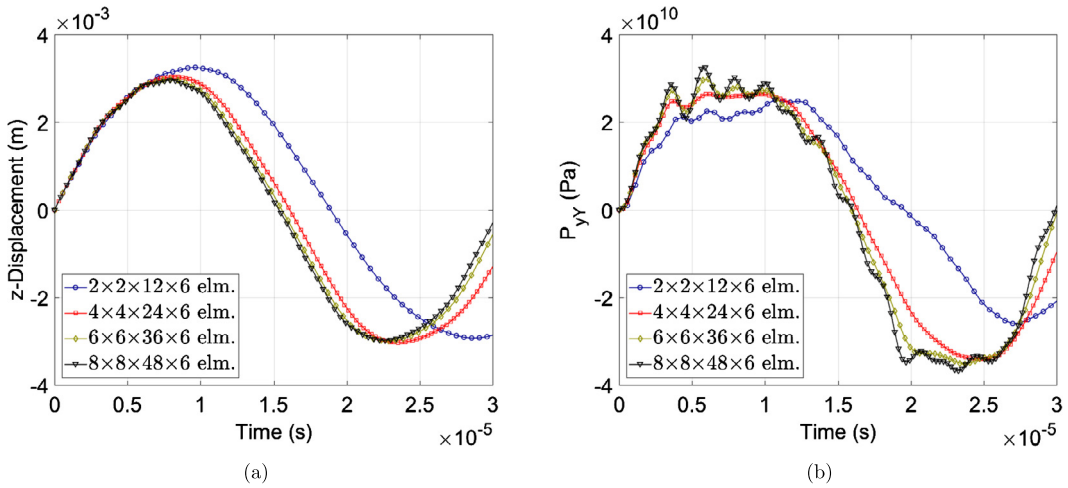

Fig. 9. Beryllium plate. (a) Time history of the z-displacement of the point $\boldsymbol{X} = [0, 0, 0]^T$ and (b) P_{yY} component of first Piola–Kirchhoff stress tensor $\boldsymbol{P}$ at point $\boldsymbol{X} = [0, 0, 0.5]^T$. Results are obtained using the $\{\boldsymbol{p}, \boldsymbol{F}\}$ Upwind-TLF scheme with different mesh sizes. A neo-Hookean material is used with density $\rho_0 = 1845$ kg/m^3, Young's modulus $E = 318.27$ GPa, Poisson's ratio $\nu = 0.0539$ and $\alpha_{CFL} = 0.3$.

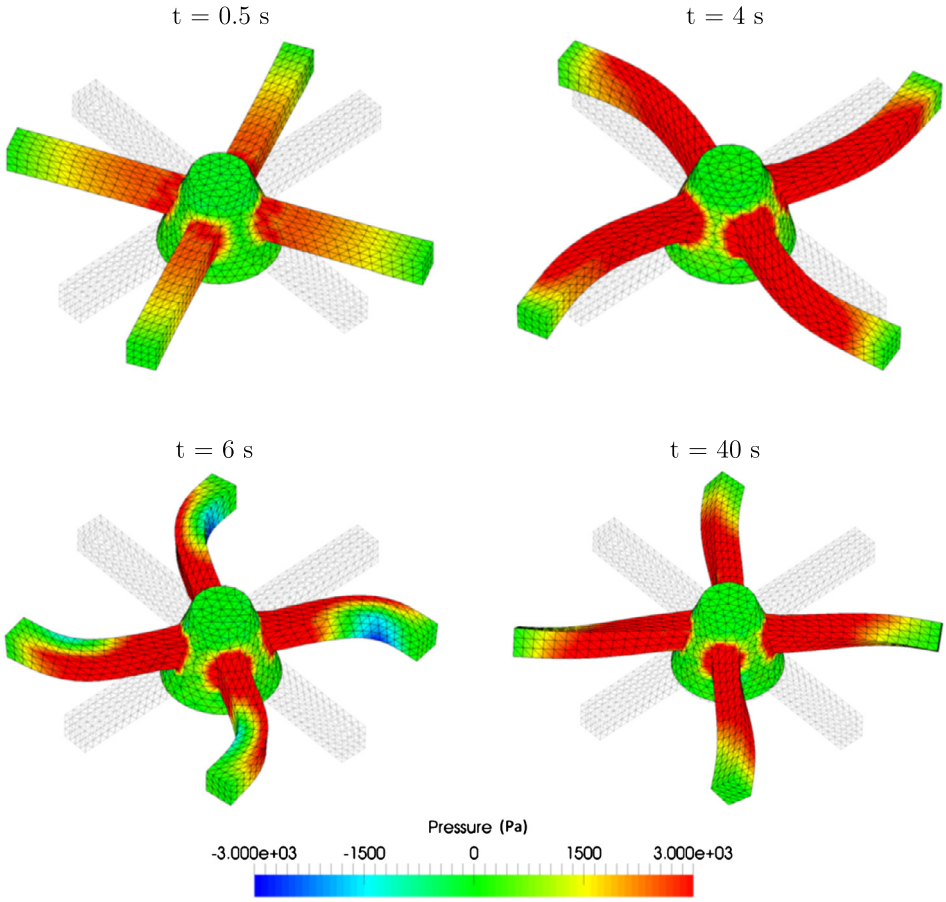

Fig. 10. Satellite-like structure. Time evolution of the deformation along with the pressure distribution. Results are obtained using the $\{\boldsymbol{p}, \boldsymbol{F}\}$ Upwind–TLF scheme with an initial angular velocity $\boldsymbol{\omega}_0 = [0, 0, 1]^T$ rad/s. A neo-Hookean material is used with density $\rho_0 = 1000$ kg/m^3, Young's modulus $E = 50.05$ kPa, Poisson's ratio $\nu = 0.3$ and $\alpha_{CFL} = 0.3$. The domain is discretised using linear tetrahedral mesh with 2496 nodes.

with four attached arms of unit cross-section that extend 6.5 m from the centre of the structure. The satellite is released without any initial deformation but with an initial angular velocity of $\Omega = 1$ rad/s about the centre of mass. The velocity field relative to its centre of mass $\boldsymbol{X}_{\text{cm}}$ is given as

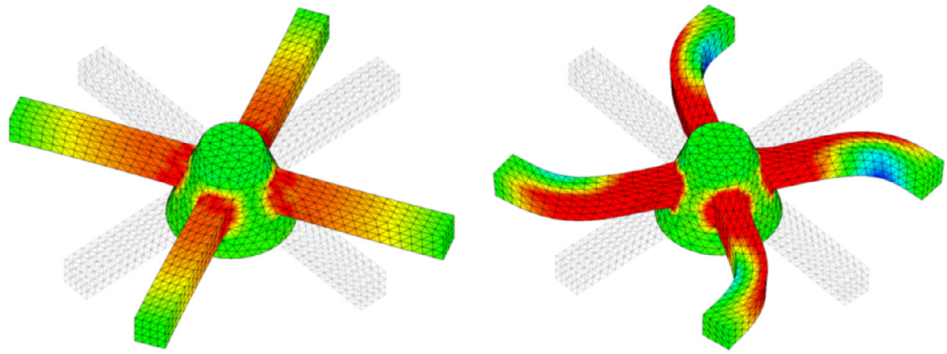

(a) $\{\boldsymbol{p},\boldsymbol{F}\}$Upwind–TLF.

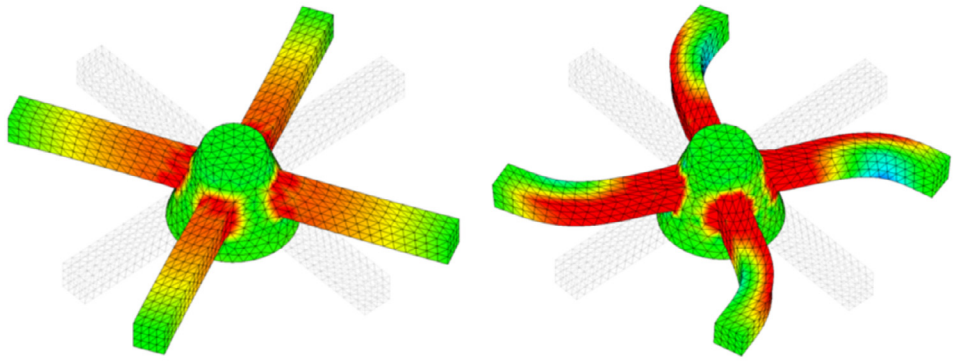

(b) $\{\boldsymbol{p},\boldsymbol{F}\}$ JST–TLF.

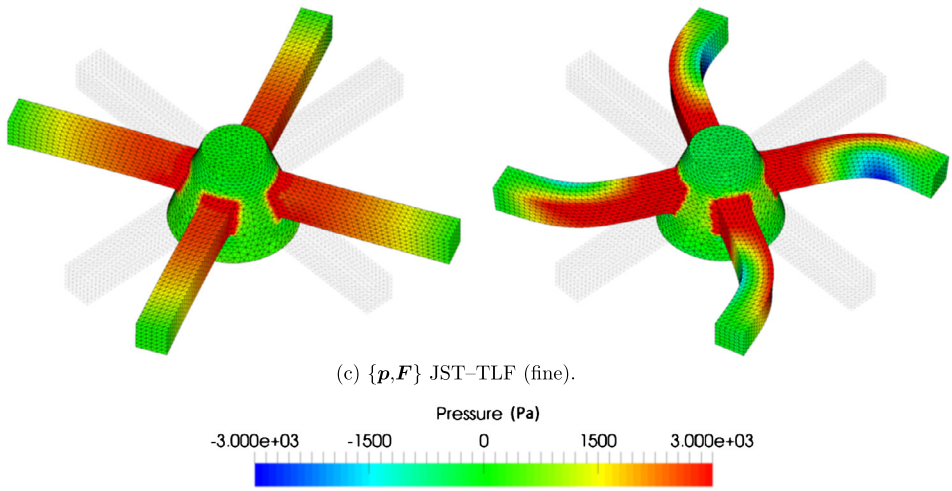

(c) $\{\boldsymbol{p},\boldsymbol{F}\}$ JST–TLF (fine).

Fig. 11. Satellite-like structure. Comparison of deformed shapes plotted with pressure distribution at times $t = 0.5$ s and $t = 6$ s using different schemes: (a) $\{\boldsymbol{p}, \boldsymbol{F}\}$ Upwind–TLF; (b) $\{\boldsymbol{p}, \boldsymbol{F}\}$ JST–TLF and (c) $\{\boldsymbol{p}, \boldsymbol{F}\}$ JST–TLF (fine). Results are obtained with an initial angular velocity $\boldsymbol{\omega}_0 = [0, 0, 1]^T$ rad/s. A neo-Hookean material is used with density $\rho_0 = 1000$ kg/m^3, Young's modulus $E = 50.05$ kPa, Poisson's ratio $\nu = 0.3$, $k_{\boldsymbol{p}}^{(4)} = 1/256$ and $\alpha_{CFL} = 0.3$.

$$\boldsymbol{v}^0(\boldsymbol{X}) = \boldsymbol{\omega} \times (\boldsymbol{X} - \boldsymbol{X}_{\text{cm}})\,; \qquad \boldsymbol{\omega} = (0, 0, \Omega)^T\,; \qquad \boldsymbol{X} = (X, Y, 0)\,. \tag{65}$$

In this particular case, a neo-Hookean model is chosen and its material properties are given as density $\rho_0 = 1000$ kg/m^3, Young's modulus $E = 50.05$ kPa and Poisson's ratio $\nu = 0.3$.

Fig. 10 shows the time evolution of the pressure field during the deformation process, simulated using the $\{\boldsymbol{p}, \boldsymbol{F}, \boldsymbol{H}, J\}$ Upwind-TLF method. With respect to the accuracy of the methodologies used, it is important to notice that, for the exact same number of degrees of freedom, the Riemann based upwind stabilisation employed in Upwind-TLF gives a higher spatial resolution of pressure field, as compared with the $\{\boldsymbol{p}, \boldsymbol{F}, \boldsymbol{H}, J\}$ JST-TLF counterpart (see Figs. 11a and 11b). Specifically, compressive stresses at the bending region of each arm at time $t = 6$ s are captured accurately when employing a Upwind-TLF. In the case of the JST-TLF, it is essential to employ a sufficiently fine mesh in order to obtain a similar pressure

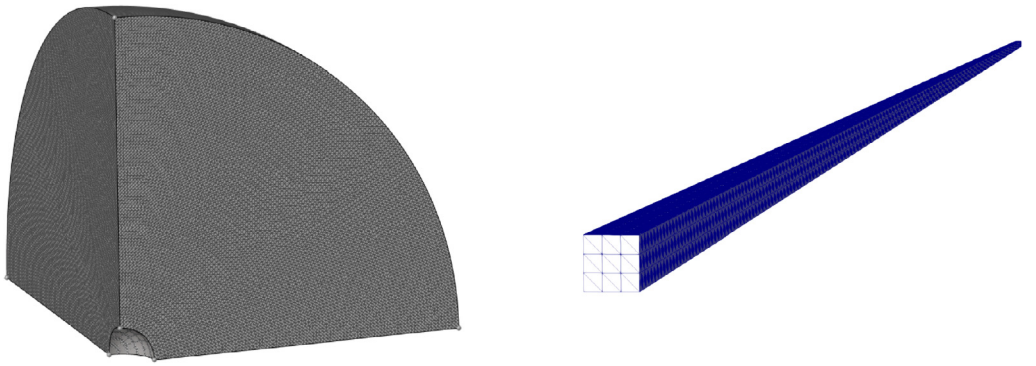

(a) Blake (b) Needle of 1^0 aperature angle

Fig. 12. Blake problem: (a) mesh of one-eighth of a shell and (b) mesh of a needle.

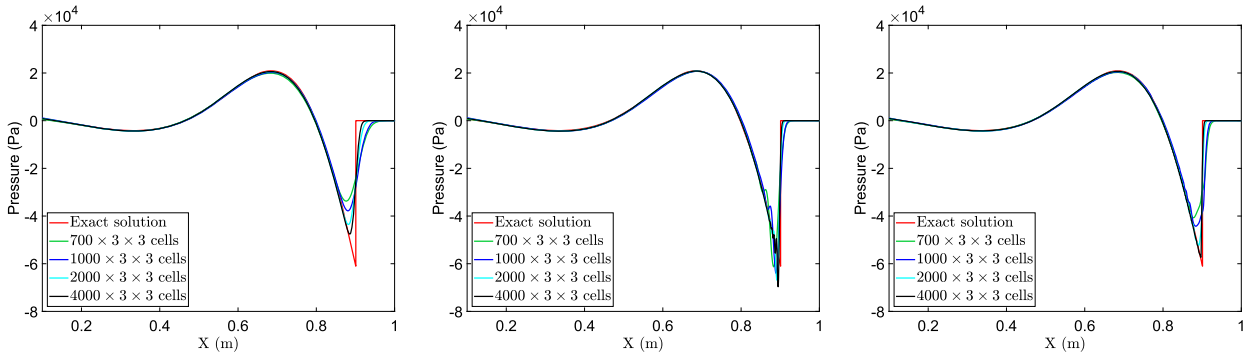

(a) First order (b) Second order (c) Barth Jespersen limiter

Fig. 13. Blake problem. The spatial distribution of radial pressure at time $t = 1.6 \times 10^{-4}$ s simulated using (a) piecewise constant reconstruction, (b) piecewise linear reconstruction and (c) piecewise linear reconstruction with the Barth and Jespersen limiter. Results are obtained using the $\{\boldsymbol{p}, \boldsymbol{F}, \boldsymbol{H}, J\}$ Upwind–TLF scheme with a boundary traction vector $\boldsymbol{t}_B = -p\boldsymbol{n}$ (with $p = 1 \times 10^6$ Pa) constantly applied to the inner face. A neo-Hookean material is used with density $\rho_0 = 3000$ kg/m^3, Young's modulus $E = 62.5$ GPa, Poisson's ratio $\nu = 0.25$ and $\alpha_{CFL} = 0.3$. The domain is discretised using a linear tetrahedral mesh.

representation, which in this case is almost 5 times greater than the number of nodes used in Upwind-TLF. This can be demonstrated by comparing Figs. 11c and 11b. Fig. 8 demonstrates the ability of the proposed algorithm in preserving both the angular and linear momenta of the system. Without activation of the angular momentum projection procedure, a significant reduction in total angular momentum can be clearly observed.

6.4. Blake problem

In this section, we present the Blake problem [38], of interest to the scientific community. The domain considered is a shell of inner radius $r_i = 0.1$ m and outer radius $r_o = 1$ m (see Fig. 12a). A constant in time boundary traction vector $\boldsymbol{t}_B = -p\boldsymbol{n}$ (with $p = 1 \times 10^6$ Pa) is applied to the inner surface of the shell, whereas the remaining surfaces are treated as traction free boundary conditions such that $\boldsymbol{t}_B = \boldsymbol{0}$. As reported in [38], for computational efficiency, the shell domain can be simplified to a needle of 1^0 aperture angle, as shown in Fig. 12b. In this case, all the boundary faces introduced by this geometrical simplification are subjected to symmetry boundary conditions (also known as roller support). The problem is simulated using the $\{\boldsymbol{p}, \boldsymbol{F}, \boldsymbol{H}, J\}$ Upwind-TLF scheme with a neo-Hookean material. The material properties are described as density $\rho_0 = 3000$ kg/m^3, Young's modulus $E = 62.5$ GPa and Poisson's ratio $\nu = 0.25$. Fig. 13 shows the spatial distribution of radial pressure at time $t = 1.6 \times 10^{-4}$ s, as compared to the analytical solution. As it can be observed, the first order FVM shows excellent smooth results though with considerable numerical diffusion and then leads to a stable yet slightly inaccurate solution (see Fig. 13a). To enhance the accuracy, we introduce a piecewise linear reconstruction. The second order FVM, as seen in Fig. 13b, gives much better resolution but fails near discontinuities, where non-physical oscillations are generated. In order to control these spurious oscillations, the Barth and Jespersen limiter [46] is implemented. A great improvement is observed in Fig. 13c.

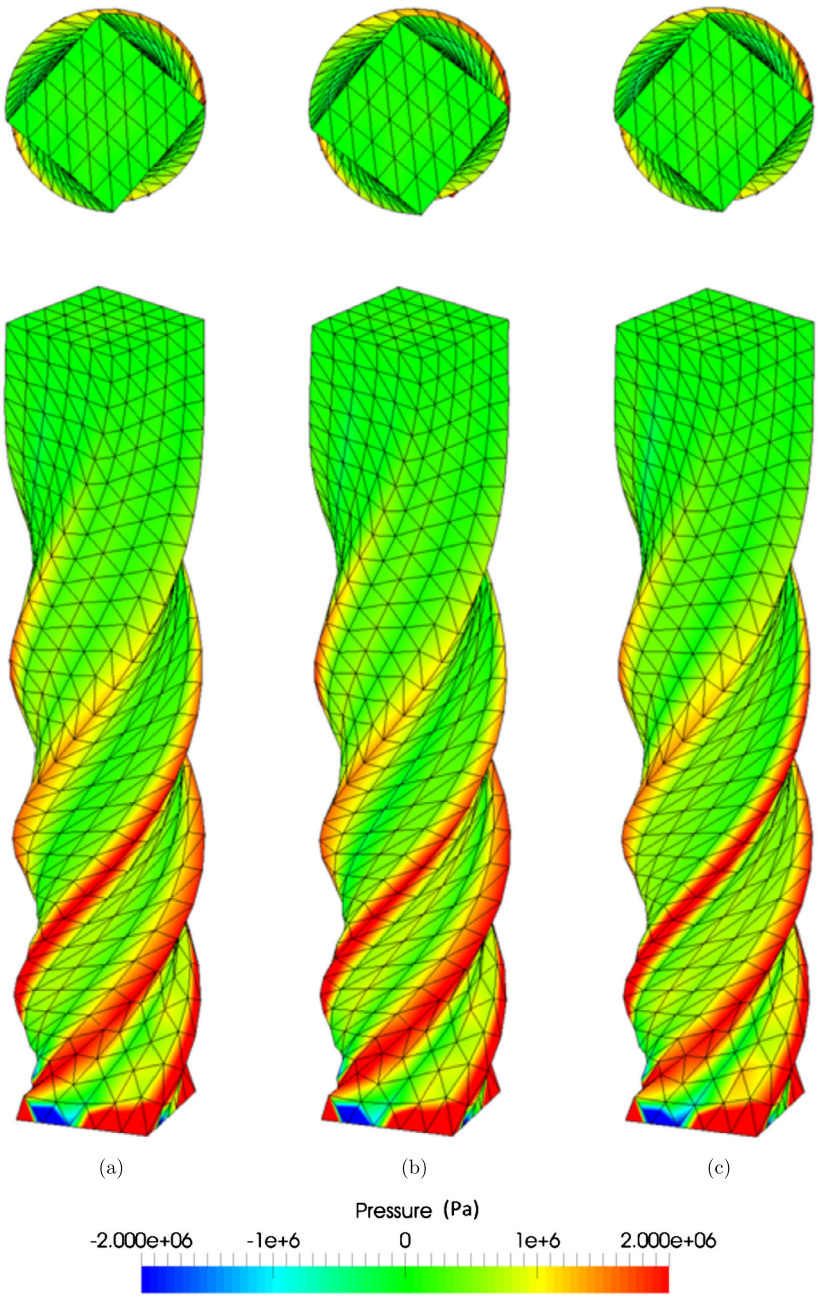

Fig. 14. Twisting column. Comparison of deformed shapes plotted with pressure distribution at time $t = 0.1$ s using different schemes: (a) $\{\boldsymbol{p}, \boldsymbol{F}\}$ Upwind-TLF; (b) $\{\boldsymbol{p}, \boldsymbol{F}\}$ Upwind-PULF and (c) $\{\boldsymbol{p}, \boldsymbol{F}\}$ Upwind-ULF. Results are obtained with an angular velocity field $\boldsymbol{\omega_0} = [0, 0, \Omega\ sin(\pi Z/2L)]^T$ where $\Omega = 105$ rad/s and $L = 6$ m. A neo-Hookean material is used with density $\rho_0 = 1100$ kg/m^3, Young's modulus $E = 17$ MPa, Poisson's ratio $\nu = 0.495$ and $\alpha_{CFL} = 0.3$.

6.5. Nearly incompressible twisting column

Aiming to illustrate the applicability and robustness of the proposed algorithm, a very challenging problem, previously explored in References [44,46,53,55], is presented. A unit squared cross section column is twisted along its height. The column is subject to an initial rotational velocity field expressed as

$$\boldsymbol{v}^0 = \boldsymbol{\omega}_0 \times \boldsymbol{X}; \quad \boldsymbol{\omega}_0 = \left[0, 0, \Omega\ \sin\left(\frac{\pi Z}{2L}\right)\right]^T, \tag{66}$$

where $\Omega = 105$ rad/s and $L = 6$ m is the length of the column. This example is modelled using a neo-Hookean model with parameters given as follows: Young's modulus $E = 17$ MPa, density $\rho_0 = 1100$ kg/m^3 and Poisson's ratio $\nu = 0.4995$.

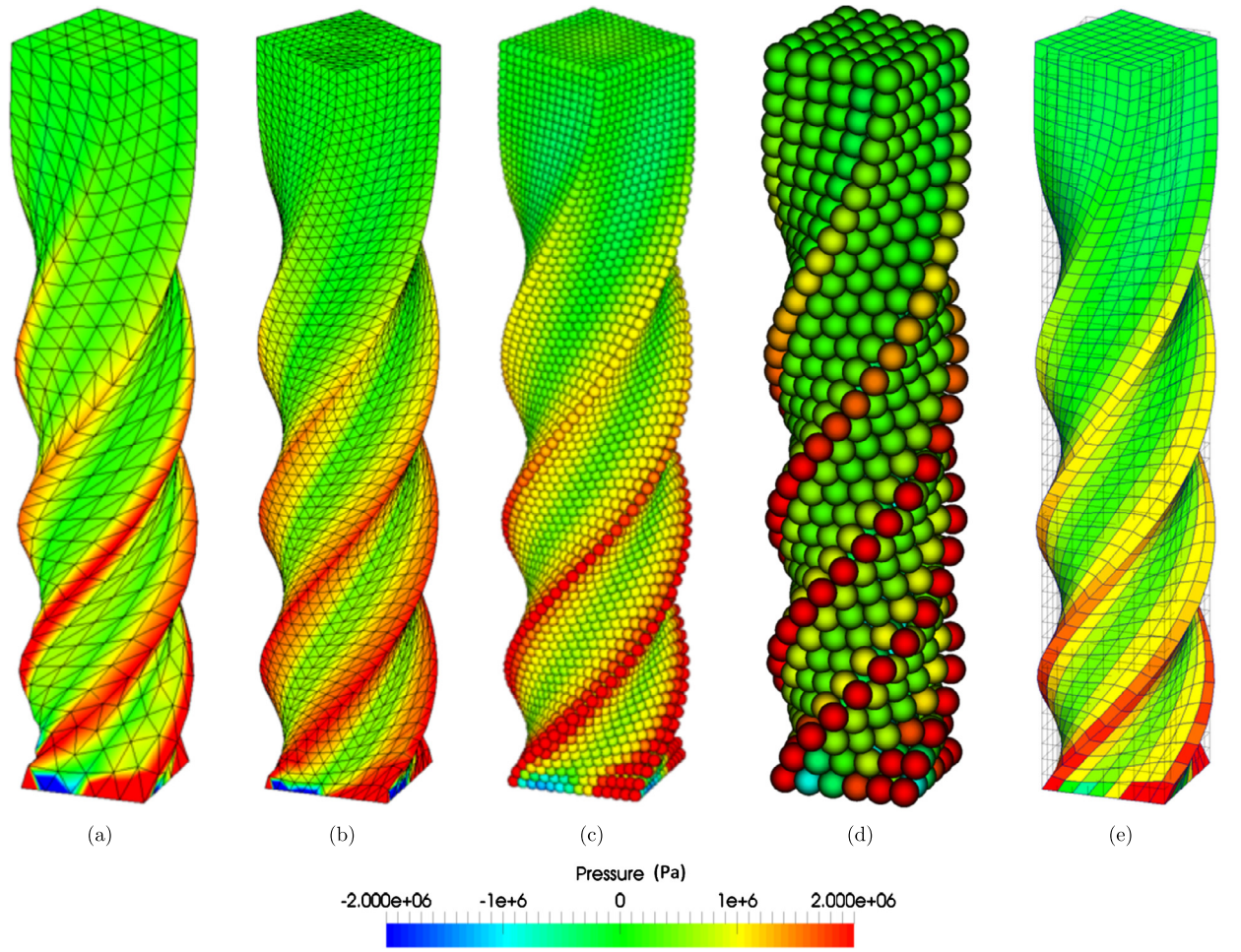

Fig. 15. Twisting column. Comparison of deformed shapes plotted with pressure distribution at time $t = 0.1$ s using different schemes: (a) TL–UW $\{\boldsymbol{p}, \boldsymbol{F}\}$; (b) TL–JST $\{\boldsymbol{p}, \boldsymbol{F}\}$; (c) Mixed-based $\{\boldsymbol{p}, \boldsymbol{F}, \boldsymbol{H}, J\}$ SUPG-SPH-H1 [53], (d) Upwind-SPH and (e) C-TOUCH. A neo-Hookean material is used with density $\rho_0 = 1100$ kg/m^3, Young's modulus $E = 17$ MPa and Poisson's ratio $\nu = 0.495$.

On another front, Fig. 14 shows the comparison between three different upwind schemes proposed in this paper, namely $\{\boldsymbol{p}, \boldsymbol{F}, J\}$ Upwind-TLF, $\{\boldsymbol{p}, \boldsymbol{F}, J\}$ Upwind-ULF and $\{\boldsymbol{p}, \boldsymbol{F}, J\}$ Upwind-PULF. Remarkably, the results obtained using the Upwind-TLF are in extremely good agreement with the Upwind-ULF counterpart. This shows that the selection of the continuum description of the system exclusively depends on the user's preference, regardless of accuracy of the method. More interestingly, Upwind-TLF is more computationally efficient as the integral evaluations are carried out at the initial undeformed configuration. Such evaluations only need to be computed once throughout the time integration process. As a viable alternative to the Upwind-ULF, an extremely competitive method, named Upwind-PULF, is also assessed. Practically identical results are obtained. As illustrated in the top view of the simulation of Fig. 14, no out-of-plane deformation can be observed.

For benchmarking purposes, Fig. 15 depicts a comparison of the new $\{\boldsymbol{p}, \boldsymbol{F}, J\}$ Upwind-TLF and $\{\boldsymbol{p}, \boldsymbol{F}, J\}$ JST-TLF methodologies against other in-house mixed-based methodologies, including Cell Centred FVM [43,44], Upwind-SPH [54] and Streamline Upwind Petrov Galerkin SPH [53] mesh-free methods. All of these schemes produce very similar results in terms of deformed shape and pressure field.

Finally, we can further examine the robustness of the algorithm by increasing the value of Poisson's ratio to the upper limit of $\nu = 0.5$. The main objective is to show the efficiency of the proposed artificial compressibility approach (see Section 5.1), especially in problems characterised by nearly or truly incompressible behaviours. Fig. 16 shows a qualitative comparison between the $\{\boldsymbol{p}, \boldsymbol{F}, p\}$ artificial compressibility algorithm and the explicit $\{\boldsymbol{p}, \boldsymbol{F}, p\}$ Upwind-TLF, with the interior pressure being displayed on the final deformed state. The artificial compressibility algorithm introduces a larger amount of numerical dissipation due to the use of the Pseudo viscosity term described in (62), which, as expected, is addressed with mesh refinement. A mesh refinement study is also carried out in Fig. 17. It is remarkable that the deformation pattern predicted using a small number of elements agrees extremely well with those results obtained using a finer discretisation.

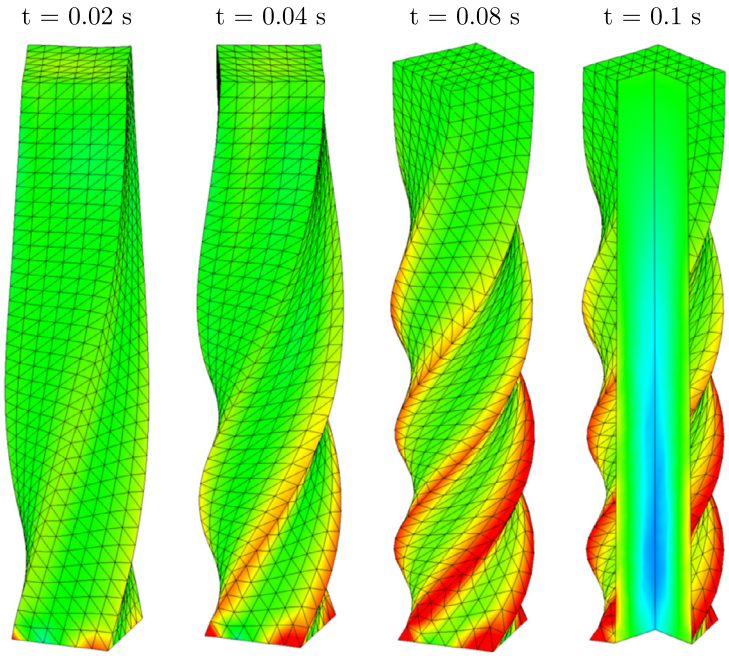

(a) Explicit $\{\boldsymbol{p},\boldsymbol{F},J\}$ Upwind-TLF

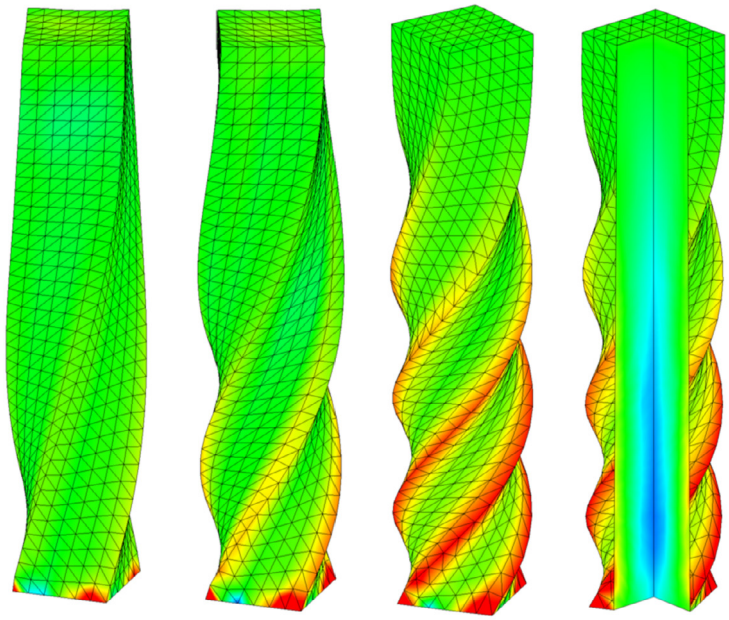

(b) Upwind-TLF Artificial compressibility

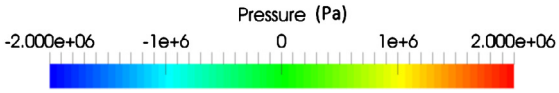

Fig. 16. Twisting column. Time evolution of the deformation along with the pressure distribution using: (a) Explicit $\{\boldsymbol{p}, \boldsymbol{F}, J\}$ Upwind-TLF and (b) Upwind-TLF Artificial compressibility. Results are obtained with an angular velocity field $\boldsymbol{\omega_0} = [0, 0, \Omega\ sin(\pi Z/2L)]^T$ where $\Omega = 105$ rad/s and $L = 6$ m. A neo-Hookean material is used with density $\rho_0 = 1100$ kg/m^3, Young's modulus $E = 17$ MPa, $\nu = 0.4995$, $\nu_{fic} = 0.495$, $L_p = 0.2$ and $\alpha_{CFL} = 0.3$.

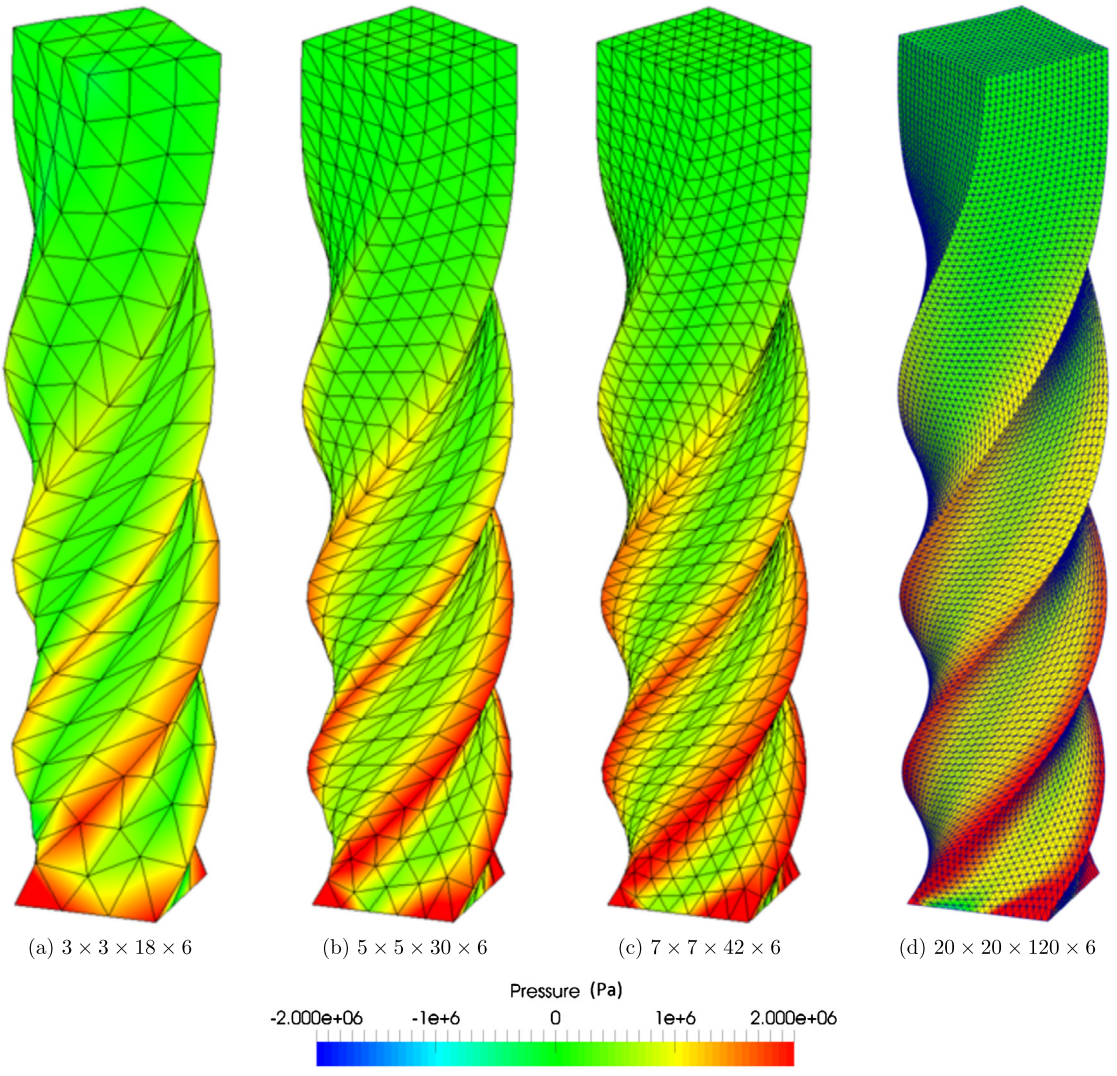

Fig. 17. Twisting column. Comparison of the deformation along with the pressure distribution at time $t = 0.1$ s for various mesh sizes: (a) $3 \times 3 \times 18 \times 6$; (b) $5 \times 5 \times 30 \times 6$; (c) $7 \times 7 \times 42 \times 6$ elements and (d) $20 \times 20 \times 120 \times 6$. Results are obtained using the Upwind–TLF artificial compressibility scheme with an angular velocity field $\boldsymbol{\omega_0} = [0, 0, \Omega\ sin(\pi Z/2L)]^T$ where $\Omega = 105$ rad/s and $L = 6$ m. A neo-Hookean material is used with density $\rho_0 = 1100$ kg/m^3, Young's modulus $E = 17$ MPa, $\nu = 0.5$, $\nu_{fic} = 0.495$, $L_p = 0.2$ and $\alpha_{CFL} = 0.3$.

6.6. Punch test

A rubber block is left free on its top face and constrained with roller supports (i.e. symmetric boundary conditions) on the rest of the boundaries. The $1 \times 1 \times 0.5$ m^3 block has a 3×3 array of vertical holes with a diameter of 0.2 m. The main aim of this example is to show the capability of the algorithm in suppressing spurious pressure oscillations in highly constrained problems. The deformation of the block is initiated with the following velocity field

$$\boldsymbol{v}^0 = -V[0, 0, (L/2 - |X|)(L/2 - |Y|)(Z/H)]^T, \tag{67}$$

where $V = -700$ m/s, L is the length of the block and H is its height.

A nearly incompressible neo-Hookean constitutive model is used where Young's modulus $E = 17$ MPa, density $\rho_0 = 1100$ kg/m^3 and Poisson's ratio $\nu = 0.495$. Fig. 18 depicts the deformation pattern of a rubber block solved using the $\{\boldsymbol{p}, \boldsymbol{F}, \boldsymbol{H}, J\}$ Upwind-TLF, displaying very smooth pressure contour. Fig. 19 compares the results against those obtained using the Upwind-SPH framework [53]. Both sets of results agree extremely well, without showing any signs of hourglassing.

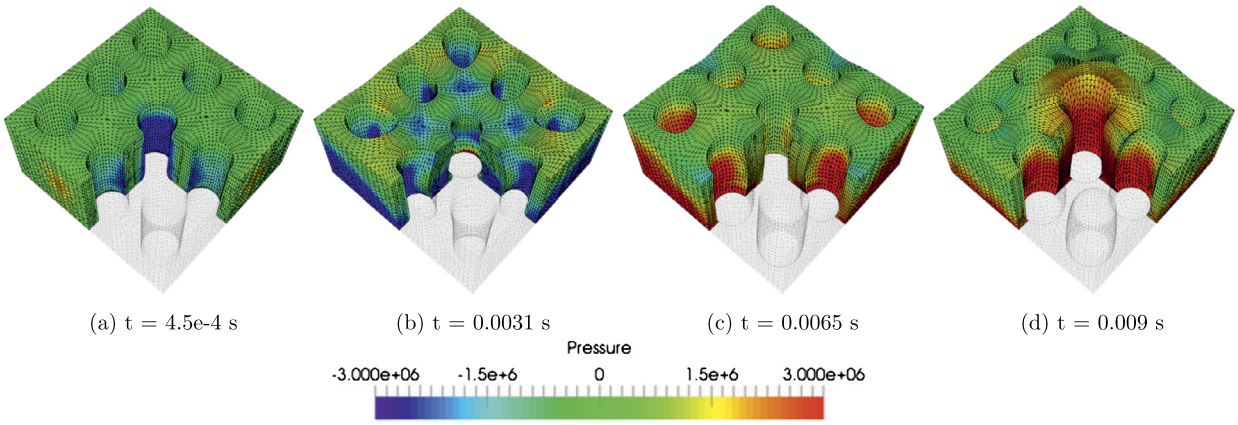

Fig. 18. Punch test. Time evolution of the deformation along with pressure distribution. Results are obtained using the $\{\boldsymbol{p}, \boldsymbol{F}, \boldsymbol{H}, J\}$ Upwind-TLF scheme. A neo-Hookean material is used with density $\rho_0 = 1100$ kg/m^3, Young's modulus $E = 17$ MPa, Poisson's ratio $\nu = 0.495$ and $\alpha_{CFL} = 0.3$.

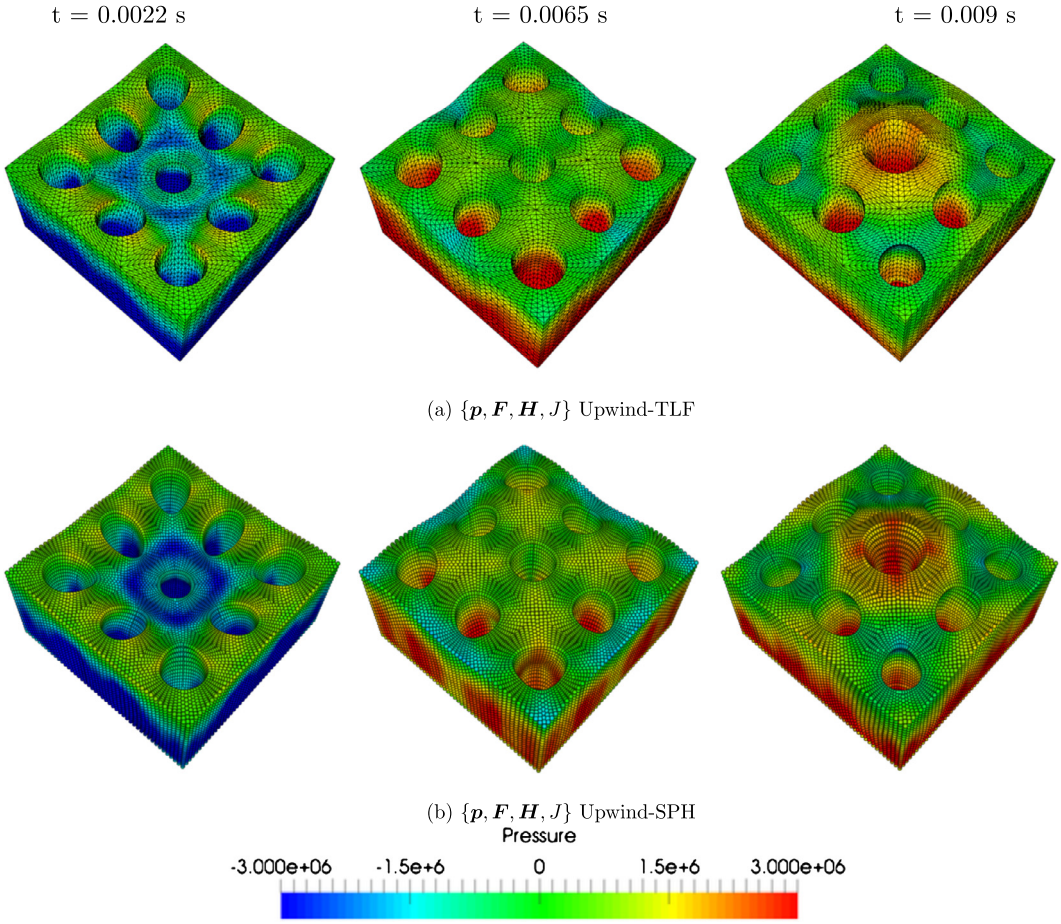

Fig. 19. Punch test. Comparison of deformed shapes plotted with pressure distribution at different snapshots in time using different schemes: (a) $\{\boldsymbol{p}, \boldsymbol{F}, \boldsymbol{H}, J\}$ Upwind-TLF and (b) Upwind-SPH. A neo-Hookean material is used with density $\rho_0 = 1100$ kg/m^3, Young's modulus $E = 17$ MPa, Poisson's ratio $\nu = 0.495$ and $\alpha_{CFL} = 0.3$.

6.7. Taylor impact

The impact of a copper bar against a rigid wall is investigated. The bar has an initial length of 0.0324 m and initial radius of 0.0032 m. The bar is dropped with a velocity of 227 m/s at time $t = 0$ s. A von Mises hyperelastic–plastic model with isotropic hardening is chosen to simulate the problem where the material properties being used are Young's modulus

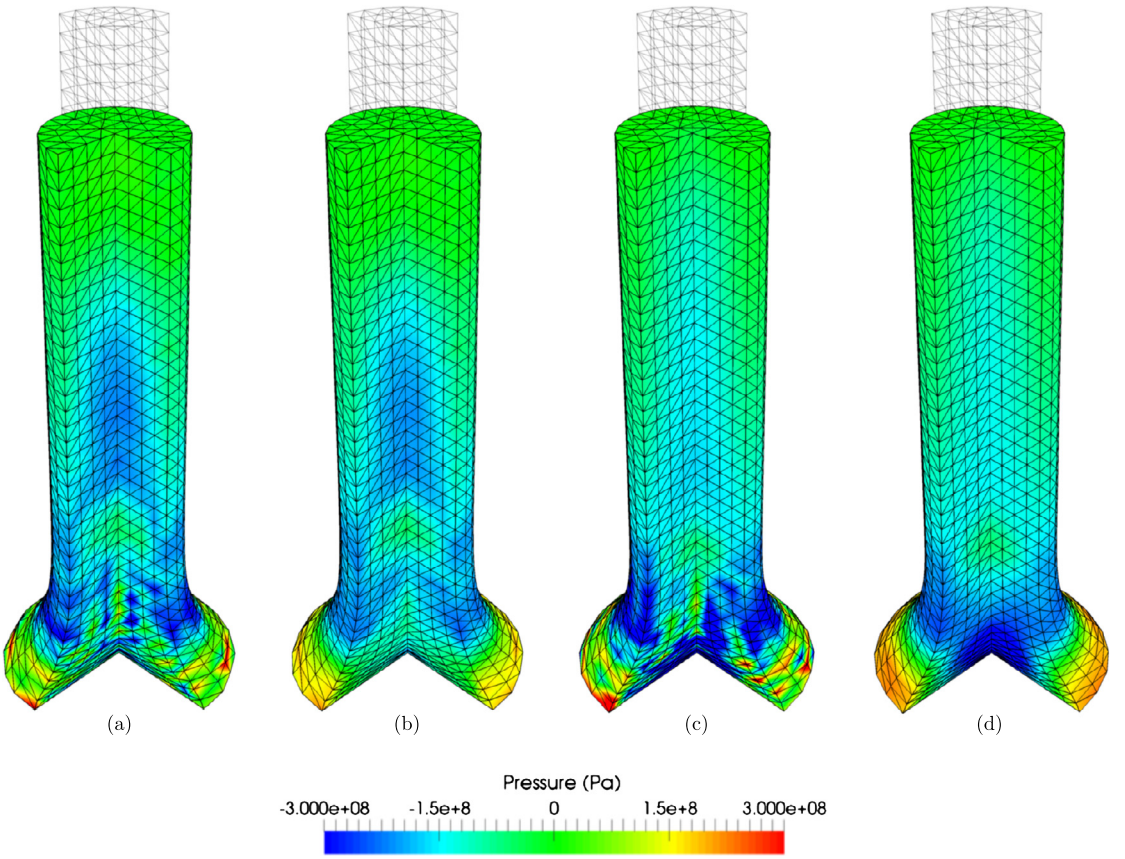

Fig. 20. Taylor impact. Comparison of deformed shapes plotted with pressures using various numerical schemes at a specific time $t = 20$ μs. (a) $\{\boldsymbol{p}, \boldsymbol{F}\}$ JST–TLF, (b) $\{\boldsymbol{p}, \boldsymbol{F}, J\}$ JST–TLF, (c) $\{\boldsymbol{p}, \boldsymbol{F}\}$ Upwind–TLF and (d) $\{\boldsymbol{p}, \boldsymbol{F}, J\}$ Upwind–TLF. Results are obtained with a constant velocity field $\boldsymbol{v}_0 = [0, 0, -227]^T$ m/s. A von Mises hyperelastic–plastic material with isotropic hardening is chosen with parameters, Young's modulus $E = 117$ GPa, density $\rho_0 = 8930$ kg/m^3, Poisson's ratio $\nu = 0.35$, Yield stress, $\bar{\tau}_y^0 = 0.4$ GPa, Hardening modulus $H = 0.1$ GPa, $k_{\boldsymbol{p}}^{(4)} = 1/256$, $k_J^{(4)} = 1/8192$ and $\alpha_{CFL} = 0.3$.

$E = 117$ GPa, density $\rho_0 = 8930$ kg/m^3, Poisson's ratio $\nu = 0.35$, yield stress $\bar{\tau}_y^0 = 0.4$ GPa and hardening modulus $H = 0.1$ GPa.

As shown in References [44,52,53], addition of the volume map conservation law to the $\{\boldsymbol{p}, \boldsymbol{F}\}$ system seems to be very efficient when solving problems with predominant nearly incompressible behaviours. In Figs. 20a,c, it is clear that both $\{\boldsymbol{p}, \boldsymbol{F}\}$ JST-TLF and $\{\boldsymbol{p}, \boldsymbol{F}\}$ Upwind-TLF schemes introduce spurious pressure modes. These non-physical pressure instabilities can be effectively removed using their counterpart $\{\boldsymbol{p}, \boldsymbol{F}, J\}$ stabilised methodologies (see Figs. 20b,d). Crucially, the $\{\boldsymbol{p}, \boldsymbol{F}, J\}$ Upwind-TLF and JST-TLF methodologies produce practically identical contours for both plastic strain and pressure at three different time instants (see Fig. 21). For verification purposes, the time history of the current coordinate of the material point $\boldsymbol{X} = [0.0032, 0, 0]^T$ is monitored, as shown in Fig. 22a. The figure also shows a mesh sensitivity study where a quarter of the domain is discretised using a linear tetrahedral mesh with 3 different mesh sizes: 3,833 (Coarse), 13,467 (Medium) and 60,957 elements (Fine). It is clear that the JST scheme requires a finer mesh in order to approach the converged solution. Both methodologies predict similar locking-free deformation with the final radius falling within an acceptable range of [6.8–7.3] mm [71].

6.8. Complex structure

In the last example of this paper, we demonstrate the robustness of the proposed finite volume algorithm on a complex geometry displayed in Fig. 22b. The geometry used in this example is that of a cardiovascular stent as reported in Reference [72]. The structure has an initial outer diameter of 20 mm, a thickness of 0.5 mm and a total length of 20 mm. The diameter of every hole is 2 mm. In this problem, we study the deformation pattern of the stent by applying a velocity field at the top and bottom of the structure, described as follows

$$\boldsymbol{v}_0 = \begin{cases} \left[0, 0, -\frac{ab\gamma}{(\gamma+1)^2}\right]^T & \text{if } t \leq 0.03 \text{ s} \\ \boldsymbol{0} & \text{otherwise} \end{cases}; \qquad \gamma = \exp\left[a(c-t)\right], \tag{68}$$

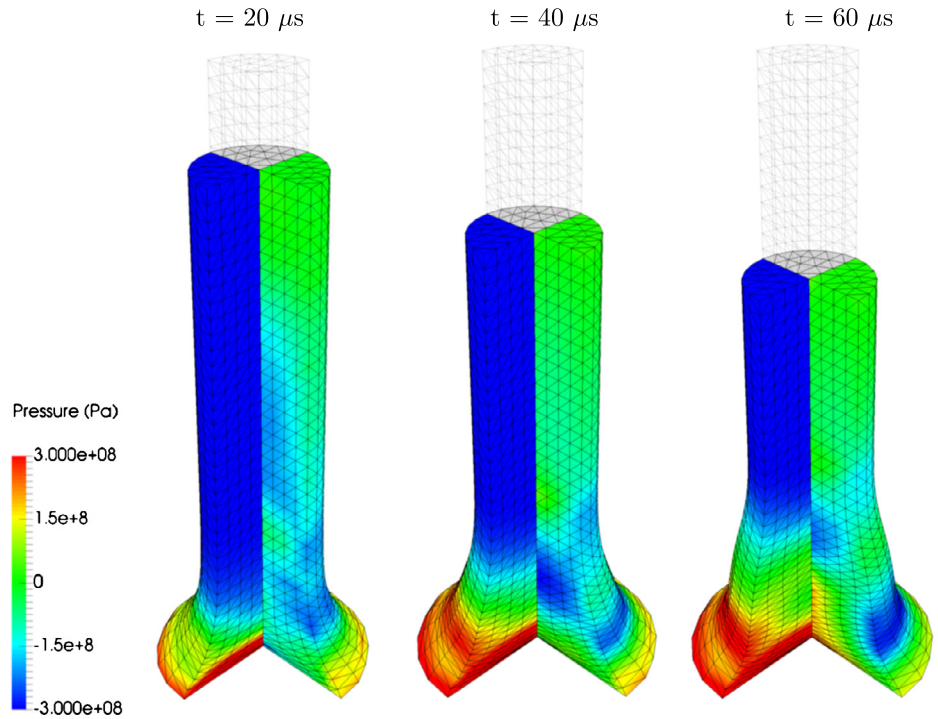

(a) $\{\boldsymbol{p},\boldsymbol{F},J\}$ JST–TLF

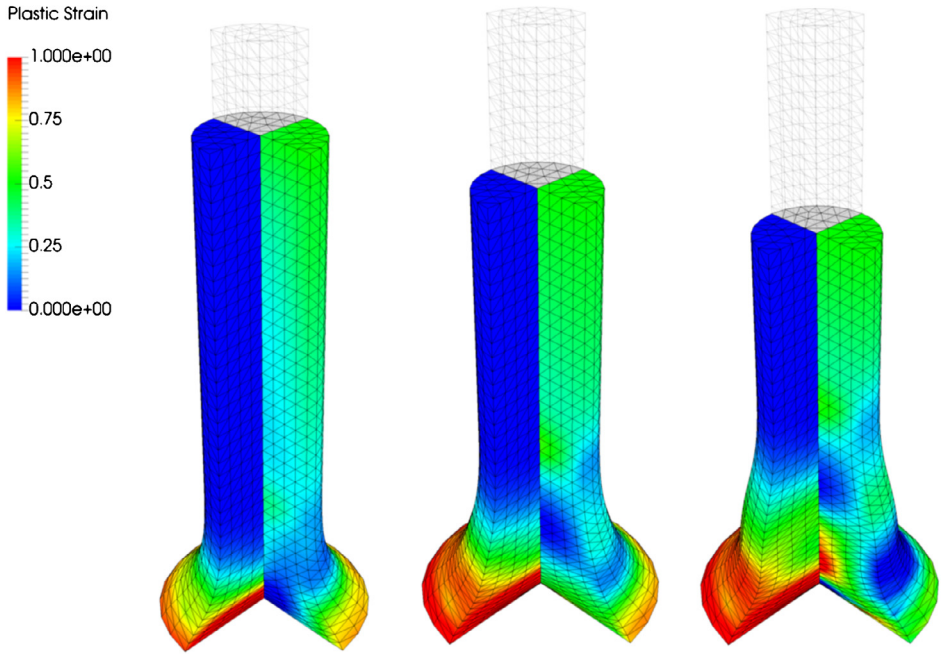

(b) $\{\boldsymbol{p},\boldsymbol{F},J\}$ Upwind–TLF

Fig. 21. Taylor impact. Comparison of deformed shapes at different times plotted with plastic strains (Left) and pressures (Right) using two different numerical schemes: (a) $\{\boldsymbol{p}, \boldsymbol{F}, J\}$ JST–TLF and (b) $\{\boldsymbol{p}, \boldsymbol{F}, J\}$ Upwind–TLF. Results are obtained with a constant velocity field $\boldsymbol{v}_0 = [0, 0, -227]^T$ m/s. A von Mises hyperelastic–plastic material with isotropic hardening is chosen with parameters, Young's modulus $E = 117$ GPa, density $\rho_0 = 8930$ kg/m^3, Poisson's ratio $\nu = 0.35$, Yield stress, $\bar{\tau}_y^0 = 0.4$ GPa, Hardening modulus $H = 0.1$ GPa, $k_{\boldsymbol{p}}^{(4)} = 1/256$, $k_J^{(4)} = 1/8192$ and $\alpha_{CFL} = 0.3$.

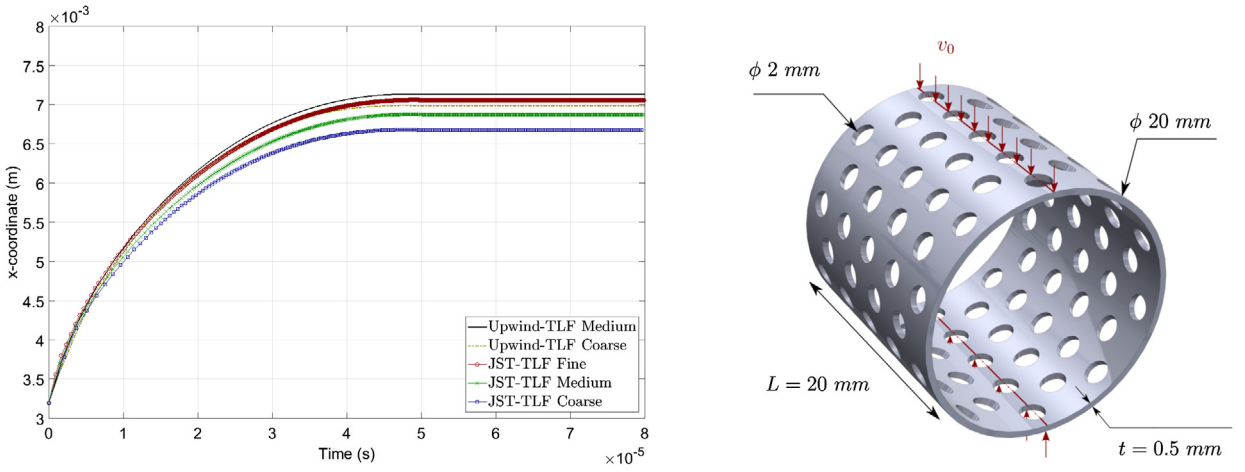

(a) Time history at $\boldsymbol{X} = (0.0032, 0, 0)^T$ (b) Stent geometry

Fig. 22. (a) Taylor impact: results are obtained using the $\{\boldsymbol{p}, \boldsymbol{F}, J\}$ Upwind–TLF scheme with a constant velocity field $\boldsymbol{v}_0 = [0, 0, -227]^T$ m/s. A von Mises hyperelastic–plastic material with isotropic hardening is chosen with parameters, Young's modulus $E = 117$ GPa, density $\rho_0 = 8930$ kg/m^3, Poisson's ratio $\nu = 0.35$, Yield stress, $\bar{\tau}_y^0 = 0.4$ GPa, Hardening modulus $H = 0.1$ GPa, and $\alpha_{CFL} = 0.3$. Quarter of the domain is discretised using linear tetrahedral mesh with 3,833 (Coarse), 13,467 (Medium) and 60,957 elements (Fine). (b) Medical stent geometry which is similar to the one reported in [72].

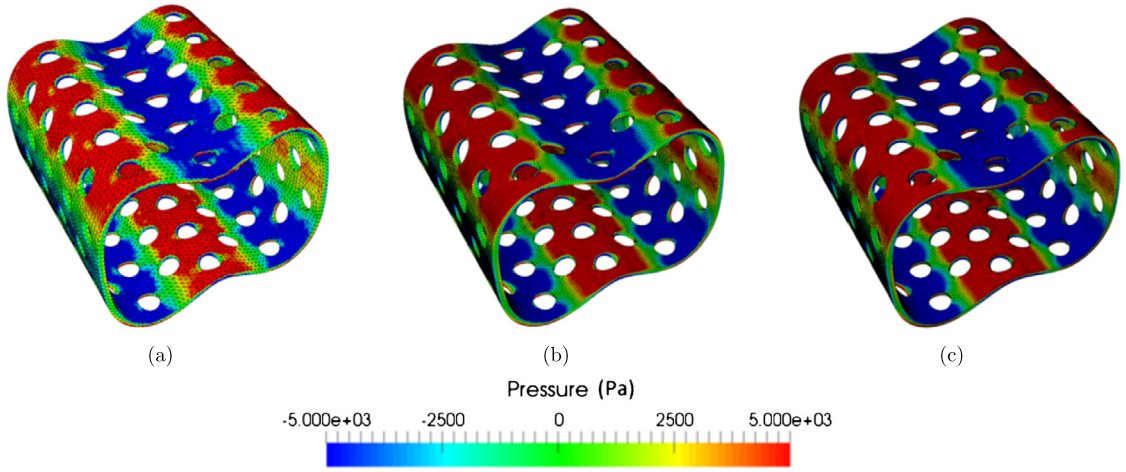

Fig. 23. Medical stent. Comparison of deformed shapes plotted with pressures using different meshes at a specific time $t = 0.016$ s. Results are obtained using the $\{\boldsymbol{p}, \boldsymbol{F}\}$ Upwind–TLF scheme with (a) coarse mesh, (b) medium mesh with one element across the thickness, and (c) fine mesh. A neo-Hookean material is used with density $\rho_0 = 1000$ kg/m^3, Young's modulus $E = 0.9$ MPa, Poisson's ratio $\nu = 0.45$ and $\alpha_{CFL} = 0.3$.

where $a = 800$ s^{-1}, $b = 0.006$ m and $c = 0.015$ s. Due to the presence of three symmetry planes, only one eighth of the problem is solved with appropriate boundary conditions. The structure is made of a nearly incompressible neo-Hookean material with density $\rho_0 = 1100$ kg/m^3, Young's Modulus $E = 17$ MPa and Poisson's ratio $\nu = 0.45$.

A mesh refinement study using the $\{\boldsymbol{p}, \boldsymbol{F}\}$ Upwind-TLF is presented in Fig. 23. Sequentially refined meshes of 7567, 45270 and 50,527 tetrahedral elements are used with the purpose of comparing the resolution of the deformed structure at time $t = 0.016$ s. It is interesting to notice that reasonably accurate deformations can be obtained even with the use of only one element across the thickness of the structure.

As illustrated in Fig. 24, all of the proposed Total Lagrangian upwind methodologies, namely $\{\boldsymbol{p}, \boldsymbol{F}\}$, $\{\boldsymbol{p}, \boldsymbol{F}, J\}$ and $\{\boldsymbol{p}, \boldsymbol{F}, \boldsymbol{H}, J\}$ Upwind-TLF schemes, are capable of capturing highly nonlinear structural deformations without exhibiting any spurious pressure modes.

For completeness, the time history of the vertical displacement monitored at point $\boldsymbol{X} = [r/2, 0, \sqrt{3/4}\, r]^T$ is also shown in Fig. 25. Remarkably, it is clear from observation that the deformation is locking-free and with a smooth pressure pattern, showing optimal convergence for the proposed method. This opens up interesting possibilities for the modelling in biomechanics [72], where this consideration is very relevant.

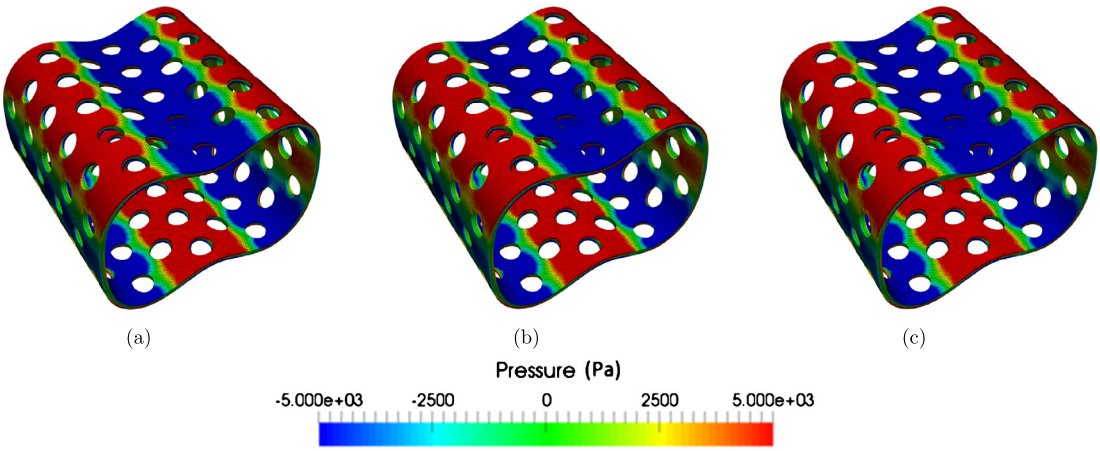

Fig. 24. Medical stent. Comparison of deformed shapes plotted with pressures using different schemes at a specific time $t = 0.016$ s. Results are obtained using the (a) $\{\boldsymbol{p}, \boldsymbol{F}\}$ Upwind–TLF, (b) $\{\boldsymbol{p}, \boldsymbol{F}, J\}$ Upwind–TLF and (c) $\{\boldsymbol{p}, \boldsymbol{F}, \boldsymbol{H}, J\}$ Upwind–TLF scheme. A neo-Hookean material is used with density $\rho_0 = 1000$ kg/m^3, Young's modulus $E = 0.9$ MPa, Poisson's ratio $\nu = 0.45$ and $\alpha_{CFL} = 0.3$.

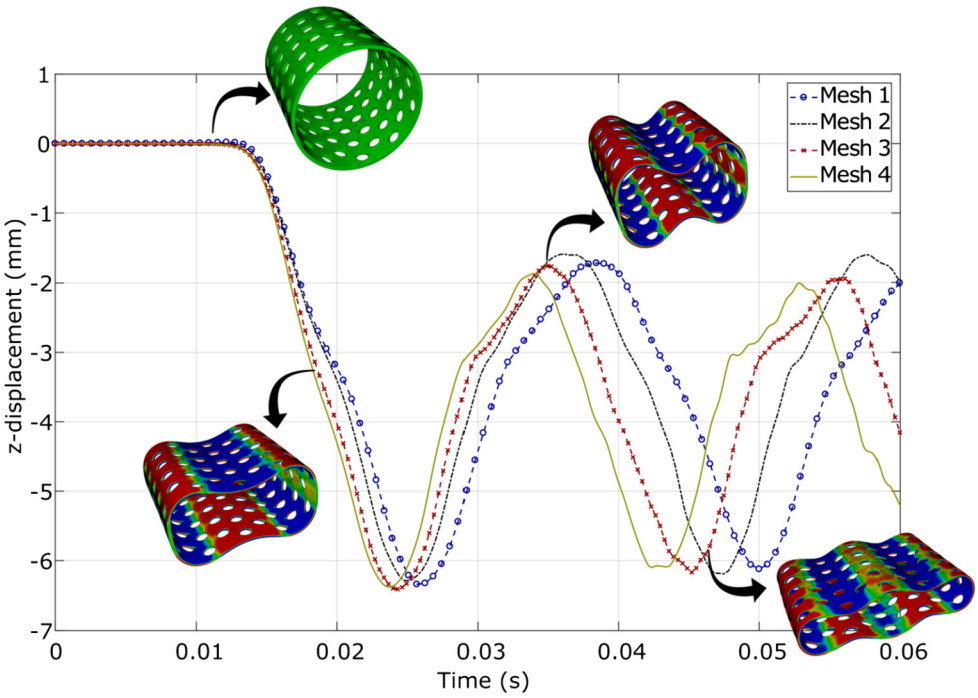

Fig. 25. Medical stent. Time history of the $\boldsymbol{z}$ displacement of the point $\boldsymbol{X} = [r/2, 0, \sqrt{3/4}\ r]^T$. Results are obtained using the $\{\boldsymbol{p}, \boldsymbol{F}\}$ Upwind–TLF scheme. A neo-Hookean material is used with density $\rho_0 = 1000$ kg/m^3, Young's modulus $E = 0.9$ MPa, Poisson's ratio $\nu = 0.45$ and $\alpha_{CFL} = 0.3$. Linear tetrahedral mesh is used to discretise $\frac{1}{8}$ of the domain with 7,567 (Mesh 1), 45,270 (mesh 2), 50,527 (Mesh 3) and 134,168 elements (Mesh 4).

7. Concluding remarks

The paper presents a vertex centred finite volume method for the solution of fast transient isothermal large strain solid dynamics, where a mixed system of first order conservation laws is solved. Both Total and Updated Lagrangian formulations are presented and compared at the discrete level, where very small differences between both descriptions are observed due to the excellent discrete satisfaction of the involutions. It has been shown that non-physical zero energy modes and spurious pressure instabilities can be effectively alleviated when attempting to model nearly incompressible solids. This is done by means of upwinding dissipation which is compared against a JST algorithm. In terms of computational efficiency, an artificial compressibility approach is formulated and suitably adapted when dealing with very large (or even indefinite) wave speeds. Finally, a comprehensive set of challenging numerical examples is presented in order to assess the accuracy, reliability and robustness of the proposed methodologies. The proposed framework shows excellent behaviour in nearly incompressible bending dominated scenarios, yielding second order of convergence for velocities, deviatoric and volumetric components of

the stress. The consideration of an Arbitrary Lagrangian Eulerian description within the current computational framework is the next step of our work.

Declaration of Competing Interest

The authors declare that they have no known competing financial interests or personal relationships that could have appeared to influence the work reported in this paper.

Acknowledgements

The authors gratefully acknowledge the financial support provided by the Sêr Cymru National Research Network for Advanced Engineering and Materials (Grant No. G05), United Kingdom. The first and second authors would also like to acknowledge the financial support received through the European Commission EACEA Agency, Framework Partnership Agreement 2013-0043 Erasmus Mundus Action 1b, as a part of the EM Joint Doctorate "Simulation in Engineering and Entrepreneurship Development (SEED)".

Appendix A. Entropy property

For completeness, it is possible to include the total energy conservation law into our mixed system as

$$\frac{d}{dt}\int_{\Omega_0} E\, d\Omega_0 = \int_{\partial\Omega_0} \frac{1}{\rho_0}\boldsymbol{p}\cdot\boldsymbol{t}\, dA - \int_{\partial\Omega_0} \boldsymbol{Q}\cdot\boldsymbol{N}\, dA + \int_{\Omega_0} s\, d\Omega_0 + \int_{\Omega_0}\frac{1}{\rho_0}\boldsymbol{p}\cdot\boldsymbol{f}_0\, d\Omega_0, \tag{69}$$

where E is the total energy per unit of undeformed volume and $\boldsymbol{Q}$ and s represent the heat flux and the heat source terms, respectively. In the case of an adiabatic deformation, the heat flux $\boldsymbol{Q}$ and the heat source s are neglected. In addition, when dealing with non-thermomechanical materials, equation (69) is fully decoupled from the rest of the system of conservation laws (10). Even in this case, from the computational point of view, this equation is still very useful when evaluating the time rate of numerical entropy (diffusion) $\dot{\mathcal{D}}_p(t)$ introduced by the algorithm.

To achieve this, it is necessary to discretise the above conservation equation for an arbitrary control volume a to give

$$\Omega_a^0\frac{dE_a}{dt} = \sum_{b\in\Lambda_a}\frac{1}{\rho_0}\boldsymbol{p}_{ab}^{\text{Ave}}\cdot\left(\boldsymbol{P}_{ab}^{\text{Ave}}\boldsymbol{C}_{ab}\right) + \sum_{\gamma\in\Lambda_a^B}\frac{1}{\rho_0}\boldsymbol{p}_a^\gamma\cdot\boldsymbol{t}_a^\gamma\,||\boldsymbol{C}_\gamma|| + \frac{\Omega_a^0}{\rho_0}\boldsymbol{p}_a\cdot\boldsymbol{f}_0^a. \tag{70}$$

Multiplying the complete set of $\{\boldsymbol{p}_a, \boldsymbol{F}_a, \boldsymbol{H}_a, J_a\}$ semi-discrete equations (expressed in (40a) and (43a)–(43c)) by their dual conjugate variables $\{\boldsymbol{v}_a, \boldsymbol{\Sigma}_{\boldsymbol{F}}^a, \boldsymbol{\Sigma}_{\boldsymbol{H}}^a, \Sigma_J^a\}$, subtracting them from equation (70) and adding over all nodes a of the computational mesh, gives, after some simple algebra,

$$\dot{\mathcal{D}}_p(t) := \sum_a \Omega_a^0\left[\frac{dE_a}{dt} - \frac{\boldsymbol{p}_a}{\rho_0}\cdot\frac{d\boldsymbol{p}_a}{dt} - \boldsymbol{\Sigma}_{\boldsymbol{F}}^a : \frac{d\boldsymbol{F}_a}{dt} - \boldsymbol{\Sigma}_{\boldsymbol{H}}^a : \frac{d\boldsymbol{H}_a}{dt} - \Sigma_J^a\frac{dJ_a}{dt}\right] \tag{71a}$$

$$= \sum_a\sum_{b\in\Lambda_a}\left[\left(\boldsymbol{P}_{ab}^{\text{Ave}}\boldsymbol{C}_{ab}\right)\cdot\frac{\boldsymbol{p}_{ab}^{\text{Ave}}}{\rho_0} - \left(\boldsymbol{P}_{ab}^{\text{Ave}}\boldsymbol{C}_{ab}\right)\cdot\frac{\boldsymbol{p}_a}{\rho_0} - \boldsymbol{P}_a : \left(\frac{\boldsymbol{p}_{ab}^{\text{Ave}}}{\rho_0}\otimes\boldsymbol{C}_{ab}\right)\right]$$

$$- \sum_a\sum_{b\in\Lambda_a}\left(\frac{\boldsymbol{p}_a}{\rho_0}\cdot\boldsymbol{\mathcal{D}}_{ab}^{\boldsymbol{p}} + \Sigma_J^a\mathcal{D}_{ab}^J\right) \tag{71b}$$

$$= \sum_a\frac{1}{2\rho_0}\left[\sum_{b\in\Lambda_a}\left(\boldsymbol{P}_{ab}^{\text{Ave}}\boldsymbol{C}_{ab}\right)\cdot(\boldsymbol{p}_b-\boldsymbol{p}_a) - \sum_{b\in\Lambda_a}(\boldsymbol{P}_a\boldsymbol{C}_{ab})\cdot(\boldsymbol{p}_a+\boldsymbol{p}_b)\right]$$

$$- \sum_a\sum_{b\in\Lambda_a}\left(\frac{\boldsymbol{p}_a}{\rho_0}\cdot\boldsymbol{\mathcal{D}}_{ab}^{\boldsymbol{p}} + \Sigma_J^a\mathcal{D}_{ab}^J\right), \tag{71c}$$

where $\boldsymbol{P}_a = \boldsymbol{\Sigma}_{\boldsymbol{F}}^a + \boldsymbol{\Sigma}_{\boldsymbol{H}}^a \times \boldsymbol{F}_a + \Sigma_J^a\boldsymbol{H}_a$. Since $\sum_{b\in\Lambda_a}\boldsymbol{C}_{ab} = \boldsymbol{0}$, we could then add the redundant term $\frac{1}{\rho_0}\sum_{b\in\Lambda_a}(\boldsymbol{P}_a\boldsymbol{C}_{ab})\cdot\boldsymbol{p}_a$ to the above expression, yielding

$$\dot{\mathcal{D}}_p(t) = \sum_a\frac{1}{2\rho_0}\left[\sum_{b\in\Lambda_a}\left(\boldsymbol{P}_{ab}^{\text{Ave}}\boldsymbol{C}_{ab}\right)\cdot(\boldsymbol{p}_b-\boldsymbol{p}_a) - \sum_{b\in\Lambda_a}(\boldsymbol{P}_a\boldsymbol{C}_{ab})\cdot(\boldsymbol{p}_a+\boldsymbol{p}_b) + \sum_{b\in\Lambda_a}2\,(\boldsymbol{P}_a\boldsymbol{C}_{ab})\cdot\boldsymbol{p}_a\right]$$
$$- \sum_a\sum_{b\in\Lambda_a}\left(\frac{\boldsymbol{p}_a}{\rho_0}\cdot\boldsymbol{\mathcal{D}}_{ab}^{\boldsymbol{p}} + \Sigma_J^a\mathcal{D}_{ab}^J\right), \tag{72}$$

After substitution of (41) into (72), it yields

$$\begin{aligned}\dot{\mathcal{D}}_p(t) = &\frac{1}{4\rho_0}\sum_a\sum_{b\in\Lambda_a}\left[(\boldsymbol{P}_b-\boldsymbol{P}_a)\,\boldsymbol{C}_{ab}\right]\cdot\left(\boldsymbol{p}_b-\boldsymbol{p}_a\right)\\ &-\frac{1}{2\rho_0}\sum_a\sum_{b\in\Lambda_a}||\boldsymbol{C}_{ab}||\boldsymbol{p}_a\cdot\left[\boldsymbol{\mathcal{S}}^{\boldsymbol{p}}_{ab}\left(\boldsymbol{p}_b-\boldsymbol{p}_a\right)\right]\\ &-\frac{1}{2\rho_0}\sum_a\sum_{b\in\Lambda_a}\Sigma^a_J||\boldsymbol{C}_{ab}||\left(\Sigma^b_J-\Sigma^a_J\right)\left(\boldsymbol{H}^{\text{Ave}}_{ab}\boldsymbol{N}_{ab}\right)\cdot\left[\boldsymbol{\mathcal{S}}^{\boldsymbol{t}}_{ab}\left(\boldsymbol{H}^{\text{Ave}}_{ab}\boldsymbol{N}_{ab}\right)\right].\end{aligned} \tag{73}$$

Notice here that the evaluation of $\{\boldsymbol{\mathcal{D}}^{\boldsymbol{p}}_{ab},\mathcal{D}^J_{ab}\}$ is carried out by utilising a piecewise constant representation for $\{\boldsymbol{p},\Sigma_J\}$ and, more importantly, the summation is carried out over control volumes. Rearranging the above summation over edges connecting a and b gives

$$\dot{\mathcal{D}}_p(t)=\sum_{\substack{\text{edges}\\ a\leftrightarrow b}}\dot{\mathcal{D}}^{ab}_p(t), \tag{74}$$

where the edge based entropy production is defined as

$$\dot{\mathcal{D}}^{ab}_p(t):=\frac{1}{2\rho_0}||\boldsymbol{C}_{ab}||\left[\left(\boldsymbol{p}_b-\boldsymbol{p}_a\right)\cdot\left[\boldsymbol{\mathcal{S}}^{\boldsymbol{p}}_{ab}\left(\boldsymbol{p}_b-\boldsymbol{p}_a\right)\right]+\left(\Sigma^b_J-\Sigma^a_J\right)^2\left(\boldsymbol{H}^{\text{Ave}}_{ab}\boldsymbol{N}_{ab}\right)\cdot\left[\boldsymbol{\mathcal{S}}^{\boldsymbol{t}}_{ab}\left(\boldsymbol{H}^{\text{Ave}}_{ab}\boldsymbol{N}_{ab}\right)\right]\right]. \tag{75}$$

It is now easy to show that both positive definite stabilisation matrices $\{\boldsymbol{S}^{\boldsymbol{p}}_{ab},\boldsymbol{S}^{\boldsymbol{t}}_{ab}\}$ (refer to (37)) used in this paper guarantee non-negative local entropy production for every edge, that is $\dot{\mathcal{D}}^{ab}_p(t)\geq 0$. This demonstrates the entropy production for the semi-discrete scheme. It is now easy to show that this is also respected in the fully discrete case for the particular TVD-RK time integration scheme used in this work. Indeed, equations (50) can be combined to give (after replacing $\boldsymbol{\mathcal{U}}_a$ with $\mathcal{D}^{ab}_p$)

$$\frac{\mathcal{D}^{ab,n+1}_p-\mathcal{D}^{ab,n}_p}{\Delta t}=\frac{1}{2}\left(\dot{\mathcal{D}}^{ab,n}_p+\dot{\mathcal{D}}^{ab,\star}_p\right). \tag{76}$$

By noticing that both terms on the right hand side of above equation are positive each (as demonstrated in (75)), it is immediate to conclude the satisfaction of entropy production in the discrete setting.

Appendix B. Involutions

One of the challenging issues in the process of the time-evolving expressions (44b), (44c) is the ability to control the onset and propagation of spurious mechanisms over a long term response [43]. To ensure the fulfilment of specific involutions (3), a discrete area map projection algorithm is presented. Specifically, the area map tensors $\{\boldsymbol{H}^{\text{Ave}}_{ab},\boldsymbol{H}_a\}$ described in (44b)–(44c) must be suitably modified (in a least-square sense) in order to satisfy the following mapping constraints described as follows

$$\boldsymbol{H}^{\text{Ave}}_{ab}\boldsymbol{C}_{ab}=\boldsymbol{c}_{ab};\qquad \boldsymbol{H}_a\boldsymbol{C}_\gamma=\boldsymbol{c}_\gamma. \tag{77}$$

A least-square minimisation procedure is first used to obtain a modified set of area map $\mathbf{H}^{\text{Ave}}_{ab}$ that satisfy the above condition (77a). This can be achieved by introducing a functional Π defined by

$$\Pi(\mathbf{H}^{\text{Ave}}_{ab},\boldsymbol{\lambda}_{ab})=\frac{1}{2}(\mathbf{H}^{\text{Ave}}_{ab}-\boldsymbol{H}^{\text{Ave}}_{ab}):(\mathbf{H}^{\text{Ave}}_{ab}-\boldsymbol{H}^{\text{Ave}}_{ab})-\boldsymbol{\lambda}_{ab}\cdot\left(\mathbf{H}^{\text{Ave}}_{ab}\boldsymbol{C}_{ab}-\boldsymbol{c}_{ab}\right). \tag{78}$$

The stationary condition of the above functional with respect to $\boldsymbol{\lambda}_{ab}$ and $\mathbf{H}^{\text{Ave}}_{ab}$ will be considered separately. To this effect, note firstly that the derivative of Π with respect to $\boldsymbol{\lambda}_{ab}$ leads to the mapping constraint (77a) applied to the modified area map $\mathbf{H}^{\text{Ave}}_{ab}$.

Additionally, the derivative of the functional in (78) with respect to $\mathbf{H}^{\text{Ave}}_{ab}$ results in

$$\mathbf{H}^{\text{Ave}}_{ab}=\boldsymbol{H}^{\text{Ave}}_{ab}+\boldsymbol{\lambda}_{ab}\otimes\boldsymbol{C}_{ab}. \tag{79}$$

Use of (77a) with $\boldsymbol{H}^{\text{Ave}}_{ab}$ replaced with $\mathbf{H}^{\text{Ave}}_{ab}$ in conjunction with (79), the Lagrange multiplier $\boldsymbol{\lambda}_{ab}$ is the solution to the following system of equations, that is

$$\boldsymbol{\lambda}_{ab}=\frac{1}{(\boldsymbol{C}_{ab}\cdot\boldsymbol{C}_{ab})}\left[\boldsymbol{c}_{ab}-\boldsymbol{H}^{\text{Ave}}_{ab}\boldsymbol{C}_{ab}\right]. \tag{80}$$

Similarly, a modified boundary area map, namely $\mathbf{H}_a$, can be obtained by replacing $\{\mathbf{H}^{\text{Ave}}_{ab},\boldsymbol{H}^{\text{Ave}}_{ab},\boldsymbol{C}_{ab},\boldsymbol{c}_{ab},\boldsymbol{\lambda}_{ab}\}$ in (79) and (80) with $\{\mathbf{H}_a,\boldsymbol{H}_a,\boldsymbol{C}_\gamma,\boldsymbol{c}_\gamma,\boldsymbol{\lambda}_\gamma\}$, respectively.

References

[1] F.M.A. Pires, E.A. de Souza Neto, J.L. de la Cuesta Padilla, An assessment of the average nodal volume formulation for the analysis of nearly incompressible solids under finite strains, Commun. Numer. Methods Eng. 20 (2004) 569–583.
[2] J. Bonet, H. Marriott, O. Hassan, An averaged nodal deformation gradient linear tetrahedral element for large strain explicit dynamic applications, Commun. Numer. Methods Eng. 17 (2001) 551–561.
[3] Y. Onishi, K. Amaya, A locking-free selective smoothed finite element method using tetrahedral and triangular elements with adaptive mesh rezoning for large deformation problems, Int. J. Numer. Methods Eng. 99 (2014) 354–371.
[4] H.M. Hilber, T.J.R. Hughes, R.L. Taylor, Improved numerical dissipation for time integration algorithms in structural dynamics, Earthq. Eng. Struct. Dyn. 5 (1977) 283–292.
[5] W.L. Wood, M. Bossak, O.C. Zienkiewicz, An alpha modification of Newmark's method, Int. J. Numer. Methods Eng. 15 (1980) 1562–1566.
[6] T. Belytschko, J.S. Ong, W.K. Liu, J.M. Kennedy, Hourglass control in linear and nonlinear problems, Comput. Methods Appl. Mech. Eng. 43 (1984) 251–276.
[7] D.P. Flanagan, T. Belytschko, A uniform strain hexahedron and quadrilateral with orthogonal hourglass control, Int. J. Numer. Methods Eng. 17 (1981) 679–706.
[8] T.J.R. Hughes, Generalization of selective integration procedures to anisotropic and nonlinear media, Int. J. Numer. Methods Eng. 15 (1980) 1413–1418.
[9] A.J. Gil, P.D. Ledger, A coupled *hp*-finite element scheme for the solution of two-dimensional electrostrictive materials, Int. J. Numer. Methods Eng. 91 (2012) 1158–1183.
[10] X. Zeng, G. Scovazzi, N. Abboud, O. Colomes, S. Rossi, A dynamic variational multiscale method for viscoelasticity using linear tetrahedral elements, Int. J. Numer. Methods Eng. 112 (2017) 1951–2003.
[11] J. Bonet, A.J. Burton, A simple average nodal pressure tetrahedral element for incompressible and nearly incompressible dynamic explicit applications, Commun. Numer. Methods Eng. 14 (1998) 437–449.
[12] S.K. Lahiri, J. Bonet, J. Peraire, A variationally consistent mesh adaptation method for triangular elements in explicit Lagrangian dynamics, Int. J. Numer. Methods Eng. 82 (2010) 1073–1113.
[13] M.W. Gee, C.R. Dohrmann, S.W. Key, W.A. Wall, A uniform nodal strain tetrahedron with isochoric stabilization, Int. J. Numer. Methods Eng. 78 (2009) 429–443.
[14] M.A. Puso, J. Solberg, A stabilized nodally integrated tetrahedral, Int. J. Numer. Methods Eng. 67 (2006) 841–867.
[15] C. Dohrmann, M.W. Heinstein, J. Jung, S.W. Key, W.R. Witkowski, Node-based uniform strain elements for three-node triangular and four-node tetrahedral meshes, Int. J. Numer. Methods Eng. 47 (2000) 1549–1568.
[16] J. Bonet, H. Marriott, O. Hassan, Stability and comparison of different linear tetrahedral formulations for nearly incompressible explicit dynamic applications, Int. J. Numer. Methods Eng. 50 (2001) 119–133.
[17] J. Bonet, H. Marriott, O. Hassan, An averaged nodal deformation gradient linear tetrahedral element for large strain explicit dynamic applications, Commun. Numer. Methods Eng. 17 (2001) 551–561.
[18] E. de Souza Neto, D. Perić, M. Dutko, D. Owen, Design of simple low order finite elements for large strain analysis of nearly incompressible solids, Int. J. Solids Struct. 33 (1996) 3277–3296.
[19] Y. Onishi, F-bar aided edge-based smoothed finite element method with 4-node tetrahedral elements for static large deformation elastoplastic problems, Int. J. Comput. Methods (2017) 1840010.
[20] A.K. Slone, C. Bailey, M. Cross, Dynamic solid mechanics using finite volume methods, Appl. Math. Model. 27 (2003) 69–87.
[21] G.A. Taylor, C. Bailey, M. Cross, A vertex-based finite volume method applied to non-linear material problems in computational solid mechanics, Int. J. Numer. Methods Eng. 56 (2003) 507–529.
[22] H. Jasak, H.G. Weller, Application of the finite volume method and unstructured meshes to linear elasticity, Int. J. Numer. Methods Eng. 48 (2000) 267–287.
[23] I. Bijelonja, I. Demirdžić, S. Muzaferija, A finite volume method for incompressible linear elasticity, Comput. Methods Appl. Mech. Eng. 195 (2006) 6378–6390.
[24] P. Cardiff, A. Karač, A. Ivanković, Development of a finite volume contact solver based on the penalty method, Comput. Mater. Sci. 64 (2012) 283–284.
[25] P. Cardiff, A. Karač, A. Ivanković, A large strain finite volume method for orthotropic bodies with general material orientations, Comput. Methods Appl. Mech. Eng. 268 (2014) 318–335.
[26] P. Cardiff, Ž. Tuković, P.D. Jaeger, M. Clancy, A. Ivanković, A Lagrangian cell-centred finite volume method for metal forming simulation, Int. J. Numer. Methods Eng. 109 (2017) 1777–1803.
[27] J.A. Trangenstein, P. Colella, A higher-order Godunov method for modeling finite deformation in elastic-plastic solids, Commun. Pure Appl. Math. 44 (1991) 41–100.
[28] J.A. Trangenstein, A second-order Godunov algorithm for two-dimensional solid mechanics, Comput. Mech. 13 (1994) 343–359.
[29] B. Després, C. Mazeran, Lagrangian gas dynamics in two dimensions and Lagrangian systems, Arch. Ration. Mech. Anal. 178 (2005) 327–372.
[30] P.-H. Maire, R. Abgrall, J. Breil, J. Ovadia, A cell-centered Lagrangian scheme for two-dimensional compressible flow problems, SIAM J. Sci. Comput. 29 (2007) 1781–1824.
[31] P.H. Maire, A high-order cell-centered Lagrangian scheme for compressible fluid flows in two-dimensional cylindrical geometry, J. Comput. Phys. 228 (2009) 6882–6915.
[32] P.-H. Maire, B. Nkonga, Multi-scale Godunov-type method for cell-centered discrete Lagrangian hydrodynamics, J. Comput. Phys. 228 (2009) 799–821.
[33] G. Carré, S. Del Pino, B. Després, E. Labourasse, A cell-centered Lagrangian hydrodynamics scheme on general unstructured meshes in arbitrary dimension, J. Comput. Phys. 228 (2009) 5160–5183.
[34] D.E. Burton, T.C. Carney, N.R. Morgan, S.K. Sambasivan, M.J. Shashkov, A cell-centered Lagrangian Godunov-like method for solid dynamics, Comput. Fluids 83 (2013) 33–47.
[35] P.-H. Maire, R. Abgrall, J. Breil, R. Loubere, B. Rebourcet, A nominally second-order cell-centered Lagrangian scheme for simulating elastic-plastic flows on two dimensional unstructured grids, J. Comput. Phys. 235 (2013) 626–665.
[36] V.A. Dobrev, T.V. Kolev, R.N. Rieben, High order curvilinear finite elements for elastic–plastic Lagrangian dynamics, J. Comput. Phys. 257 (2014) 1062–1080.
[37] G. Kluth, B. Després, Discretization of hyperelasticity on unstructured mesh with a cell-centered Lagrangian scheme, J. Comput. Phys. 229 (2010) 9092–9118.
[38] G. Georges, J. Breil, P.H. Maire, A 3D finite volume scheme for solving the updated Lagrangian form of hyperelasticity, Int. J. Numer. Methods Fluids 84 (2017) 41–54.
[39] G. Scovazzi, B. Carnes, X. Zeng, S. Rossi, A simple, stable, and accurate linear tetrahedral finite element for transient, nearly, and fully incompressible solid dynamics: a dynamic variational multiscale approach, Int. J. Numer. Methods Eng. 106 (2015) 799–839.
[40] G. Scovazzi, T. Song, X. Zeng, A velocity/stress mixed stabilized nodal finite element for elastodynamics: analysis and computations with strongly and weakly enforced boundary conditions, Comput. Methods Appl. Mech. Eng. 325 (2017) 532–576.

[41] N. Abboud, G. Scovazzi, Elastoplasticity with linear tetrahedral elements: a variational multiscale method, Int. J. Numer. Methods Eng. 115 (2018) 913–955.
[42] S. Rossi, N. Abboud, G. Scovazzi, Implicit finite incompressible elastodynamics with linear finite elements: a stabilized method in rate form, Comput. Methods Appl. Mech. Eng. 311 (2016) 208–249.
[43] C.H. Lee, A.J. Gil, J. Bonet, Development of a cell centred upwind finite volume algorithm for a new conservation law formulation in structural dynamics, Comput. Struct. 118 (2013) 13–38.
[44] J. Haider, C.H. Lee, A.J. Gil, J. Bonet, A first-order hyperbolic framework for large strain computational solid dynamics: an upwind cell centred Total Lagrangian scheme, Int. J. Numer. Methods Eng. 109 (2017) 407–456.
[45] M. Aguirre, A.J. Gil, J. Bonet, A. Arranz-Carreño, A vertex centred finite volume Jameson-Schmidt-Turkel (JST) algorithm for a mixed conservation formulation in solid dynamics, J. Comput. Phys. 259 (2014) 672–699.
[46] M. Aguirre, A.J. Gil, J. Bonet, C.H. Lee, An upwind vertex centred finite volume solver for Lagrangian solid dynamics, J. Comput. Phys. 300 (2015) 387–422.
[47] I.A. Karim, A Two-step Taylor-Galerkin Formulation For Explicit Solid Dynamics Large Strain Problems, PhD thesis, Civil Engineering Dept. Swansea University, 2011.
[48] C.H. Lee, A.J. Gil, J. Bonet, Development of a stabilised Petrov-Galerkin formulation for conservation laws in Lagrangian fast solid dynamics, Comput. Methods Appl. Mech. Eng. 268 (2014) 40–64.
[49] A.J. Gil, C.H. Lee, J. Bonet, M. Aguirre, A stabilised Petrov-Galerkin formulation for linear tetrahedral elements in compressible, nearly incompressible and truly incompressible fast dynamics, Comput. Methods Appl. Mech. Eng. 276 (2014) 659–690.
[50] A.J. Gil, C.H. Lee, J. Bonet, R. Ortigosa, A first order hyperbolic framework for large strain computational solid dynamics. Part II: Total Lagrangian compressible, nearly incompressible and truly incompressible elasticity, Comput. Methods Appl. Mech. Eng. 300 (2016) 146–181.
[51] J. Bonet, A.J. Gil, C.H. Lee, M. Aguirre, R. Ortigosa, A first order hyperbolic framework for large strain computational solid dynamics. Part I: Total Lagrangian isothermal elasticity, Comput. Methods Appl. Mech. Eng. 283 (2015) 689–732.
[52] C.H. Lee, A.J. Gil, G. Greto, S. Kulasegaram, J. Bonet, A new Jameson–Schmidt–Turkel Smooth Particle Hydrodynamics algorithm for large strain explicit fast dynamics, Comput. Methods Appl. Mech. Eng. 311 (2016) 71–111.
[53] C.H. Lee, A.J. Gil, O.I. Hassan, J. Bonet, S. Kulasegaram, A variationally consistent Streamline Upwind Petrov Galerkin Smooth Particle Hydrodynamics algorithm for large strain solid dynamics, Comput. Methods Appl. Mech. Eng. 318 (2017) 514–536.
[54] C.H. Lee, A.J. Gil, A. Ghavamian, J. Bonet, A Total Lagrangian upwind Smooth Particle Hydrodynamics algorithm for large strain explicit solid dynamics, Comput. Methods Appl. Mech. Eng. 344 (2019) 209–250.
[55] A.J. Gil, C.H. Lee, J. Bonet, R. Ortigosa, A first order hyperbolic framework for large strain computational solid dynamics. Part II: Total Lagrangian compressible, nearly incompressible and truly incompressible elasticity, Comput. Methods Appl. Mech. Eng. 300 (2016) 146–181.
[56] J. Bonet, A.J. Gil, C.H. Lee, M. Aguirre, R. Ortigosa, A first order hyperbolic framework for large strain computational solid dynamics. Part I: Total Lagrangian isothermal elasticity, Comput. Methods Appl. Mech. Eng. 283 (2015) 689–732.
[57] I.A. Karim, C.H. Lee, A.J. Gil, J. Bonet, A two-step Taylor-Galerkin formulation for fast dynamics, Eng. Comput. 31 (2014) 366–387.
[58] N.C. Nguyen, J. Peraire, Hybridizable Discontinuous Galerkin methods for partial differential equations in continuum mechanics, J. Comput. Phys. 231 (2012) 5955–5988.
[59] J. Bonet, A.J. Gil, R. Ortigosa, On a tensor cross product based formulation of large strain solid mechanics, Int. J. Solids Struct. 84 (2016) 49–63.
[60] J. Bonet, A.J. Gil, R. Ortigosa, A computational framework for polyconvex large strain elasticity, Comput. Methods Appl. Mech. Eng. 283 (2015) 1061–1094.
[61] F. Vilar, P.-H. Maire, R. Abgrall, A discontinuous Galerkin discretization for solving the two-dimensional gas dynamics equations written under total Lagrangian formulation on general unstructured grids, J. Comput. Phys. 276 (2014) 188–234.
[62] M. Torrilhon, M. Fey, Constraint-preserving upwind methods for multidimensional advection equations, SIAM J. Numer. Anal. 42 (2004) 1694–1728.
[63] J. Bonet, R.D. Wood, Nonlinear Continuum Mechanics for Finite Element Analysis, 2nd edition, Cambridge University Press, 2008.
[64] H. Luo, J. Baum, R. Lohner, An Improved Finite Volume Scheme for Compressible Flows on Unstructured Grids, AIAA Paper 95-0348, Reston, Virginia, 2012.
[65] J. Haider, C.H. Lee, A.J. Gil, A. Huerta, J. Bonet, An upwind cell centred Total Lagrangian finite volume algorithm for nearly incompressible explicit fast solid dynamic applications, Comput. Methods Appl. Mech. Eng. 340 (2018) 684–727.
[66] B. Engquist, S. Osher, One-sided difference approximations for nonlinear conservation laws, Math. Comput. 36 (1981) 321–351.
[67] R. Courant, K. Friedrichs, H. Lewy, On the partial difference equations of mathematical physics, Math. Ann. 100 (1928) 32–74.
[68] A.J. Chorin, A numerical method for solving incompressible viscous flow problems, J. Comput. Phys. 2 (1967) 12–26.
[69] S.K. Sambasivan, M.J. Shashkov, D.E. Burton, A finite volume cell-centered Lagrangian hydrodynamics approach for solids in general unstructured grids, Int. J. Numer. Methods Fluids 72 (2013) 770–810.
[70] J.C. Simo, N. Tarnow, The discrete energy-momentum method. Conserving algorithms for nonlinear elastodynamics, Z. Angew. Math. Phys. 43 (1992) 757–792.
[71] M.L. Wilkins, M.W. Guinan, Impact of cylinders on a rigid boundary, J. Appl. Phys. 44 (1973) 1200–1206.
[72] E. Boatti, G. Scalet, F. Auricchio, A three-dimensional finite-strain phenomenological model for shape-memory polymers: formulation, numerical simulations, and comparison with experimental data, Int. J. Plast. 83 (2015) 153–177.